2020

Developing highly efficient oxygen evolution reaction electrocatalysts by electronic structure regulation on transition metal oxides

Xiaoning Li
University of Wollongong

Developing highly efficient oxygen evolution reaction electrocatalysts by electronic structure regulation on transition metal oxides

A thesis submitted for fulfilment of the requirements for the

award of the degree

DOCTOR of PHILOSOPHY

From the

UNIVERSITY OF WOLLONGONG

By

Xiaoning Li, B.Sc., M.Sc.

Institute for Superconducting and Electronic Materials

Faculty of Engineering and Information Sciences

University of Wollongong, NSW Australia

13th August 2020

Certification of Originality

I, Xiaoning Li, declare that this thesis submitted in fulfilment of the requirements for the conferral of the degree Doctor of Philosophy, in the Institute for Superconducting & Electronic Materials, Faculty of Engineering and Information Sciences, University of Wollongong, is wholly my own work unless otherwise referenced or acknowledged. This document has not been submitted for qualifications at any other academic institution.

Xiaoning Li

13th August 2020

Acknowledgments

Time flies by so fast, fast as fleeting, and as my PhD career draws to a close. I would also like to thank UOW for my International Postgraduate Tuition Award (IPTA) and the China Scholarship Council (CSC) for providing me with living expenses.

I would like to express my heartfelt appreciation to my supervisors, Prof Zhenxiang Cheng, who provided me with the opportunity to carry out Ph.D studies at the University of Wollongong and kind supervision throughout my Ph.D studies. I appreciate the platforms and inspiration he has provided to achieve innovation in scientific research, I also thank him for the supports of life and study during difficulties, especially during the worldwide spread of COVID-19. I also want to show my thanks to my co-supervisor, Prof. Xiaolin Wang, who gives me sincere encouragement, understanding, and valuable advices on my project during my PhD study.

Technical assistances from people at UOW, such as Dr. Tania Silver (Language Polishing), Dr. Germanas Peleckis (XRD, PPMS), Dr. Dongqi Shi (Furnace Training), Dr. Tony Romeo (FESEM), Dr. Qiang Zhu (FESEM), Dr. Gilberto Casillas-Garcia (TEM), Dr. David Mitchell (TEM), Dr. David Wexler (TEM), and Patricia Hayes (UV-Vis) are also highly appreciated. In addition, I want to thank the staff in UOW, such as Ms. Crystal Mahfouz (Administrative Assistant), Ms. Narelle Badger (Administrative Assistant in AIIM), Ms. Naomi Davies (Administrative Assistant in AIIM), Ms. Joanne George (Laboratory and Safety Operations Officer), and Ms. Candace Gabelish (Laboratory and Safety Operations Officer), who gave me great assistance and especially safety education assistance. I would like to express my thanks to the Dr. Bruce Cowie at the SXR beamline at the Australian Synchrotron, part of ANSTO for his great help in the X-ray Absorption measurement and data analysis.

I would also like to thank my colleagues and friends at UOW, since they gave me a lot of help in many different ways. Many thanks to Ms. Yanhua Sun, Mr. Yun Lu, Ms. Daolan Liu, Mr. Letao Yang, Mr. Xiaobo Zheng, for their readiness to share knowledge and valuable suggestions.

I am very grateful for the supports, encourages, loves from my teachers, family, and friends in China, for encouraging me to overcome the difficulties, frustrations and anxieties encountered on my path.

Finally, a poem to end:

Importance always means

one thing in relation to another.

There is no such thing as

importance alone.

What if 'nothing' never existed?

Maybe there is,

and always was,

an everything forever.

Abstract

The efficiency of rechargeable metal-air battery, water electrolysis systems, solar fuels devices is limited by the oxygen evolution reaction (OER) due to its sluggish kinetics. For the OER process, it not only involves four sequential proton coupled electron transfers, but also includes a spin state transition from the spin singlet state of OH^-/H_2O to the spin triplet state of O_2 production. Considering this kind of spin state transition is quantum forbidden, it needs to associate an active catalyst with specific spin configurations to lower the energy consumed to promote such spin transition as well as the charge transfer. While the spin configuration of transition metal based OER electrocatalysts, is strongly coupled with other fundamental parameters, such as charge, orbital, and lattice, and they determine the outward manifested properties all together. Therefore, to understand the true mechanism of OER is to identify the roles of spin and clarify its correlations with other intrinsic parameters.

In this doctoral research, we attempt to start with various physical properties which correlated with OER efficiency to elucidate the complex situations (**Chapter 4**), including:(1) oxidation states of transition metal ions, (2) crystal field splitting, (3) eg electron number, (4) bond length, (5) electronic conductivity, (6) magnetic property and (7) oxygen p band centre. Based on the comprehensive understanding from the aspect of spin, conclusions can be drawn that transition metal compounds with higher oxidation, appropriate crystal field and local coordination, around unit e_g electron, shorter bond length, and ferromagnetic exchange interaction will be highly desirable for enhancing the overall OER efficiency.

Following above analysis (**Chapter 5**), we first demonstrated an excellent platform to investigate the roles of the composition and structure in tuning the electron configuration for higher OER efficiency is provided by layered perovskite oxides with subtle variations of composition and structure (doping with 0%, 50%, and 100% cobalt in the $Bi_7Fe_3Ti_3O_{21}$). The crystal structures were analyzed by X-ray diffraction refinement, and the electronic structures were calculated based on X-ray absorption spectroscopy and magnetization vs temperature plots according to the Curie−Weiss law. The results indicate that the elongation of oxygen octahedra along the c-axis in layered perovskite could stabilize Co ions in the intermediate spin (IS) $(t_{2g})^5(e_g)^1$ state, resulting in dramatically enhanced electronic conductivity and absorption capacity. Subsequently, the OER efficiency of sample with 100% Co was found to be (incredibly) 100 times higher than that of the sample with 0% Co, with the current density increased from 0.13 to 43 mA/cm^2 (1.8 V vs reversible hydrogen electrode); the Tafel slope was reduced from 656 to 87 mV/dec; and double layer capacity enhanced from 174 to 4193 $\mu F/cm^2$. This work reveals

that both the composition and structure should be taken into account to stabilize a suitable electronic structure such as IS Co ions with moderate absorption and benign electronic conductivity for high-efficiency catalysis of the OER.

Furthermore, instead of only adjusting the electronic structure, we utilize ferroelectric polarization to accelerate the oxygen evolution reaction as well (**Chapter 6**). This is demonstrated by in situ growth of a secondary phase $BiCoO_3$ on a multiferroic layered perovskite $Bi_5CoTi_3O_{15}$ matrix to tune the e_g electron number and utilizing the ferroelectric polarization by corona poling afterward. The material system is designed from the deliberate insertion of several layers of $BiCoO_3$ into the three-layered perovskite $Bi_4Ti_3O_{12}$. From considerations of structural tolerance and thermodynamic stability, only one layer of BCO can be inserted to form a four-layered perovskite oxide $Bi_5CoTi_3O_{15}$, while the residual BCO would be deposited in situ on its surface as the secondary phase. It turned out to be very effective, the as-prepared multiferroic electrocatalysts are more efficient than the benchmark IrO_2 (with a final 320 mV overpotential at the current density of 10 mA cm^{-2} and a 34mV dec^{-1} Tafel slope) thanks to the superimposed effects of electronic regulation and ferroelectric polarization. The electronic structure and the contribution of the ferroelectric polarization are studied in detail by various tests and measurements, and a possible enhanced mechanism is proposed. This work not only demonstrates a low-cost and high-efficient OER electrocatalyst, but also provides a strategic design for multicomponent electrocatalytic material systems by consideration of both spin and polarization degrees of freedom.

Subsequently, we devote our efforts to exploring a new flexible structure that is competent in providing large amounts of oxygen vacancies as well as offering the freedom to manipulate the electronic structure of metal cations (**Chapter 7**). This is demonstrated by anchoring low valence state Co at high valence state Nb sites in the tetragonal tungsten bronze (TTB) structured $Sr_{0.5}Ba_{0.5}Nb_{2-x}Co_xO_{6-\delta}$, with different ratios of Co to Nb to optimize the Co substitution proportion. It is found that the occupation of Co in the Nb^{5+} sites gives rise to the generation of massive surface oxygen vacancies (O_{vac}), while Co itself is stabilized in Co^{2+} by adjacent O_{vac}. The coexistence of O_{vac} and LS Co^{2+} enables an oxygen intercalation mechanism in the optimal SBNC45 with specific activity at 1.7 V vs. reversible hydrogen electrode that is 20 times higher than for the commercial IrO_2. This work illuminates an entirely new avenue to rationally design OER electrocatalysts with ultrafast kinetics.

Table of Contents

List of Figures

List of Tables

Chapter 1

1 Introduction

Sustainable development of human society should be expected with a switch from traditional fossil fuels to a new era of clean energy economy lifestyle. Water splitting by electricity or by photovoltaics device can generate hydrogen fuels with high energy density and zero pollution, being regarded as one of the most promising techniques to alleviate energy and environmental issues [1]. However, water splitting requires highly performing catalysts for the two half reactions on the two electrodes, known as the hydrogen evolution reaction (HER) and the oxygen evolution reaction (OER). It is well acknowledged that the oxygen evolution reaction (OER) half of the overall water-splitting process is underdeveloped compared to the other half, the hydrogen evolution reaction (HER). OER involves the formation of oxygen-oxygen bond and relates to the four proton-coupled electron transfer processes, leading to sluggish kinetic and consequently demand a high overpotential. Thus, OER mechanism investigations and high-efficient OER electrocatalysts designs are the two main tasks for researchers in this field.

1.1 Research progress of OER electrocatalysts

The current commercial OER electrocatalysts are Pt or RuO_2/IrO_2, while a great deal of efforts have been expended on possible alternatives due to their scarcity and high cost [2]. Earth-abundant transition metal compounds have drawn dramatically interesting since last century, due to the low cost, high intrinsic activity, and good stability in the alkaline electrolytes [3,4]. What's more fascinating in perovskites and spinel-type oxides is that its OER performance can be greatly improved based on the strong couplings between the fundamental quantum parameters and the large freedom of regulation on the crystallographic and electronic structures [5-8]. This has advantaged them as one of the most promising candidates among other material families for the application of future energy devices based on water splitting.

Perovskites ABO_3, for instance, $La_{1-x}Sr_xCoO_{3-\delta}$ (x=0~1, LSCO), is well recognized as a family of high-efficient OER electrocatalysts, with the two famous end compounds, $LaCoO_3$ (LCO) and $SrCoO_3$ (SCO) [9,10]. Typically, LCO adopts adsorbate evolution mechanism (AEM) during the OER process, while SCO is capable of a faster lattice oxygen mechanism (LOM), associated with ordered oxygen vacancy or oxygen intercalation [11,12]. This sharply contrast in the mechanism adoption intimates that OER

performance is strongly depended on the crystal structure, the oxidation state of Co cations, and the oxygen stoichiometry. One of the straightforward strategies to adjust above factors in the LSCO is chemical doping to vary the *x* value. For example, J. Tyler Mefford et al reported the OER activity is enhanced with the increase of *x* in the LSCO, which is ascribed to the increase in the bulk oxidation state of Co as well as the increased concentration of oxygen vacancies [13]. In the research of Xi Cheng's group, Sr substitutions have the effect of straightening the octahedral cage, aligning atoms along the Co−O−Co axis, and increasing the average oxidation state of the Co cations, resulting in a considerably improved oxygen evolution reaction efficiency of the LSCO [14]. But it is hard to prepare perovskite oxides with low dimensional morphology with abundant active sites exposed.

In spinel AB_2O_4, the transition metals inside can occupy the tetrahedral and octahedral coordinations. Many famous OER members in spinel structure are iron-based and cobalt-based compounds with doped with such as Mn, Ni, Cu, Al and Zn [15]. Especially, Al^{3+} ions occupying the tetrahedral Co^{2+} Td sites optimizes the adsorption, activation, and desorption features of intermediate species during OER processes [16]. However, many researchers argue that transition metal cations in the tetrahedral sites are not major contributors in the OER actually [17], which is resources wasting. Meanwhile, layered double hydroxides (LDH) composed of positively-charged brucite-like host layers and charge-compensating interlayer anions, have been regarded as the true active materials in the OER test on the cobalt- and nickel based compounds[18]. But its OER efficiency was severely limited somehow by the intrinsic poor electron conductivity and the unavoidable agglomeration in nano dimension [19].

Apart from above oxides, many other transition metal oxides, sulfides, phosphides are also emerging, with compromise of OER activity between stability [15]. Despite of the tremendous materials reported with OER activity, the intrinsic physics is still not being well understood compared with other catalysis such as photocatalysis, which has stagnated its development despite of mature nanotechnologies.

1.2 Research progress of OER mechanisms

Since the early 20th century, the classical Sabatier principle demonstrates that the best catalysts should bind atoms and molecules with an optimum bond strength: not too weak in order to activate the reactants, and not too strong so as to desorb the products [20]. However, this principle lacks predictive power because it is not quantitative and cannot be validated experimentally. Currently, various OER activity descriptors based on transition metal oxides have been proposed to reflect the correlation of electronic structure with OER efficiency, for example, the number of *d*-electrons [21], the e_g band filling of the

transition-metal cations [22], the difference between the surface binding energies of O* and HO* reaction intermediates (ΔG_O* − ΔG_{HO}*) [23], the oxide formation energy [24], and the accumulation of the magnetic moment on the conduction plane atoms [25]. As pointed out by Cheng et al., however, it is better to consider the relationship of the OER activity to several physicochemical properties at the same time, due to the fact that there is some probability of incidental correlations between a single descriptor and the OER activity for a limited series of catalysts [26]. At the same time, the immediate reaction paths and oxygen species evolution during the OER process are drawing more and more interests from researchers.

For the traditional adsorbate evolution mechanism (AEM) [23,27], the rate-determining step is the O–O bond formation through nucleophilic attack of *O by water or OH^- occurring on single metal active sites (Eley–Rideal, ER-type mechanism) [28,3]. This step can be avoided by the direct formation of the O–O bond between the neighboring oxygen species on two adjacent active sites (Langmuir–Hinshelwood, LH-type mechanism) [29]. In principle, the LH-type mechanism with two conjunct active sites is more desirable, but it requires the distance between two active sites to be short enough [30]. Activating the LH-type mechanism remains a challenge if only metal cations are OER-active, as two metal cations are spatially separated by the oxygen anion in oxide catalysts, while the pure transition metals with short metal atom distances are usually unstable as anode. Recently, O-O formation via direct coupling between a metal cation and a lattice oxygen anion, known as lattice oxygen mechanism (LOM), has been proposed both theoretically and experimentally [31-33]. In this mechanism, both metal cations and lattice oxygen anions are active sites, cooperating with each other due to the short distance between them. The underlying physics of the LOM is that the electrons involved are contributed by the metal 3*d* orbitals as well as the O 2*p* orbitals when Fermi level enters into the O 2*p* band [13].

Despite the great progress achieve in the descriptors and mechanisms, the overpotential of OER is more than ten times higher compared to the other half reaction, hydrogen evolution reaction (HER). For instance, some ultrathin two-dimensional HER electrocatalysts such as phosphates CoP can achieve a cathodic current density of 20 mA/cm^2 at an overpotential of 85 mV owing to the extremely substantial active sites of low dimensions and good conductivity [34]. In contrast, some OER electrocatalysts such as phosphates Fe-Co-P alloy require at least 250 mV high overpotential to achieve a anodic current density of 10 mA/cm^2 [35]. The underlying reason for this is that the OER half of the process is limited by the additional constraints of the spin transition on top of the charge transfer. The mechanism of the spin

transition in the OER, however, and its significance is not yet fully understood and recognized, and there have been relatively few studies on this point so far.

1.3 Research and thesis structure

Based on above, this thesis work aims to develop new and effective strategies to regulate the electronic structure, reveal more underlying OER mechanisms involved, and finally provide more highly efficient OER electrocatalyst with the potential to be further developed into practical applications in the future.

The scope of this thesis work is briefly outlined as follows:

Chapter 1 presents the general background of OER and the thesis structure.

Chapter 2 presents a literature review on the OER mechanisms with the consideration of spin attribute of an electron.

Chapter 3 presents the main preparation methods, as well as the materials and electrochemical characterization techniques.

Chapter 4 presents a single-phase platform to investigate the roles of the composition and structure in tuning the electron configuration for higher OER efficiency: by three layered perovskite oxides with subtle variations of composition and structure (doping with 0%, 50%, and 100% cobalt in the $Bi_7Fe_3Ti_3O_{21}$).

Chapter 5 presents a heterojunction platform to tune e_g electron number and corona poling ferroelectric polarization afterwards to improve the OER activity: by in-situ grown a secondary phase $BiCoO_3$ on a ferroelectric matrix $Bi_5CoTi_3O_{15}$.

Chapter 6 presents a flexible platform to introduce large amounts of oxygen vacancies as well as offering the freedom manipulate the electronic structure of metal cations: by anchoring low valence state Co at high valence state Nb sites in the tetragonal tungsten bronze (TTB) structured $Sr_{0.5}Ba_{0.5}Nb_{2-x}Co_xO_{6-\delta}$, with different ratios of Co to Nb to optimize the Co substitution proportion.

Chapter 7 summarizes the conclusions that were obtained from this doctoral work and provides some suggestions for future research work related to both piezo/triboelectric energy harvesting and piezo-catalytic reactions.

Chapter 2

2 Literature review

2.1 Introduction to the OER with the consideration of spin

The oxygen evolution reaction (OER) has been the rate-determining step that hinders water splitting applications in various energy conversion and storage devices. It is mainly due to the fact that this process not only involves four sequential proton coupled electron transfers, but also includes a spin state transition from the spin singlet state of OH^-/H_2O to the spin triplet state of O_2. Ideal OER electrocatalyst should preserve the capability to extract electrons with same spin from adsorbates as well as smooth spin polarized electron transportation afterwards. In order to lower the energy consumed in spintrocatalytic OER process, it is necessary to associate an active- catalysts with specific spin configurations to promote the spin state transition. While the spin configuration of transition metal based OER electrocatalysts, is strongly coupled with other fundamental parameters, such as charge, orbital, and lattice, and they determine the outward manifested properties all together. Therefore, to understand the true mechanism of OER is to identify the roles of spin and clarify its correlations with other intrinsic parameters.

The ground spin state of singlet OH^-/H_2O (nonmagnetic) and triplet O_2 (magnetic) are demonstrated in **Figure 2.1**. By comparing the difference of reactant and resultant, it easy to understand that the formation of the oxygen molecular with O−O π^* bond demands extraction of two electrons with the same spin direction from the surface chemisorbed OH^- species by the electrocatalyst surface active sites. In theory, the rate of a chemical reaction will be extremely slow if the spin of the electronic wave function of the products differs from that of the reactants, as the Hamiltonian does not contain spin operators.[36] Forbidden by quantum mechanics, oxygen evolution reaction is necessarily to be associated with an additional stimulus energy to proceed, such as magnetic field, thermal disturbance or electric potential [37]. For instance, oxygen molecular produced in photosynthesis is found to be determined by spin and orbital physics of the four- manganese catalyst [38]. In terms of photocatalytic water splitting, Steeve Chrétien et al used spin-polarized density functional theory calculation on TiO_2 (110) to reveal the importance of spin conservation[39]. While for the electrocatalytic oxygen evolution, E. Torun testified that O_2 molecule produced on the RuO_2 (110) surface is 1 eV lower in energy when the surface is magnetic [40]. Given that TiO_2 is one of the most acknowledged solar-driven water splitting

photocatalysts, while RuO_2 is one of the state-of-art electro-driven water splitting electrocatalysts, we can say that spin seems ubiquitous in the production of molecular oxygen [41].

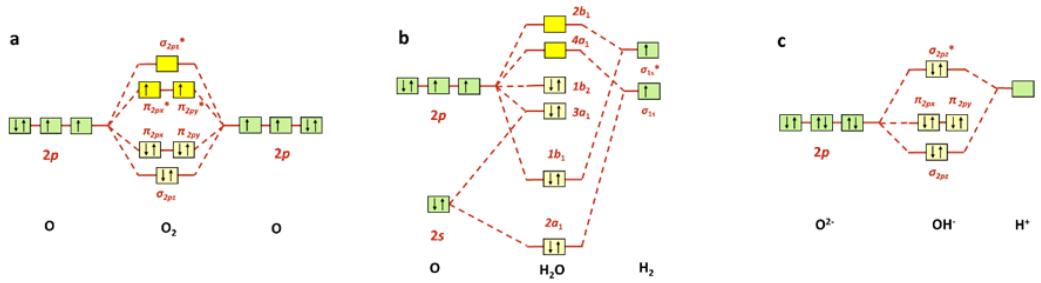

Figure 2.1 Ground state of oxygen, water and hydroxyl molecular orbital energy diagram.

2.2 Understanding the OER process with the consideration of spin

With respect to one O_2 evolution process, four electrons are transferred from adsorbates to the active sites by means of several steps (this part can be regarded as "surface reactions"). While these extracted electrons should be transported from the surface through the bulk electrocatalyst to the anode finally (this part can be regarded as "bulk transportation"). Both parts are all about electron behaviors and interaction between adsorbates, electrocatalyst and resultants. The transformation from OH^- to O_2 (in alkaline) or H_2O to O_2 (in acid) has similar intermediate oxygen species and evolution process for various widely accepted reaction mechanisms [42]. OER can be treated as a process of depletion of valence electrons of oxygen in the reactant OH^-/ H_2O (0) with 8 valence electrons per oxygen atom that satisfies the octet rule, to release product O_2 (5) with 6 valence electrons, among which two occupied π^* are unpaired with the same spin direction. From OH^-/ H_2O (0) to O_2 (5), the intermediates *OH (1), *O (2), *OOH (3), *OO (4) are chemisorptively bonded with active sites in the electrolyte-electrocatalyst interface, which are intrinsically electron deficient due to the charge transfer to the active sites [43]. Figure 2 provides three basic reaction paths of OER process concluded among various electrocatalysts, based on which the role of spin will be elucidated thoroughly afterwards.

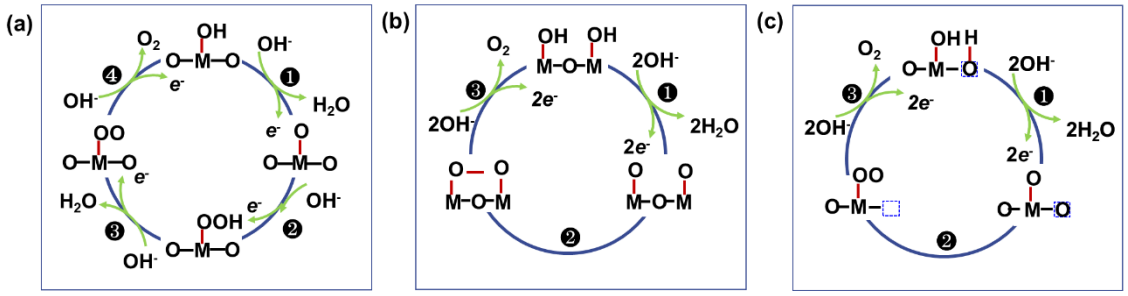

Figure 2.2 Well-recognized reaction paths proposed based on various electrocatalyst working in alkaline

OER electrolytes. (a) Eley–Rideal (ER) type adsorbate evolution mechanism (AEM) with single metal cation active site, from reactant OH^-(0) to intermediates *OH (1), *O (2), *OOH (3), *OO (4), to product O_2 (5). The number after each oxygen species is marked for a better logics in main text, but not marked in figures to avoid intricacy; (b) Langmuir–Hinshelwood (LH) type adsorbate evolution mechanism (AEM) with two adjacent metal cation active sites; (c) lattice oxygen mechanism (LOM) with one metal cation active site and one oxygen in lattice involved. LH-tpye AEM and LOM is with reactant OH^-(0) to intermediates *OH (1), *O (2), *OO* (4), to product O_2 (5), with the bypassing of *OOH (3).

As previous reported, different reaction routes will be favoured by different electrocatalysts (or by different local crystal plane surfaces in the same electrocatalyst) in order to minimize free energy of activation. For instance, there are two different reaction paths based on adsorbate evolution mechanism (AEM): (1) the Eley–Rideal (ER) type and (2) the Langmuir–Hinshelwood (LH) type [25]. (**Figure 2.2a, 2.2b**). In AEM, adsorption of reactants or intermediates on the surface of electrocatalysts is actually the results of orbital overlap, generation of chemisorptive bond, and charge transfer in the interface. From traditional view, Sabatier principle suggests that the adsorptive interactions between the catalyst and the adsorbates are expected to be "just right" [26]. Adjusting adsorption capacity of active sites has been regarded as one of the most powerful strategies to reduce the surface reaction energy barrier. For 3*d* transition metal based oxides with octahedron coordination, the adsorption capacity correlates to the e_g occupation, due to spatial overlap and energetic similarity of the electronic states [25,27]. Yang Shao-Horn's research group revealed that the OER activity exhibited a volcano-shaped dependence on the number of e_g electrons of transition metal perovskite oxides [28,29]. Despite the complexity of the local surface, such as reconstructions, space charges, polarity or segregation [30], we assume that there must be some universal roles spin played during OER process, as the efficiency descriptor e_g electrons number is decided by the spin configuration of an electrocatalyst.

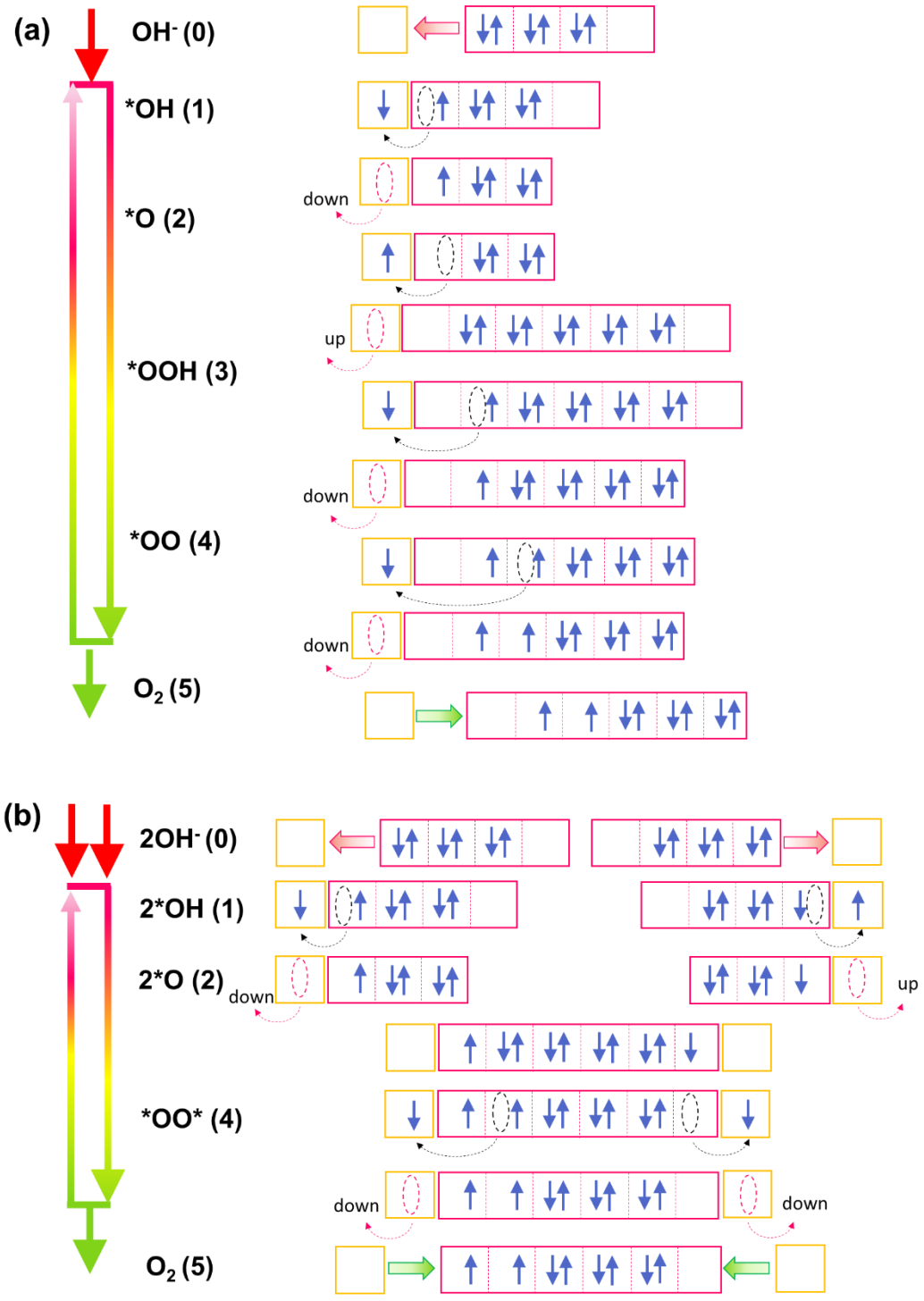

Figure 2.3 Possible cases of the outer electron's behaviours during OER process. (a) is the cases for one active site mechanism such as ER-type AEM; (b) is the cases for two active sites mechanism such as LH-type AEM and LOM. The red squares present the hybrid orbitals of oxygen species, which is simplified without the energy level contrasting to Figure 1. The black dashed circles and lines with arrows track the electron transfer/hopping between adsorbates and active sites via chemisorptive bonding. The electron depletion occurs as the red dashed circles and lines denoted, which are delivered away surface to bulk.

Here, the spin direction of the four electrons are down-up-down-down, other possible cases can also be possible if three in four electrons are in the same spin direction.

Figure 2.3a shows one possible situation of the outer electron's behaviours from the spin view during the ER-type AEM process. The six electrons of OH^- (0) in electrolyte are all paired occupied the three low energy orbitals, from which let us assume that the active site will select a spin down electron for the formation of *OH (1). In this stage, the electron actually is still shared by the adsorbate and surface-active site due to their shared chemisorptive bond. It should be extracted from surface afterwards via bulk transport to the external circuit to make the active site available for the transformation of *OH (1)-*O (2). If the electron extracted during the formation of *OH (1)-*O (2) is spin down; spin up for the next one during the formation of *O (2)-*OOH (3), then the subsequent one during the formation of *OOH (3)-*OO (4) should be spin down for the evolution of O_2 (5). If the electron extracted during the formation of *OH (1)-*O (2) and *O (2)-*OOH (3) are spin down, then the subsequent two electrons should be with different spin directions. Hence, we find that the rationale is that three in four electrons extracted from reactant and intermediates are in the same spin direction. It should be noted that other cases can be possible, since spin selection during each electron transfer is dictated by the contemporary available orbital of the active sites. If the active sites are not capable of extracting three spin up and one spin down electrons, some electrons have to suffer a spin flip during transferring to satisfy the rationale before oxygen evolution.

Now, we inspect the situation of other reaction routes these two active sites: LH-type AEM and LOM. In these cases, the transformation of *O (2)-*OOH (3) and *OOH (3)-*OO (4) are replaced by *O (2) -*OO* (4), the energy barrier is relatively lower as it detours the rate-limiting step of OOH* (3) with the collaboration of two adjacent cation active sites **(Figure 2.2b, and 2.2c**). For instance, the OER activity of quadruple perovskite $CaCu_3Fe_4O_{12}$ (CCFO) exceeds that of the benchmark $Ba_{0.5}Sr_{0.5}Co_{0.8}Fe_{0.2}O_{3-\delta}$ (BSCF) and RuO_2 by adopting the LH-type mechanism [31]. As explained, it is benefited from the catering geometric structure of the shorten oxygen–oxygen distance (~2.6 Å) induced by heavily bent Fe–O–Fe bonds. Lately, O-O formation via direct coupling between metal cation and lattice anion known as lattice oxygen mechanism (LOM) is observed in today's most active transition metal oxide OER electrocatalysts [7-9,32]. The underlying physics of LOM is that the Fermi level is lowered into oxygen 2*p* band induced by the strong overlap of metal 3*d* with oxygen 2*p* [33]. Generally, the kinetic of LOM is

even faster than ER-type AEM due to the non-concerted proton–electron transfer process, as reported in LOM-adopted $CaCoO_3$ with substantially smaller lattice parameter and shorter surface oxygen separation [34]. In LOM, the redox centre of the catalyst is no longer limited to the metal alone, and the ligand holes are also involved in the oxidation reaction. It's noteworthy that the prerequisite for rapid LOM reaction is that O *p*-band centre is close enough to the Fermi level, which is also the culprit for poor stability of electrocatalysts [35]. One of the differences between LH-type AEM and LOM is that lattice oxygen is activated as active sites in LOM. Similarly, the spin rationales based on these two active sites involved mechanisms (LH-type AEM and LOM) are in line with that concluded from one active site mechanism (ER-type AEM), as depicted in **Figure 2.3b**.

The selective removal of spin-polarized electrons from the active sites, allows the appropriate magnetic moment for oxygen molecules to evolve. To realize this kind of selective electron removal on the surface, electrons transferred to bulk should be with certain spin polarization to prompt the kinetics. Hence, the bulk transportation in OER is not only simply about charge transfer but also associating with the spin transport. Therefore, materials coupled mixed-valence spin acceptors guarantee spin passages in principle with minimum Gibbs energy of activation are strongly desired [44]. Some measurable physicochemical properties can be representative to access the efficiency in the bulk transportation part, such as conductive and magnetic property, and their correlations with OER efficiency have been extensively studied [45,46]. With a clear understanding of OER mechanism, following sections will discuss the specific roles of spin played in the OER process from several correlated physical, chemical and crystal and electronic structural aspects.

2.3 Influence of oxidation states on the OER

The fulfillment of electron-counting rules for maximum stability of oxidized transition metal ions is the main driving force for the OER activity. The harder to lose electrons when forming compounds with anions, the stronger driving force in the OER electrocatalytic reaction, and this ability is decided by the oxidation (electrophilicity) of transition metal ions. As a matter of fact, Sabatier principle mentioned above can be understood in terms of the simplest descriptors in chemistry: the number of outer orbit electrons and the oxidation states [47]. Throughout the periodic Table, alkaline earth metals are always in the valence of 2+, and Ln group are usually in the valence of 3+. While for transition metal oxides with unfulfilled 3*d* orbital, their oxidation tends to vary a lot. According to the electrically neutral principle, the oxidation of transition metal ions can be adjusted by means of manipulating the element composition.

The element selection in A-site ions can impose constraints on B-site transition metal cation valence as well as oxygen non-stoichiometry. For example, in ABO_3 perovskite, valence states of B-site transition metal cations is decided by the A-site cations, which can accommodate alkaline, alkaline earth, and rare earth metal ions with valence states ranging from 1+ to 3+ (The valance state of Co cations may be 2+, 3+ to 4+ depending on the amount of Sr (2+) in the perovskite $LaSr_{1-x}Co_xO_3$). The oxidation state of the transition metal ions can be easily determined by X-ray photoelectron spectroscopic analysis (XPS) [48], X-ray absorption spectroscopy (XAS) [49], electron energy loss spectroscopy (EELS) [50], and Mössbauer Spectroscopy [51], and iodometric titration [52].

Oxidation state influence the OER efficiency by determining the spin state, e_g electron number, bond length and exchange interaction. At first, higher oxidation means less electrons in the *d* orbitals for a certain element. Meanwhile the number of electrons in *d* orbitals together with its crystal field directly decides the spin state and e_g electron number, both of which are very important factors for OER (will be discussed in the following parts). Here an example of cobalt element with different oxidation is provided in **Table 2.1**. For a cobalt ion with 2+ oxidation in an octahedral coordination, it has seven electrons in 3*d* orbitals with two possible electronic configurations. That is high spin (HS, $(t_{2g})^5(e_g)^2$) with two e_g electrons in the weak crystal field and low spin (LS) $(t_{2g})^6(e_g)^1$ with one e_g electron in the strong crystal field. But for cobalt with 3+ oxidation, there are six electrons in 3*d* orbitals with three possible spin configurations: high spin (HS, $(t_{2g})^4(e_g)^2$, two e_g electrons), low spin (LS, $(t_{2g})^6(e_g)^0$, zero e_g electron) and intermediate spin (IS, $(t_{2g})^5(e_g)^1$, one e_g electron). There is only on spin configuration of 4+ cobalt.

Table 2.1 Property variation of cobalt element with different oxidation.

Property	$Co^{2+}(3d^7)$		$Co^{3+}(3d^6)$		$Co^{4+}(3d^5)$
Spin state	HS	LS	HS	LS	HS
Configuration	$(t_{2g})^5(e_g)^2$	$(t_{2g})^6(e_g)^1$	$(t_{2g})^4(e_g)^2$	$(t_{2g})^6(e_g)^0$	$(t_{2g})^3(e_g)^2$
e_g number	2	1	2	1	2
Radius	88.5 pm	79 pm	75 pm	68.5 pm	67 pm
Electronegativity	2.234	2.613	3.36	3.88	4.703

From the **Table 2.1** we can see that an ion at high oxidation state, or same oxidation with low spin state would result in a smaller ion radius, which may further shorten the bonding length between the adjacent ions. While the significance of bonding length in choosing surface reaction route has been mentioned above. Moreover, oxidation of cations also affects the exchange interaction and conductivity in bulk which relies on the spin state and bonding length of materials. For instance, the exchange of Mn^{3+}-O-Mn^{4+} is double exchange interaction with half metallic in $La_{1/3}Ca_{2/3}MnO_3$, while Mn^{2+}-O-Mn^{2+} is super-exchange interaction with insulator in MnO (More details will be discussed in the following parts) [53]. Generally, higher oxidation state is relatively more beneficial to accelerate the OER process, because its electrophilicity is strengthened and the adsorption and reaction of –OH to form adsorbed –OOH are boosted, as reported by many researchers [54]. Another phenomenon can't be ignored is that the formation energy of oxygen vacancy has been found to be correlated well with the number of electrons of the transition metals [47], so higher oxidation may bring about certain amount of oxygen vacancies in the electrocatalysts. While the advantages of oxygen vacancy on the electrocatalytic OER activity have been intensively investigated in $LiCo_{0.8}Fe_{0.2}O_2$, $SrNb_{0.1}Co_{0.7}Fe_{0.2}O_{3-\delta}$ and $La_{0.6}Ca_{0.4}CoO_3$, for example [55]. Furthermore, *d* band of the late transition metal ions with high oxidation have larger possibility to hybrid with p band of oxygen. In this situation, electrons of Fermi level are also contributed by oxygen anions and the redox centers are no longer limited to the 3*d* transition metal cation active sites alone [56].

2.3 Influence of crystal field splitting on the OER

Metal cations are coordinated by negatively charged anions in the oxides, sulphides or phosphides. The electrons of the cations are repelled by the neighboring anions ligands due to the repulsion of same negative charges. In this regard, the orbital energies of cations are raised and a crystal field potential is generated. Then the free rotation of the electrons is hindered and the orbital angular momentum is quenched, resulting in the crystal field splitting of the *d* orbitals of cations (degeneracy). Here is an example in the octahedral symmetry (**Figure 2.4a**), where six oxygen anions form an octahedron around a metal cation and the *d* orbitals of cation split into two sets with an energy difference (Δ_{oct}). Since the d_{xy}, d_{xz} and d_{yz} orbitals (named t_{2g}) are farther from the oxygen anions with less repulsion, it is in lower energy ($-2/5\Delta_{oct}$) compared to the directly head-to-head dz^2 and dx^2-y^2 orbitals (named e_g, $3/5\Delta_{oct}$). While in a tetrahedral crystal field (**Figure 2.4b**), four oxygen ions form a tetrahedron around the metal cation but they do not orient directly towards any *d* orbitals, so the energy splitting (Δ_{tet}) is lower than Δ_{oct}. Under this circumstances, lower energy orbitals will be dz^2 and dx^2-y^2 (e_g orbitals), and the higher energy orbitals

will be the d_{xy}, d_{xz} and d_{yz} (t_{2g} orbitals). Certainly, there is also other possible coordinations resulting with more than two sets of orbitals, and **Figure 2.4c-f** provides list some common cases.

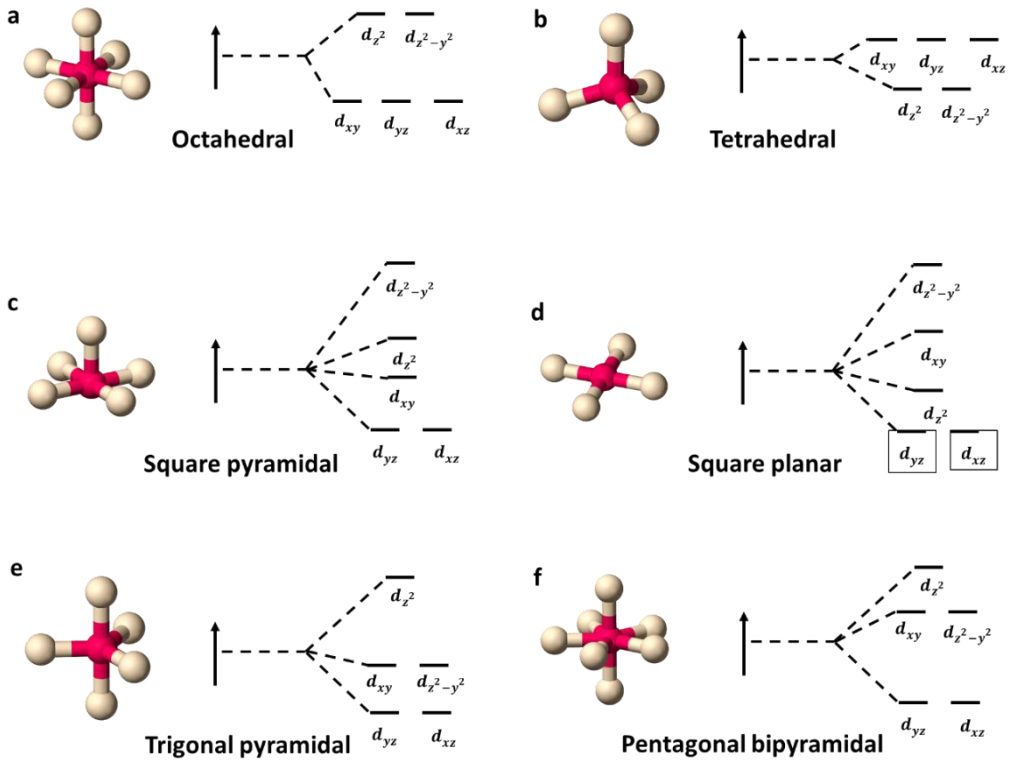

Figure 2.4 3*d* orbit crystal field splitting of several coordination. (a) Octahedral, (b) Tetrahedral; (c) Square pyramidal; (d) Square planar; (e) Trigonal pyramidal; (f) Pentagonal bipyramidal.

Crystal field splitting plays very important role in determining the spin configuration of *d*-band transition metals. Electrons tends to be in the configurations with the maximum unpaired number to reduce the pairing interaction energy (P), but additional energy are required to occupy the high energy orbital due to the crystal field splitting energy (Δ). Therefore, for a certain cation with a certain number of electrons, the spin configuration is decided by the competition between crystal field splitting energy (Δ) and electron pair interaction energy (P). In 3*d* transition metal oxides, crystal field splitting energy and electron pairs interaction energy are sometimes of comparable magnitude, which lead to very competing spin states. Generally, 4*d* or 5*d* transition metal oxides have low spin (LS) configurations with weaker electron pairs interaction energy compared with the 3*d* metals [57].

In general, crystal field splitting of the *d* orbit is affected by the following factors: (1) the nature of the metal ion; (2) the metal ion's oxidation state; (3) the arrangement of the ligands around the metal ion; (4) the nature of the ligands. In the first place, the higher oxidation state for a given metal, the larger

magnitude of crystal field splitting energy (Δ). Inversely, the transition metals with the high oxidation states are more stable in the large crystal field, such as face-shared polyhedral coordination stabilized Co^{4+} [58]. Secondly, small bond length between the ligand and the metal ion associates with large crystal field (Δ), which means that crystal field splitting can be manipulated by changing the lattice constant, bonding length, distortion or other structure parameters. Thirdly, spin state of the cations also impose effect on the crystal field splitting. For example, uneven occupations of the *d* sub-orbits may change the bonding length via Jahn–Teller distortions, and thus influence the crystal field itself conversely. Different ligands such as oxides, sulfides, selenide, phosphides also have strong impacts on the OER efficiency with totally different electronic/spin structure, [59]. The influence of transition metal coordination on the OER activity and stability of perovskites has been reported by many researchers [58].

2.4 Influence of e_g electron occupation on the OER

According to the crystal field splitting theory, 5-fold *d* orbitals will be degenerated into orbitals with different energy level according to the coordination environment symmetries. Only the electrons occupied at the high energy orbitals in the octahedral environment is called e_g electrons. In other coordination conditions, such as tetrahedron, bipyramidal, square planar, square pyramidal, the situations are different. Generally, the high-energy (HE) orbital parentage of cations is considered to more easily react with oxygen-related adsorbates due to their matched energies compared to other orbitals [60]. Here we select e_g electrons in the octahedron environment as a representative to discuss the effects of the high-energy (HE) orbital. In the octahedron, e_g orbitals will have strong spatial overlap with those of adjacent O 2*p* orbitals, forming σ-bonding and σ*-antibonding states with partial metal and oxygen character. While t_{2g} have weaker spatial overlap with nearby O 2*p* orbitals and form π-bonds and π*-antibonds. Therefore, the electron number of e_g orbital decides the chemisorption capability of OH^- to form bonding with metal ions. According to the Sabatier principle, the chemisorption bonds between electrocatalyst and oxygen species should be "just right" for the optimum efficiency. The presence of a single/unit electron in the antibonding e_g orbital is expected to yield just the appropriate strength of interaction. Yang Shao-Horn's research group revealed that the OER activity of transition metal perovskite oxides exhibited a volcano-shaped dependence on the number of e_g electrons (optimal $e_g \approx 1.2$) [60]. Unit e_g electrons has been one of the most powerful strategies in material design to improve the OER performance of various perovskite oxides [61,62]. The perovskite $Ba_{0.5}Sr_{0.5}Co_{0.8}Fe_{0.2}O_{3-\delta}$ (BSCF) with the $(t_{2g})^5(e_g)^{1.2}$ electronic

configuration of Co cations designed by following Yang Shao-Horn's principle has become the state-of-art OER electrocatalyst instead of IrO_2 [63]. Notably, the optimal e_g occupancy proposed by Yang Shao-Horn's research group is not an integer, indicating that the spin states of the transition metal atoms are an average value shared by the entire system, i.e., delocalized in the crystalline field [64].

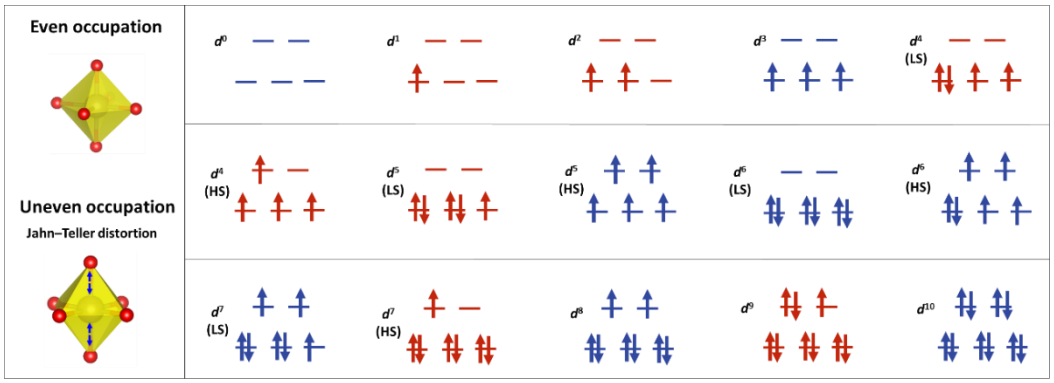

Figure 2.5 Possible spin states and e_g electrons of different electronic configuration in the octahedron coordination. The uneven occupation in red will introduce certain degree of Jahn-Teller distortion.

The number of e_g electron is basically determined by spin states, and **Figure 2.5** displays d^0-d^{10} cations in the octahedron coordination. However, the orbit occupation also influences on the local coordination geometry inversely. One common phenomenon is the Jahn–Teller distortion caused by uneven orbit occupation. Suppose one electron occupies the dz^2 orbital and no electron in the dx^2-y^2 (d^4, HS), then the metal–oxygen bonding will be elongated along *c* direction in the lattice due to the stronger Coulomb repulsive potential of *c* direction compared to *ab* plane [65]. Such an elongation weakens the metal-oxygen covalent bonds, which will inevitably bring about changes of the surface local coordination geometry as well as the electronic properties. For instance, Jahn–Teller distortion might facilitate the forming of oxygen defects on the surface or oxygen vacancies in the crystals while maintain the pristine structural framework, both of which affects the OER kinetics [66]. It is reported that oxides with one e_g electron and thus the Jahn–Teller distorted metal–oxygen octahedron show high activity for OER irrespective of the crystallographic structure of the catalyst [65]. Besides, another possible consequence brought about by Jahn–Teller distortion is the variation of metal-oxygen-metal bond length, which will also lead to different types of exchange interaction and the switch between RE-type and LH-type reaction mechanism.

2.5 Influence of the bond length on the OER

The importance role of bond length on the OER efficiency can be justified by: (1) the OER reaction route taken place on the surface; (2) electron transportation in the bulk. Just as illustrated in the OER mechanism above, LH-type reaction with fast kinetics occurs only when the oxygen-metal-oxygen distance is short enough. In the simple cubic perovskite $SrFeO_3$, the oxygen–oxygen distance is ~3.9 Å with the linear Fe–O–Fe bonds (~180°), which is too large to permit the oxygen atoms to interact with each other and form oxygen molecules via LH-type route. In a sharp contrast, the oxygen–oxygen distance is shortened to ~2.6 Å by heavily bent Fe–O–Fe bonds (~140°) in the quadruple perovskite $CaCu_3Fe_4O_{12}$, which has exceeded the state-of-the-art $Ba_{0.5}Sr_{0.5}Co_{0.8}Fe_{0.2}O_{3-\delta}$ and RuO_2 OER electrocatalysts [29]. The superior OER efficiency in α-Mn_2O_3 than Mn_3O_4 could also be ascribed to the dominated LH-type mechanism in the former one with a large variety of Mn−O bond lengths [67], and the uneven occupation of the e_g orbital and Jahn−Teller distortion [68].

The bond length also imposes its effects on the exchange interaction between adjacent ions as well as the electron conductivity, as the strength of the exchange interaction (exchange integral) is related to the wavefunction overlap, which decreases approximately exponentially when the proton–proton distance (bond length) increases. When the overall electronic and magnetic structure allows for the coupled charge-spin transport, increasing covalent metal-oxygen bonding increases the magnetization of the oxygen atoms through spin donation from certain high-spin transition metal ions, which is very desirable for lowering the spin transition potential from singlet OH^-/H_2O to triplet O_2 product. In the perovskite with small tolerance factor (*R*), metal-oxygen-metal bonds will be bended and deviated from 180° of the ideal perovskite structure, and the oxygen 2*p*−metal 3*d* transfer energy value will be decreased, which is confirmed to be favorable for the OER efficiency [69]. The monotonic increase in OER activity associated the average Mn−Mn distance from ~3 to ~3.2 Å was observed in the manganese oxides Mn_2O_3, Mn_3O_4 and $AMnO_3$ and AMn_7O_{12} perovskites (*A*=Ca, La, etc) [70]. The bond length (including the bonding angle) depend on the crystal lattice and electronic structures of the materials. There are many factors determine the bond length of the ions in a specific compound, including the pristine structural framework, oxidation of transition metal cations, e_g occupation/Jahn-Teller distortion and lattice defects.

2.6 Influence of conductivity and magnetic property on the OER

Atoms in covalent oxides interact with each other to exchange charge and spin through the orbital hybridization. This kind of coupling between intrinsic angular momentum of the electrons and orbital ordering is called quantum exchange interaction [71]. In transition metal oxides, the exchange interactions

between metal cations via oxygen anions can be explained by the Goodenough-Kanamori rules, known as super-exchange interaction, and double-exchange interaction [71]. As shown in **Figure 2.6a**, two metal cations with the same oxidation states are 180° antiferromagnetic coupled via an intermediary oxygen anion. In this case, the spin direction of the electrons of the two cations are antiparallel. If the two cations are connected at 90° via an intermediary oxygen anion, the exchange interaction becomes ferromagnetic, resulting in the same spin direction of the neighboring cations (**Figure 2.6b**). If the two metal cations are with different oxidation states, the spin direction of their electrons is coupled through double exchange interaction, as shown in **Figure 2.6c**. Oxygen anion gives up its spin-up electron to the higher oxidized cation, then its vacant orbital will be filled by a spin-up electron transferred from the adjacent lower oxidized cation. At the end of the exchange, an electron has been transferred between two neighboring metal cations with the preservation of its spin direction. Since the reverse of spin direction is avoided in the double exchange interaction process, the transportation speed is relatively fast. Take the $La_{0.5}Sr_{0.5}MnO_3$ compound as an example, double exchange are facilitated with the increase the oxygen deficiency and Mn 3+/Mn 4+ ratio, resulting in the enhanced conductivity and OER efficiency [72].

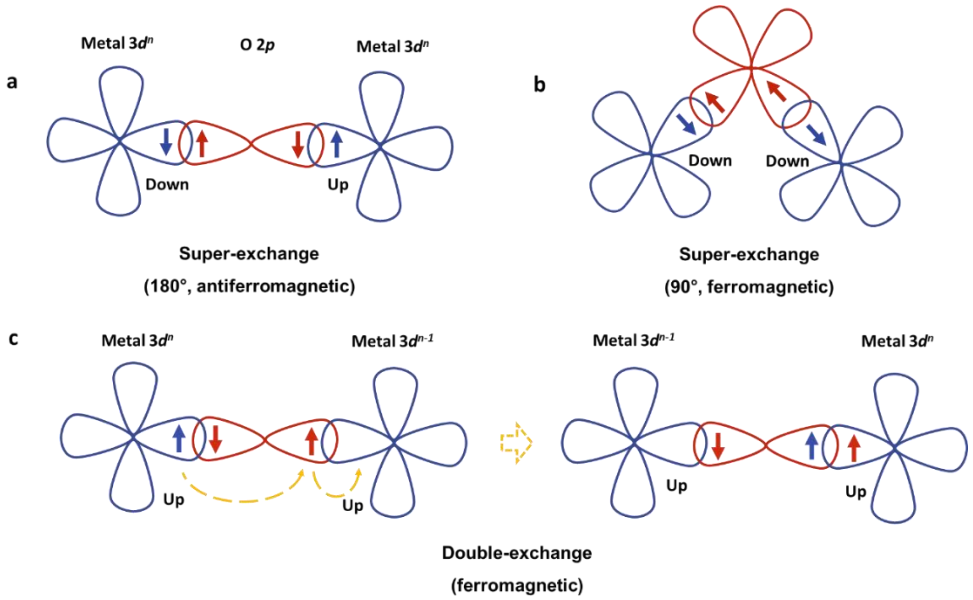

Figure 2.6 Possible inter-ions exchange interaction types in the transition metal oxides.

In the spin-consuming OER process, proper exchange interaction between metal cations in the electrocatalyst can accommodate a spin current together with fast charge transfer. It will reduce the Coulomb repulsions with more itinerant charge carriers during the bulk transportation [71], which can also dramatically decreases the activation energy of spin-selective steps on the surface reaction [57].

Specifically, exchange interaction affects the stability of the intermediate species and hence influences the kinetic barrier to bond formation and cleavage. For example reductive cleavage of the O-O π* bond (oxygen reduction reaction, ORR) is favored when the metal active sites are antiferromagnetic coupled, whereas oxidative formation of the O-O π* bond (OER) is favored by ferromagnetic coupling [24]. Iwakura *et al* experimentally proved that the OER overpotential is diminished with the increase in magnetization in the spinel ferrites [73]. Nevertheless, a ferromagnetic exchange interaction is not sufficient condition to guarantee a highest OER efficiency. First-class electrocatalysts should also have empty orbitals to preserve an incoming spin flow [74]. For instance, for the active sites with high spin state $3d^5$, $(t_{2g})^3(e_g)^2$, is not ideal for OER, since the incoming electrons from adsorbates need to be paired with pre-existing electrons in the orbit with release of energy which make it difficult for the following desorption and transport process [75].

Higher delocalization and more unpaired electron number is favorable to increase the conductivity in the bulk transition metal oxides without the consideration of spin. Dependency of conductivity on the increased unpaired electrons was observed in the $CoFe_{2-x}Cr_xO_4$ with the replacement of Fe (3+, d^5, $(t_{2g})^3(e_g)^2$) by Cr (3+, d^3, $(t_{2g})^3$). When increasing the x, $(t_{2g})^3$–$(t_{2g})^3$ interaction remains but interaction of e_g orbitals is interrupted, so the number of unpaired electrons increases resulting in the enhanced conductivity [76]. Meanwhile higher delocalization degree of electrons can enhance the conductivity of the electrocatalysts, decreasing the energy consumption of the electron transportation. For example, *d*-electron delocalization is induced by the structural distortion in the confined two-dimensional ultrathin nanosheets NiS and NiSe with the Ni^{2+} $(t_{2g})^6(e_g)^2$, resulting in enhanced electrical conductivity and OER efficiency [64]. However, caused by the strong on-site Coulomb repulsive interaction, most of the pristine perovskite oxides do not have synchronized appropriate e_g electron filling degree and electrical conductivity at the same time [64].

So as to the magnetic property of a material, it is rooted in the exchange interaction between adjacent ions, and comprehensively linked to its crystal morphology and microstructure. **Figure 2.7a** depicts the ferromagnetic (FM) characteristic in a lattice of *d* orbit unfulfilled transition metal oxides, in which spin can be accumulated in any direction, resulting various spin polarization planes. Spin in the A-type antiferromagnetic (A-AFM) in **Figure 2.7b** has a chance to be preserved in only one current plane, because of the intra-plane ferromagnetic and inter-plane antiferromagnetic characteristics. For G-type antiferromagnetic (A-AFM) in **Figure 2.7c**, there is no any spin accumulated plane. If the opposing

moments introduced by antiferromagnetic interaction are unequal and there will be a spontaneous magnetization remains. This is called ferrimagnetism, and happens in the materials composited by different cations. In theory, materials with FM type interaction are usually more conductive with higher rate of charge and spin transfer compared with AFM type oxides. With regard to the AFM interactions, A-AFM OER oxides are usually performed high activity due to the spin polarization favoring the step of oxygen releasing in **Figure 2.7c** and **2.7d** at intra-plane ferromagnetic surface layers [25]. Well-recognized high-efficient OER electrocatalyst such as $Ba_{0.5}Sr_{0.5}Co_{0.8}Fe_{0.2}O_{3-\delta}$ (BSCF) is with A-AFM ground state. By doping Nb^{5+} ions into strontium cobaltite to reinforce an individual A-AFM ordering allowing spin-covalent bonding to accumulate larger magnetic moments on the conduction planes, the OER efficiency of $SrNb_{0.1}Co_{0.7}Fe_{0.2}O_{3-\delta}$ and $SrSc_xNb_yCo_{1-x-y}O_{3-\delta}$ have surpassed the BSCF by several factors. G-AFM ordering in the octahedral coordination oxides are not-so-good OER electrocatalysts given the fact that the signs of magnetic moment in any direction of conduction is cancelled out completely, resulting in zero spin current even though they link transition-metal atoms with a large magnetic moment. Perovskites with high spin G-AFM exchange interactions such as $LaFeO_3$, $LaCoO_3$, $CaMnO_3$ and $LaMnO_3$ have limited conductivity ($<10^{-3}$–10^{-4} Ω^{-1} cm^{-1}) and low electrocatalytic activity (antiferromagnetic insulators), compared with the ferromagnetic (FM) $CaMnO_{3-\delta}$ and $Ca_{0.9}Yb_{0.1}MnO_{3-\delta}$ [41]. Ferrimagnetic materials with AFM exchange interaction and uncompensated magnetic moments such as spinel Mn_3O_4 [77], $NiCo_2O_4$ [78] are good catalyst for OER due to better conductivity than pure AFM material. Paramagnetic conductors ($>10^{-3}$ Ω^{-1} cm^{-1}), $EuNiO_3$, $PrNiO_3$, $LaNiO_3$ and for example are good electrocatalyst for OER are good catalysts [74].

To sum up, OER efficiency and magnetic property of a material is of a certain degree of relevance, since both of them are in connection with intrinsic exchange interaction of the atoms. If we want to assess the possible OER activity of a material from magnetism angle, ferromagnetic conductors may be the most desired type in terms of conserving the spin current. One of the most important character of this class of materials is that they usually are spin polarized meeting the requirements of good conductivity and unpaired *d* orbit electrons, which facilitate the efficient spin transport in step 3 and step 4 in ER-type (or step 3 in LH-type). However, appropriate adsorption/desorption strength cannot be ignored which also require the FM conductors to be with around unit e_g electron numbers.

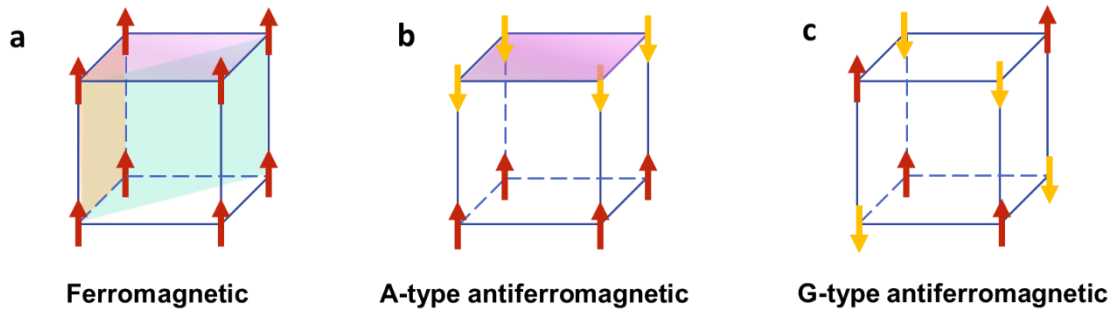

Figure 2.7 Types of magnetic interaction in the crystal lattice. (a) Ferromagnetic (FM); (b) G-type antiferromagnetic (G-AFM); and (c) A-type antiferromagnetic (A-AFM).

2.7 Influence of oxygen p band on the OER

Metal-oxygen co-valency and the computed center of the oxygen *p* band relative to the Fermi level have been also proposed as a descriptor of the OER activity and stability [79]. In oxides, hybridization of the metal *d* orbitals and O 2*p* orbitals occurs due to the spatial overlap and energetic similarity of the electronic states [28]. As shown in **Figure 2.8**, shifting the oxygen *p* band closer to the Fermi level, the metal *d* band mixed with the oxygen *p* band, and the redox center of the catalyst is no longer defined by the metal alone. As when anionic redox is activated, the lattice oxygen atoms also involved in the oxidation reaction, and O_2 molecule release step is linked to a phase with dynamic oxygen vacancies (oxygen vacancies can bring about higher magnetization and conductivity) [41]. This kind of lattice oxygen evolved reaction route will definitely result in faster kinetics and it has been observed for today's most active OER oxide catalysts [56]. In fact, the electrons from oxygen p band are spin polarized when they are at the Femi level in the situation of either lattice oxygen or oxygen vacancies evolved mechanism.

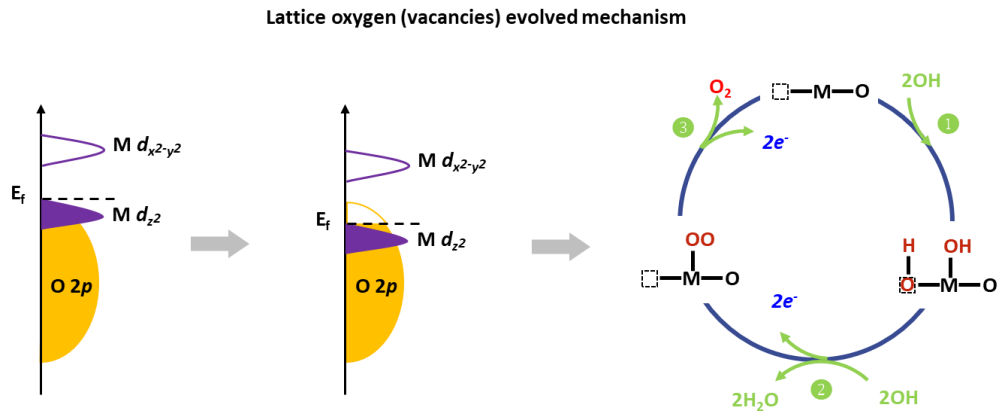

Figure 2.8 Possible OER mechanism induced by change of center of the oxygen *p* band relative to the Fermi level.

The degree of metal–oxygen hybridization can be tuned by the choice of transition metal ion and its oxidation state. For example, the number of d electrons and electronegativity increase when moving across a row on the periodic table, which can lower the metal d states below that of the oxygen 2*p* states, resulting in bonding metal d bands and antibonding oxygen 2*p* bands. It has been predicted that Fe 4+ ions have higher OER activity than Mn 3+ ions (isoelectronic d^6 configuration) and Co 5+ are also expected to have higher OER activity than Ni 6+ ions (d^4 configuration), due to the higher degree of metal–oxygen hybridization in their oxides [29].Yet, if the O *p*-band center is lifted too close to the Fermi level, the stability of electrocatalysts will be decreased [79].

2.8 Gaps in Literature

(1) Electron transportation behaviours in the spintrocatalytic OER process can be regarded as battlefield with two correlated parts, the frontline is the electron extraction from adsorbates by the active sites of electrocatalysts, and the backup is the electron transport in the bulk electrocatalyst. To meet the needs of surface frontline, that is, at least two electrons extracted with the same spin polarization, subsequent electron transport in the bulk section is expected to be with the same spin polarization to lower the overall energy consuming. In the most cases of OER electrocatalysts, there exists spin, charge, orbital, and lattice couplings, and a subtle change in one part may affect the situation as a whole, just like the butterfly effect. Although the complexity making it a big challenge to discern the specific roles and contributed proportion of each factors, it provides great freedom of artificially manipulation for better performance at the same time.

(2) Ideal OER electrocatalyst should preserve the capability to extract electrons with same spin from adsorbates as well as smooth spin polarized electron transport afterwards. Transition metal compounds with higher oxidation, appropriate crystal field and local coordination, around unit e_g electron, shorter bond length, and FM (or A-AFM, including ferrimagnetic case) exchange interaction will be highly desirable for enhancing the overall OER efficiency. By reducing the dimensional of the materials, in atomic thickness for example, bulk transportation part may be negligible and then there is higher degree of freedom to optimize for the fast surface reaction. However, if a single phase cannot simultaneously exhibit advantages mentioned above, a heterojunction of two phases may be a considerable choice.

2.9 Research Plans

To verify the conclusions above, a single-phase platform to investigate the roles of the composition and structure (charge and lattice) in tuning the electron configuration (spin) for higher OER efficiency was designed (**Chapter 4**). At the same time, a heterojunction platform to tune e_g electron number (charge and spin) and corona poling ferroelectric polarization (lattice and orbital) to improve the OER activity was designed (**Chapter 5**). Finally, a flexible platform to introduce large amounts of oxygen vacancies as well as offering the freedom manipulate the electronic structure of metal cations was designed (**Chapter 6)**.

Chapter 3

3 Experimental Methods

3.1 Materials Preparation method

3.1.1 Hydrothermal Method

Hydrothermal synthesis is a common method for synthesizing inorganic materials. The first step is dissolving the raw materials into a solution, and then the aqueous solution is sealed in an autoclave which includes a polytetrafluoroethylene (PTFE)-lined stainless-steel vessel. The autoclave is then heated to a certain temperature (below 220 ℃), while the pressure in the sealed autoclave varies from 1 MPa to 1 GPa. The disadvantages of hydrothermal/solvothermal synthesis are as follows:(1) the need of expensive autoclaves; (2) safety issues during the reaction process; (3) impossibility of observing the reaction process. However, compared with other methods for synthesizing materials, the hydrothermal reaction method shows evident advantages in controlling the material size and morphology, since the material will grow slowly under high temperature and pressure. Thus, it is always used to fabricate nanoscale materials with specific morphology. In addition, the hydrothermal reaction method is quite simple, because it contains less steps, and the reaction temperature is not very high, since the sealed autoclave can form the high-pressure environment. Furthermore, the chemical ratio is easy to control, especially for volatile materials. In this thesis, the nanomaterials used in Chapter 4 and Chapter 5are synthesized by the hydrothermal reaction method.

3.1.2 Solid State Method

The solid state reaction, which is also called a dry media reaction, is a chemical reaction system in the absence of a solvent, which is the most widely used method for preparing polycrystalline ceramics. Generally, in a typical solid state reaction process, raw materials are mixed thoroughly via a ball-milling machine or by the hand in an agate mortar, and then the mixed materials will undergo pre-sintering with the chemical reaction taking place at this stage. After the pre-sintering, the powders will be ground again, followed by pressing the powders into pellets for a second sintering at an appropriate temperature with the aim of forming the desired phases. The advantages of solid state reactions ripple throughout many industries. It is important to economics because the elimination of solvents means that products will cost less. This, in turn, will make those products cheaper to buy. With normal reactions, scientists need to

remove the residual solvent from the resulting product after a reaction has finished. Producing materials from a solid state reaction will mean that scientists are able to bypass the purification process. Eliminating the solvent from the reaction means that a solid state reaction produces more product than a normal reaction can. It also is more environmentally friendly. Since there is no solvent, there is no waste to eliminate at the end of the reaction. Although there are many benefits to developing solid state reactions, there are also many drawbacks. The ideal process should result in a homogeneous, or uniform, substance, and some solid state reactions do not. In addition, these reactions are, for obvious reasons, useless for reactions requiring solvents. In this thesis, the materials used in Chapter 6 are made by the solid state reaction.

3.2 Materials Characterization Techniques

3.2.1 Powder X-ray Diffraction (XRD)

Powder XRD is mainly used to identify crystal structures and phases of samples. Prior to analysis, the sample must be finely ground and homogenized. XRD signals occur due to constructive interference of monochromatic X-rays following diffraction through a crystalline sample when conditions satisfy Bragg's Law ($n\lambda = 2d\sin\theta$), where n represents any integer, λ represents the X-ray wavelength, d represents the distance between lattice planes, and θ represents the angle of incidence with the lattice plane. The XRD patterns were collected via a GBC-MMA X-ray diffractometer or Rigaku-TTR III X-ray diffractometer with a Cu Kα radiation (λ = 1.5418 Å) at room temperature in air.

3.2.2 Scanning Electron Microscopy (SEM)

A scanning electron microscope (SEM) is a type of electron microscope that produces images of a sample by scanning the surface with a focused beam of electrons. The electrons can interact with atoms in the sample and produce various signals, such as secondary electrons and backscattered electrons, which can be collected by detectors and form images of the sample. In addition, characteristic X-rays are produced by inner electron transitions, which can show the distribution of elements and compounds. With an energy dispersive spectroscopy (EDS) facility, the elemental composition can be analyzed immediately. In this thesis, the surface morphology and elemental information were characterized by JOEL JSM-7500F or JSM-6700F with an energy-dispersive X-ray spectroscopy facility.

3.2.3 Transmission Electron Microscopy (TEM)

In TEM a high-energy electron beam is transmitted through a sufficiently thin specimen, with the interaction between incident electrons and the specimen resulting in the formation of an image. TEM can

provide specimen information, including on morphology, crystal structure, and electronic structure. In addition, selected area electron diffraction (SAED) can be used to identify crystal structures and crystal defects. In this doctoral thesis, TEM was carried out using JEOL JEM-ARM200F, JEOL JEM-2011 and JEOL JEM-2100F transmission electron microscopes.

3.2.4 Scanning transmission electronic microscopy (STEM)

Scanning transmission electronic microscopy (STEM) is a type of TEM equipped with additional scanning coils, detectors, and the necessary circuitry. Unlike a traditional TEM, the electron beam in an STEM is focused to a fine spot, which is then scanned over the sample in a raster pattern. The raster pattern of the electron beam across the sample makes STEM suitable for several analysis techniques, such as annular dark-field imaging (ADF), electron energy loss spectroscopy (EELS), and elemental mapping by energy dispersive X-ray (EDX) spectroscopy. In this thesis, the crystal structure information was obtained from a JEOL ARM200F microscope. Elemental mapping was performed on the X-ray spectrometer attached to the JEOL ARM200F microscope.

3.2.5 Raman Spectroscopy

Raman spectroscopy is a widely used spectroscopic technique, and is mainly used to collect information on low-frequency vibrational and rotational modes in a system. The laser interacts with phonons, molecular vibrations, or other excitations, causing the energy of some of the laser photons to shift upward or downward. Such shifts in energy provide information on vibrational modes in the system, which are specific to certain chemical bonds and the symmetry of the molecules. In this doctoral thesis, all Raman spectra were collected using a SPEX-1403 Laser Raman spectrometer excited by a 532 nm wavelength Ar^+ laser.

3.2.6 X-ray Photoelectron Spectroscopy (XPS)

XPS is a surface-sensitive quantitative spectroscopic technique. Specifically, this technique can measure the elemental composition, oxidation state, quantity, and binding energies of a sample. XPS spectra are recorded by irradiating a sample with X-rays and measuring the kinetic energy and number of electrons with an escape depth of typically < 10 nm. XPS data in this doctoral thesis was collected using a SPECS XPS/Auger spectrometer or an ESCALAB 250 system (Thermo Scientific).

3.2.7 X-ray absorption spectra (XAS)

XAS is a powerful technique which has the ability to reveal the molecular structure and orientation at surfaces, interfaces and within thin films. Depending upon the energy of an absorbed X-ray, a core-level

electron can be excited to an unoccupied but bound molecular orbital, or to a free state above the vacuum level. The critical aspect is that the absorption cross section of X-rays near the binding energy of a core electron is highly sensitive to the local bonding environment of the atom; by carefully recording the absorption spectrum in this near-edge region, this bonding environment can be probed. Although a direct absorption measurement is challenging, there are several methods of indirectly measuring an absorption spectrum, including the total electron yield (TEY), partial electron yield (PEY), Auger electron yield (AEY), fluorescence yield (FY) and attenuation of the incident X-ray flux (X-ray transmission). The soft X-ray absorption spectra (XAS) were collected at the BL12B-a facility of the National Synchrotron Radiation Laboratory (NSRL, Hefei, P. R. China) using the synchrotron radiation from a storage ring running at 800 MeV with an average current of 300 mA, and Soft X-ray Spectroscopy beamline at the Australian Synchrotron (AS, Australia), BL14W1 facility of the Shanghai Synchrotron Radiation Facility (SSRF, P. R. China).

3.2.8 Brunauer, Emmett and Teller (BET) surface area

The BET theory is commonly used to evaluate the gas adsorption data and generate a specific surface area result expressed in units of area per mass of sample (m^2/g). This method is widely used for most materials, but is most reliable for materials with a Type II or Type IV isotherm with sufficient level of interaction between the adsorbate gas and the surface. Prior to analysis, the sample must be preconditioned to remove physically bonded impurities from the surface of the powder in a process called degassing or outgassing. The specific surface area of a material is then determined by the physical adsorption of a gas (typically nitrogen, krypton, or argon) onto the surface of the sample at cryogenic temperatures (typically liquid nitrogen or liquid argon temperatures). The BET surface area of samples in this doctoral thesis was estimated by using the adsorption data (Tristar II 3020M, Mircomeritics, USA, or BET Nova 1000, Quantachrome Instrument).

3.3 Physical property

3.3.1 Ferroelectricity Measurements

Ferroelectricity is a characteristic of certain materials that have a spontaneous electric polarization that can be reversed by the application of an external electric field. The polarization–electric field (P–E) loops that can directly reflect the spontaneous polarization inside were investigated with a Precision LC ferroelectric analyzer (Radiant Technology Product, USA) on the ceramic counterparts of the samples at room temperature.

3.3.2 Magnetic properties

Magnetization curves with two different modes: zero-field cooling (ZFC) and field cooling (FC) curves are informative for the electronic structure of a material. For ZFC mode, sample must be cooled without any applied magnetic field to the desired temperature, then data should be collected while heating with application of some magnetic field. While in the field cooling (FC) measurement, sample is cooled under certain applied magnetic field to the desired temperature, and collected the data while heating with application of some magnetic field. In this doctoral work, magnetization-temperature curves were measured under a 500 Oe magnetic field within the temperature range of 5–340 K on a Quantum Design physical properties measurement system (PPMS-9T) (Quantum Design, USA) with the vibrating sample magnetometer (VSM) option.

3.4 Electrochemical Characterization

3.4.1 Electrode preparation

To prepare the working electrode, 10 mg of electrocatalyst and 0.1 mL of 5 wt% Nafion® solution were dispersed in 0.75 mL deionized water and 0.25 mL methanol under ultrasound for 1 hour to form a mixed ink. 2 mg carbon powder was also added for some electrodes. Then, 3 μL of this solution was drop-casted onto a glassy carbon electrode 3 mm in diameter (effective area 7.065 mm^2) and dried naturally, yielding a catalyst loading of 0.38 mg cm^{-2}.

3.4.2 OER test system

Investigation of the electrocatalytic oxygen evolution reaction (OER) was performed on electrochemical workstations (CHI instruments 660E, or Ivium-n-Stat, Ivium Technologies) in a standard three-electrode electrochemical cell, with saturated Ag/AgCl, platinum wire, and a glassy carbon electrode coated with the electrocatalyst as the reference electrode, the counter electrode, and the working electrode. The potentials vs. Ag/AgCl were converted to reversible hydrogen electrode (RHE) according to the **Nernst Equation 3.1**:

$$E_{\mathrm{RHE}} = E_{\mathrm{Ag/AgCl}} + E^{0}_{\mathrm{Ag/AgCl}} + 0.059 * \mathrm{pH} \qquad (3.1)$$

Where E_{RHE} is the converted potential vs. RHE, $E^{0}_{\mathrm{Ag/AgCl}}$ = 0.1976 V, and $E_{\mathrm{Ag/AgCl}}$ is the measured potential. Afterwards, some potentials were corrected to compensate for the effect of solution resistance, by subtracting *iR* (where *i* is the current, and *R* is the uncompensated ohmic electrolyte resistance).

3.4.3 OER characterization techniques

Linear sweeping voltammograms (LSV) is a voltammetric method where the current at a working electrode is measured while the potential between the working electrode and a reference electrode is swept linearly in time.

Cyclic Voltammetry (CV) is an electrochemical technique which measures the current that develops in an electrochemical cell under conditions where voltage is in excess of that predicted by the Nernst equation. CV is performed by cycling the potential of a working electrode, and measuring the resulting current.

Tafel plot is a graphical plot (usually logarithmic) showing the relationship between the current generated in an electrochemical cell and the electrode potential of a specific metal. These plots are usually generated based on electrochemical experiments performed under controlled conditions. In order to measure the Tafel plot, open potential (V_o) was measured at first. Then Tafel plots were obtained under Tafel mode and the range was set as V_o~V_o+100 mV with the scan rate 5 mV s^{-1}.

Chronoamperometry is a time-dependent technique where a square-wave potential is applied to the working electrode. The current of the electrode, measured as a function of time, fluctuates according to the diffusion of an analyte from the bulk solution toward the sensor surface. Long term chronoamperometric measurements in this doctoral work were conducted at 1.5 V vs reversible hydrogen electrode (RHE) with scan rate 10 mV s^{-1}.

Electrochemical impedance spectroscopy (EIS) is an electrochemical technique to measure the impedance of a system in dependence of the AC potentials frequency, which was conducted with AC voltage with 5 mV amplitude at certain potential within the frequency range from 10^6 Hz to 0.1 Hz.

Chapter 4

4 Optimized electronic configurations to improve the surface absorption and bulk conductivity for enhanced oxygen evolution reaction

4.1 Introduction

Electrocatalytic water splitting holds great promise for the future energy conversion devices, but the kinetics of the sluggish oxygen evolution reaction (OER, $4OH^- = O_2 + H_2O + 4e^-$) is the rate-determining step and deserves to be studied extensively [80,56,81]. Transition metal compounds are the most promising non-precious-metal OER electrocatalysts, with the characteristics of low cost, relative abundance, and high electrocatalytic activity [82-85]. Recently, Yang Shao-Horn's research group revealed that the OER activity of transition metal perovskite oxides exhibited a volcano-shaped dependence on the number of e_g electrons [60]. This has led to one of the most promising strategies in material design to improve the OER performance of various perovskite oxides [61,62]. The perovskite $Ba_{0.5}Sr_{0.5}Co_{0.8}Fe_{0.2}O_{3-\delta}$ (BSCF) with the $(t_{2g})^5(e_g)^{1.2}$ electronic configuration of Co cations designed by following Yang Shao-Horn's principle has become the state-of-art OER electrocatalyst instead of IrO_2 [63]. Still, there are some fundamental issues should be addressed before further improvement in OER efficiency is possible. In the first place, this principle only emphasizes the effect of average e_g electron number and its relationship to absorption. As is well known, both electrical conductivity and adsorption capability are the key factors for the OER strongly, which all dependent on the electronic/spin configuration[86,87]. Therefore, more efforts are required to reveal the electronic/spin configuration effects on the other key factors, such as conductivity, as well as the absorption. Secondly, due to the fact that the electronic configuration is decided by the subtle balance between the crystal-field-splitting (Δ) and the intersite interaction energy (J, Hund's-rule coupling), a transition metal ion may be in several types of electron and spin configuration, depending on the crystal-field-splitting [88]. For instance, $3d^6$ Co ions can be in high spin $(t_{2g})^4(e_g)^2$, low spin $(t_{2g})^6(e_g)^0$, or intermediate spin states $(t_{2g})^5(e_g)^1$. Still and all, it is a challenge to substantially tune the crystal field in the perovskite to reveal the basic mechanism, considering its limited operating degrees of freedom.

In recent years, many members of the perovskite derivative family, such as layered perovskite $LaSr_3Co_{1.5}Fe_{1.5}O_{10-\delta}$, $PrBaMn_2O_{5+\delta}$ and double perovskite $NdBaMn_2O_{5.5}$, have been reported to have

excellent OER activity [55,89,90]. As derivatives of perovskites, layered perovskite oxides give more freedom to adjust both the composition and the structure due to the larger tolerance factor [91]. For example, in the layered Aurivillius-phase perovskite oxides with the formula $(Bi_2O_2)^{2+}(A_{n-1}B_nO_{3n+1})^{2-}$, A can be chosen from Na, K, Sr, Ca, Bi, etc., and B can be chosen from Ti, Fe, Ni, Co, Mn, etc., while the number of the perovskite layers *n* can range from 1 to 9 [92]. The plasticity of the composition and the crystal structure provide a powerful platform for both electronic structure and magnetic property manipulation in this material family. For instance, 6 layered $Bi_7Fe_3Ti_3O_{21}$ exhibits paramagnetic (PM)-like characteristics with a small proportion of weak antiferromagnetic (AFM) property; while an exchange bias phenomenon and spin glass (SG)-like characteristics can be observed in samples with more than 7 layers [93]. In the two-layered $La_{2-x}Sr_xCoO_4$, Co ions may change from d^7 to d^6 and then to d^5, together with an increased proportion in the intermediate spin (IS) state with increasing *x*. The lattice constant *a* and the Co-O bond length monotonically decrease with increasing *x* due to the reduction of the ionic radius resulting from the changes to oxidation states [94]. Here, we can see that a wide range of composition and structure changes, bringing about electronic structure variation, can be realized in the layered perovskite, which provides a wonderful platform to reveal the fundamental principles of the OER for more rational and effective designs.

In the present work, we attempt to study the roles of structure and composition evolution on the OER efficiency by doping cobalt into Fe sites in the layered perovskite $Bi_7Fe_3Ti_3O_{21}$. Three samples were prepared with the Co/(Fe+Co) of 0%, 50%, and 100%. The OER performance was enhanced more than 100 times from 0% to 100% Co, with the current density at 1.8 V vs. reversible hydrogen electrode (RHE) increased from 0.13 mA/cm^2 to 43 mA/cm^2 and the Tafel slope reduced from 656 mV/dec to 87 mV/dec. After careful crystal and electronic structure analysis, we found that Co ions are in the intermediate spin (IS) state due to the appropriate crystal field splitting. This kind of electronic configuration facilitates fast electron transfer in bulk and moderate bonding with surface reactants, resulting in enhanced conductivity, appropriate adsorption capability, and thus, the tremendously improved OER efficiency.

4.2 Experimental

In a typical synthesis, 1.2 g $Ti(OC_4H_9)_4$ (> 99.7%) was first dissolved into a 4 M HNO_3 solution (7.5 mL), and then $Bi(NO_3)_3{\cdot}5H_2O$ (> 99%), $Fe(NO_3)_3{\cdot}9H_2O$ (> 98.5%) and $Co(NO_3)_2{\cdot}6H_2O$ (> 99%) were added respectively in the stoichiometric ratio according to the formula $Bi_7Fe_{3-x}Co_xTi_3O_{21}$ (x = 0, 1.5, and 3, with the samples denoted as BFTO, BFCTO, and BCTO respectively). After 20 minutes of magnetic stirring,

the homogeneous metal-ion solution was added into a 1.66 M NaOH solution (70 mL). Afterwards, the resulting slurry was transferred into a Teflon-lined stain-less steel autoclave (total capacity of 100 mL). The autoclave was sealed and heated at 200 °C for 2 days, before being naturally cooled down to room temperature (RT). The sediments were washed with water and ethanol several times and then dried at 60 °C for 8 hours.

The purity and crystallinity of the as-prepared samples were characterized by X-Ray powder diffraction (XRD) with the XRD patterns recorded on a Rigaku-TTR III X-ray diffractometer with Cu-Kα radiation. X-ray photoelectron spectroscopy (XPS) analysis was performed using an ESCALAB 250 system (Thermo Scientific). Magnetic properties were characterized by the vibrating sample magnetometer (VSM) option of a Quantum Design physical property measurement system (PPMS) (Quantum Design, USA). The soft X-ray absorption spectra (XAS) were collected at the BL12B-a facility of the National Synchrotron Radiation Laboratory (NSRL, Hefei, P. R. China) using the synchrotron radiation from the storage ring running at 800 MeV with an average current of 300 mA. The Brunauer-Emmett-Teller (BET) surface area was estimated by using the adsorption data (Tristar II 3020M, Mircomeritics, USA).

Electrochemical measurements were performed on an electrochemical workstation (CHI instruments 660E, China) in a standard three-electrode electrochemical cell, with saturated Ag/AgCl, platinum wires and a glassy carbon electrode coated with electrocatalyst as the reference electrode, counter electrode, and working electrode. To prepare the working electrode, 10 mg of electrocatalyst and 0.1 mL of 5 wt % Nafion® solution were dispersed in 0.75 mL deionized water and 0.25 mL methanol, and then ultrasonicated for 1 hour to form a mixed ink. 3 μL of this solution was drop-casted onto a glassy carbon electrode 3 mm in diameter (effective area 7.065 mm^2) and dried naturally, yielding a catalyst loading of 0.38 mg/cm^2. Linear sweep voltammograms (LSV) were obtained at a scan rate of 5 mV/s. Electrochemical impedance spectra (EIS) were collected with AC voltage 5 mV in amplitude at the potential of 1.686 V vs. RHE within the frequency range from 10^6 Hz to 0.1 Hz. The potentials vs. Ag/AgCl were converted to RHE according to the Nernst equation:

$$E_{\mathrm{RHE}} = E_{\mathrm{Ag/AgCl}} + E^{0}_{\mathrm{Ag/AgCl}} + 0.059 * \mathrm{pH} \qquad (4.1)$$

Where E_{RHE} is the converted potential vs. RHE, $E^{0}_{\mathrm{Ag/AgCl}}$ = 0.1976 V, and $E_{\mathrm{Ag/AgCl}}$ is the measured potential against RHE and the Ag/AgCl reference.

4.3 Crystal structure

XRD patterns from the as-prepared samples are displayed in **Figure 4.1**, all of which can be indexed to

the Aurivillius layered perovskite structure. The crystal structure parameters as refined by the Pawley method are listed in **Table 4.1**. BFTO can be indexed with a six-layer Aurivillius structure with a = 5.475, b = 5.454, and c =58.046 Å. BFCTO can be indexed with a four-layer Aurivillius structure with a = 5.424, b = 5.437, and c = 40.993 Å, while BCTO has a four-layer Aurivillius structure with a = 5.429, b = 5.444, and c = 41.042 Å. Accordingly, BFTO has the nominal composition of $Bi_7Fe_3Ti_3O_{21}$, BFCTO has the nominal composition of $Bi_5Fe_{0.5}Co_{0.5}TiO_{15}$, and BCTO has the nominal composition of $Bi_5CoTi_3O_{15}$.

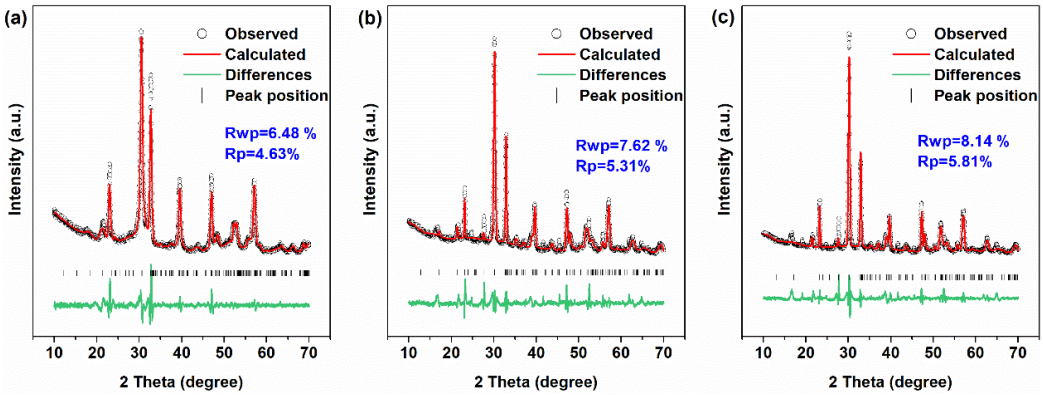

Figure 4.1 XRD patterns of the as-prepared samples. (a) BFTO; (b) BFCTO; (c) BCTO.

The bond lengths of Fe-O, and Co-O in the octahedra (L) of all the samples is also listed in **Table 4.1**, where L1, L2 refer to the axial lengths and L3-L6 are the apical lengths. In all the samples, octahedra from the perovskite-like layers are elongated along the axial direction, i.e., the c axis, when compared with ideal perovskite octahedron. It seems that the distortion of oxygen octahedra is greater, however, regarding to great disparity of the L values in the BFTO, compared to the BFCTO and BCTO. This is not caused by the ionic radius difference between Fe and Co, since the distribution of L value in the BFCTO and BCTO is similar with the same layer. Therefore, it might be due to the fact that BFTO has more layers of perovskite and a larger unit cell, which is less thermodynamically stable, and the oxygen octahedra may be self-regulated more drastically for the sake of lower energy.

Table 4.1 Crystal structure parameters in Å refined from the measured XRD patterns.

Sample	BFTO	BFCTO	BCTO
a	5.4750	5.4240	5.4290
b	5.4540	5.4370	5.4440
c	58.0460	40.9930	41.0420
L1	1.9240	2.0260	2.0260
L2	1.8940	2.0100	2.0090
L3	1.5800	1.9340	1.9340
L4	1.5800	1.9340	1.9340

L5	2.3380	1.9340	1.9340
L6	2.3380	1.9340	1.9340

4.4 Electronic structure

Ti *L*-edge XAS spectra of all as-prepared samples are shown in **Figure 4.2a**. Each consists of two sets of branches: one set is the lower energy L_3 and the other set is the higher energy L_2 due to the spin-orbit splitting of the 2*p* core states. Then, both of them are further split into t_{2g} and e_g states by the octahedral ligand field. Two peaks situated at around 458 eV and 460 eV represent absorption of electron transitions from the Ti L_3 2*p* core levels to the split lower energy t_{2g} and higher energy e_g orbitals, respectively. The other two peaks at 464 eV and 466 eV are from Ti L_2 2*p* to t_{2g} and e_g levels, respectively. By comparing with $SrTiO_3$ (Ti^{4+}) and $LaTiO_3$ (Ti^{3+}), the oxidation states of Ti are confirmed to be 4+ with the $3d^0$ configuration in all samples. Fe $L_{2,3}$ spectra of BFTO and BFCTO are displayed in **Figure 4.2b**, and the peaks around 709.5 eV (L_3) and 722.1 eV (L_2) are due to the spin-orbit splitting of Fe 2*p* core levels. The spectra of α-Fe_2O_3 and FeO were also collected for comparison, and from the peak positions, it was confirmed that the oxidation states of Fe ions in BFTO and BFCTO are mainly 3+. Co $L_{2,3}$ edge spectra are almost the same as each other for BFCTO and BCTO, as shown in the **Figure 4.2c**. The two absorption peaks located at 778.7 eV (L_3) and 793.5 eV (L_2) are due to the spin-orbit splitting of +3 Co 2*p* states, as shown by comparing them with the references CoO (Co^{2+}) and $LaCoO_3$ (Co^{3+}) $L_{2,3}$-edge. By the way, even though the measured Fe and Co *L*-edge spectra do not perfectly coincide with the standard substances due to the different spin states [95], the three transition metals Ti, Fe, and Co can still be confirmed to be mainly in the 4+, 3+, and 3+ states, respectively, according to their consistent peak positions.

The bismuth core level splits into $4f_{5/2}$ and $4f_{7/2}$ spin-orbit components, as shown in **Figure 4.2e**. There is no obvious disparity in the energy difference between the two peaks of the three samples, indicating that the bismuth valence state stays unchanged at 3+ unchanged [96]. The O 1s spectra (**Figure 4.2f**) of the three samples have two peaks with binding energy (BE) at about 529.6 eV and 531.4 eV; the main peak located at 529.6 eV is assigned to the lattice oxygen (P_o), and the later shoulder peak is assigned to the less electron-rich oxygen species [97], such as surface adsorbed oxygen (P_s). We define the area ratio of P_s/P_o as R_{so}, and it can be clearly seen that R_{so} increases from 9% in BFTO to 15% in BFCTO and reaches 27% in the BCTO sample. This result indicates that the capacity for absorbing oxygen intermediates is enhanced with increasing Co, which is likely to be rooted in the intrinsic electronic structure of Co.

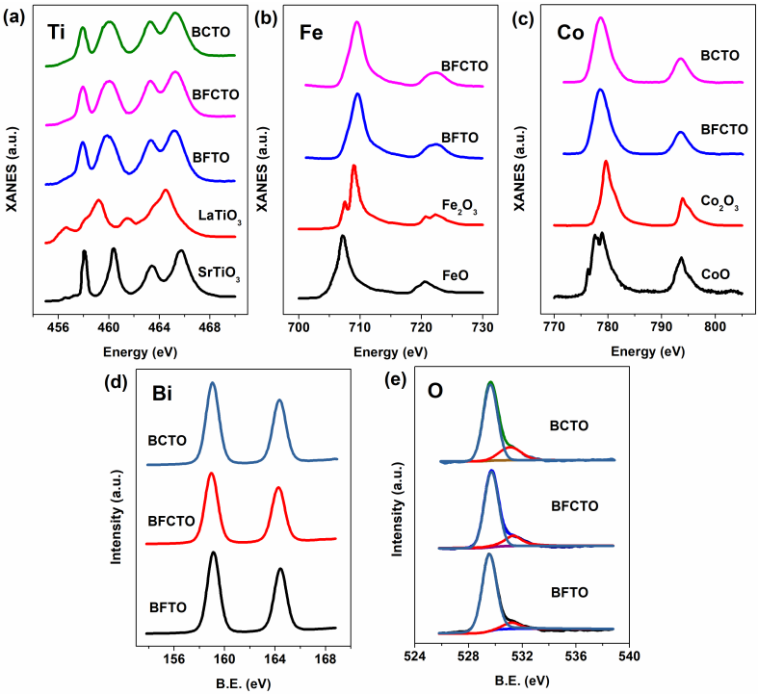

Figure 4.2 XAS spectra for the as-prepared samples. (a) Normalized Ti *L*-edge XAS spectra; (b) normalized Fe *L*-edge XAS spectra; (c) normalized Co *L*-edge XAS spectra. XPS core level spectra: (d) Bi 4f; (e) O 1s.

Therefore, magnetic properties, which are strongly related to the electronic configuration and exchange interaction, were measured in order to reveal the truth. **Figure 4.3a-c** shows the magnetization – magnetic field (*M-H*) hysteresis loops at room temperature (RT) of BFTO, BFCTO, and BCTO samples, respectively. Obviously, BFTO and BCTO have an almost linear feature, while BFCTO exhibits a well-defined hysteresis loop. This suggests that the ground magnetic state of BFCTO is ferromagnetic or ferrimagnetic at RT, while BFTO and BCTO are paramagnetic. Still, small loop-like features can also be observed in both BFTO and BCTO. The zero-field cooling (ZFC) and field cooling (FC) curves under 500 Oe magnetic field are further provided in **Figure 4.3d**, from which we can see that the FC-ZFC curves of BFTO obviously start to diverge above room temperature. This suggests the coexistence of weak ferromagnetism with the paramagnetic state in this material [98], while for the BCTO sample (**Figure 4.3f**), the FC-ZFC curves distinctly diverge around 50 K with two peaks at a lower temperature, indicating the existence of the spin glass state and a weak ferromagnetic interaction. On the contrary, BFCTO exhibits a typical "λ" ferromagnetic feature as displayed in the **Figure 4.3e**.

The evolution of inverse magnetic susceptibility dependence on temperature was obtained based on the FC curves of BFTO and BCTO (insets of **Figure 4.3d** and **4.3f**). The reciprocal slope is the Curie-Weiss

constant *C*, and both samples have a positive linear correlation, suggesting Curie-Weiss paramagnetism [99]. According to the following equations, the effective magnetic moment, μ_{eff} and the average e_g electron number can be estimated based on the quenching of orbital angular momentum (L = 0) for 3d transition metals and a measured g factor.

$$\frac{1}{\chi} = \frac{1}{C}T + \frac{T_C}{C} \qquad (4.2)$$

Where χ, C, T, and T_C represent the magnetic susceptibility, Curie-Weiss constant ($C > 0$), temperature, and Curie point, respectively.

$$\mu_{eff} = \sqrt{\frac{3kC}{N}} \qquad (4.3)$$

Where μ_{eff} is the effective magnetic moment, k is the Boltzmann constant, C is the Curie-Weiss constant, and N is the number of magnetic ions in the unit cell (N = 1, because there is only one Co atom per unit cell in BCTO or BCO).

$$\mu_{eff} = g\sqrt{J(J+1)}\mu_B \qquad (4.4)$$

Where g is the Lande factor, J is total quantum number, and μ_B is the Bohr magneton. (g can be approximated by 4.2 in $Bi_6Fe_2Ti_3O_{18}$ [100].)

On average, Fe ions are calculated to be in the high spin (HS) state $(t_{2g})^3(e_g)^2$, while Co ions are in the intermediate spin (IS) state $(t_{2g})^5(e_g)^1$. The ferromagnetism of BFCTO is the result of possible coupling of Fe-O-Co octahedral clusters when the concentrations of iron and cobalt ions are approximately equal [101]. The appearance of weak ferromagnetism in the paramagnetic ground state may have arisen from the nanosized morphology (10 nm thick nanoplates) which induces a certain amount of spin-canting on the surface [98].

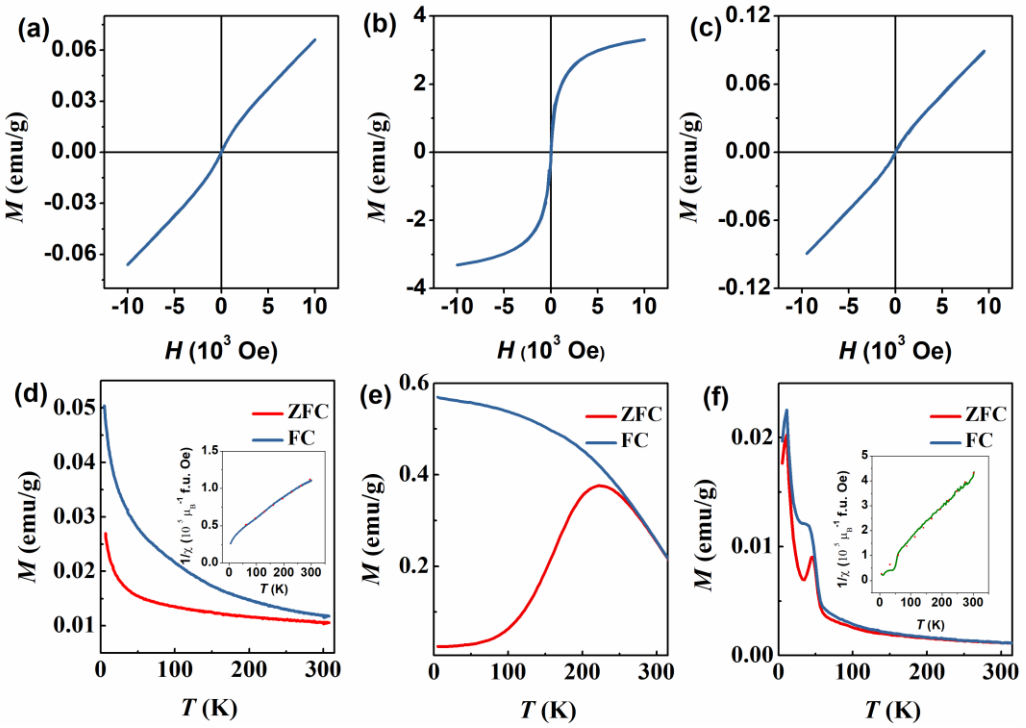

Figure 4.3 Magnetic characterization. *M-H* hysteresis loops of (a) BFTO; (b) BFCTO; (c) BCTO. FC-ZFC curves (500 Oe) of (d) BFTO; (e) BFCTO; (and f) BCTO respectively; insets are the inverse magnetic susceptibility versus temperature.

4.5 OER performances

OER efficiency is improved dramatically in the presence of cobalt, which can be observed in the linear-scan voltammetry (LSV) curves in **Figure 4.4a**. The current density at 1.8 V vs. RHE was extracted from the LSV curves to compare the OER activity. It increases from 0.13 mA/cm^2 to 5.16 mA/cm^2, and then to 43 mA/cm^2 on the BFTO, BFCTO, and BCTO samples, respectively. This improvement is confirmed by the Tafel plots in **Figure 4.4b**, the slope of which is reduced from 656 mV/dec for BFTO to 87 mV/dec for BCTO. Nyquist plots from the electrochemical impedance spectroscopy (EIS) experiments are provided in **Figure 4.4c**. An equivalent circuit composed of R_s, R_p, and CPE is proposed to resolve these spectra (the inset), where R_s represents the solution resistance, R_p represents the polarization resistance of the samples, and CPE is the constant phase element. The R_p value reflects the resistance of the electrocatalyst when performing as the electrode under a certain applied voltage. It decreased from 2014 Ω to 43 Ω with increasing cobalt content, indicating that the presence of Co could greatly improve the conductivity of the material.

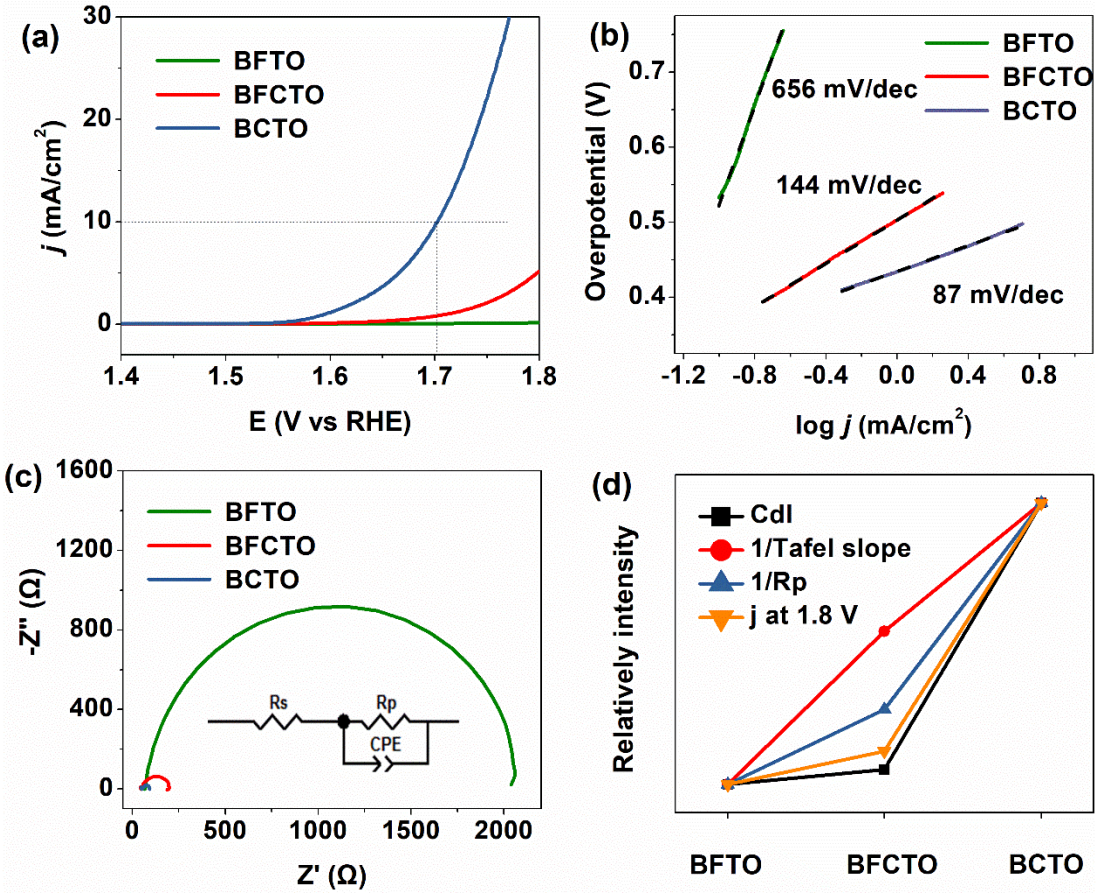

Figure 4.4 OER performance of samples. (a) LSV polarization curves; (b) Tafel plots; (c) Nyquist plots; (d) C_{dl}, reciprocal of the Tafel slope, reciprocal of R_p, and current density (j) at 1.8 V vs. RHE for the three samples.

The electrochemically active surface area (ECSA) reflect more intrinsic property of the electrocatalysts and it is proportional to the double layer capacitance C_{dl} (ECSA=Cdl/Cs, Cs usually treated as a constant). From the parameters resolved from Nyquist plots (**Table 4.2**), C_{dl} can be calculated according to the following equation:

$$C_{dl} = (\frac{T}{Rs^{P-1}})^{\frac{1}{P}}/S \qquad (4.5)$$

It is 174 μF/cm^2, 554 μF/cm^2 and 4193 μF/cm^2 for BFTO, BFCTO, and BCTO respectively, justifying the strong ability to hold electrons of BCTO. The C_{dl}, reciprocal of the Tafel slope, reciprocal of R_p, and current density at 1.8 V vs. RHE for the three samples are plotted in **Figure 4.4d** to show the visible upward tendency of OER descriptors with increasing cobalt. To confirm the tendency when considering the effects of the number of active sites, BET surface area and adsorption/desorption curves are measured and presented in **Figure 4.5a-4.5c**. As we can see, these three samples have the similar BET surface area,

and their normalized LSV curves by BET surface area are also consistent with above results and conclusions (**Figure 4.5d**).

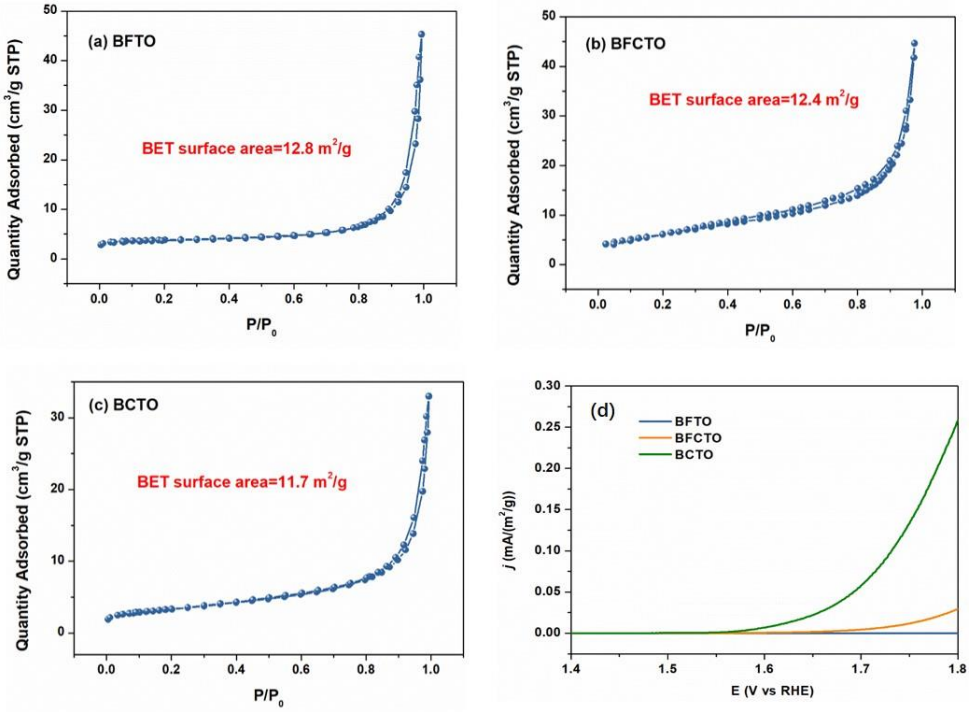

Figure 4.5 N2 adsorption and desorption isotherms plots of (a) BFTO; (b) BFCTO; (c) BCTO and LSV polarization curves normalized by corresponding measured BET surface area.

In addition, as Aurivillius phase have attracted tremendous attention as the famous ferroelectrics [99,102], we measured the P-E hysteresis loop of BCTO at room temperature in **Figure 4.6a**. It clearly illustrates that there exists intrinsic ferroelectric polarization in BCTO, which make it possible to be poled via the corona poling method. As shown in **Figure 4.6b**, the OER activity of poled BCTO sample is far beyond the commercial state-of-art IrO_2. The overpotential at the current density j=10 mA/cm^2 ($\eta_{j=10}$) we measured for poled BCTO is 350 mV, which is much smaller than $SrNb_{0.1}Co_{0.7}Fe_{0.2}O_{3-\delta}$ (SNCF, 500 mV), $Ba_{0.5}Sr_{0.5}Co_{0.8}Fe_{0.2}O_{3-\delta}$ (BSCF, 530 mV) and $SrCo_{0.8}Fe_{0.2}O_{3-\delta}$ (SCF, 510 mV) [63]. It's probably due to the further improved electron separation and transfer during the OER process and further work to reveal the improvement mechanism is undergoing.

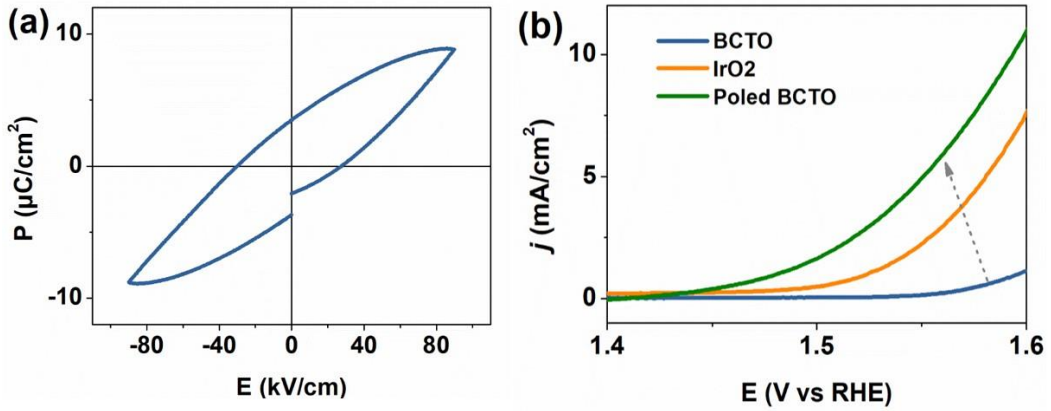

Figure 4.6 (a) P-E hysteresis loop of BCTO, (b) LSV curves for comparison with IrO2 and the potential further improvement by corona poling of the ferroelectric BCTO sample (The overpotential at the current density j=10 mA/cm^2 ($\eta_{j=10}$) for poled BCTO is 350 mV).

Table 4.2 Parameters resolved from Nyquist plots.

Sample	R_p(Ω)	R_s(Ω)	T(CPE)	P(CPE)	S(cm^2)
BFTO	2014	69.95	1.91E-5	0.9397	
BFCTO	153.1	47.81	1.00E-4	0.8483	0.07065
BCTO	43.10	51.86	6.03E-4	0.8298	

4.6 Discussion

From the analysis of XRD pattern we notice that doping cobalt decreases layer number of the perovskite in the crystal structure from six (BFTO) to four (BFCTO and BCTO). This speculation is based on the layered characteristic along the *c* axis of Aurivillius phase, with the lattice parameter *c* valued near 3.28 nm for 3-layered one, 4.12 nm for 4-layered one, and 5.76 nm for 6-layered one. The layer number of Aurivillius phase is decided by the stochiometric ratio of starting materials as well as the thermodynamics during synthesis, in general. Obviously, doping cobalt brings about changes in two aspects: crystal structure and composition. So four-layer Aurivillius structure $Bi_5FeTi_3O_{15}$ (denoted as BFTO-ref) with identical crystal structure to the BFCTO and BCTO may be a better reference[103]. $Bi_5FeTi_3O_{15}$ was synthesized with the same method (denoted as BFTO-ref) and its XRD pattern and refined parameters are displayed in **Figure 4.7a**. From the refined crystal structure results we know that, the length of transition metal-oxygen L is with almost the same in BFTO-ref, BFCTO and BCTO, which may be mainly decided by the layer number of the perovskite. Distorted oxygen octahedrons are drawn in **Figure 4.7b** according to the refined parameters for the BFTO, BFCTO, BCTO, and BFTO-ref samples. The oxygen octahedron

is more distorted in the six-layered BFTO than the other three four-layered samples.

Figure 4.7c demonstrate the comparison of OER performance between BFTO-ref and BFTO, from which it can be observed that electrocatalytic activity of four-layered BFTO-ref and six-layered BFTO are not much different, and BFTO-ref even worse than the BFTO. It suggests that the dramatically enhanced OER performance of BFCTO and BCTO is not from the layer number decrease. The slightly different performance between six-layer BFTO and four-layer BFTO-ref may originate from the advantageous electronic configuration of BFTO with higher degree of oxygen distortion. For example, three t_{2g} orbitals and two e_g orbitals could be further split, and the short bonding length means more overlap with oxygen 2*p* orbital. Nevertheless, the disadvantage in the crystal structure do have effect on the OER performance but it's overwhelmed by the different element composition.

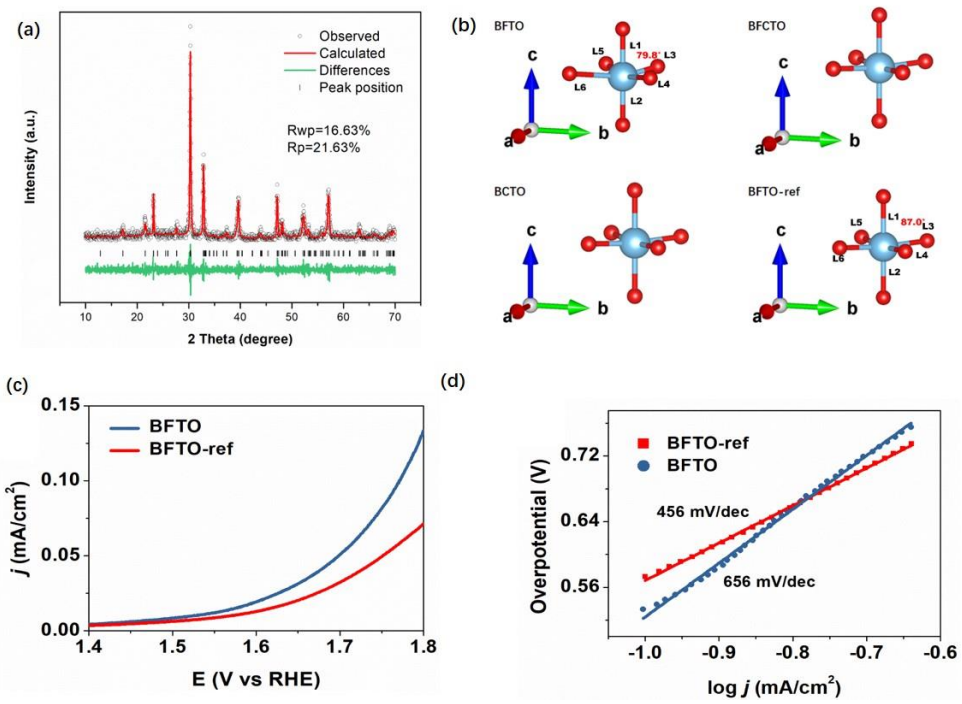

Figure 4.7 (a) XRD patterns of BFTO-ref samples. (Parameters: 4-layered perovskite, a=5.4456 Å, b=5.4474 Å, c=41.159 Å, L1=2.009 Å, L2=2.025 Å, L3=1.928 Å, L4=1.928 Å, L5=1.928 Å, L6=1.928 Å); (b) Distorted oxygen octahedrons drawn according to the refined parameters for as-prepared samples; (c-d) LSV polarization curves and Tafel plots of BFTO and BFTO-ref.

We can propose a scenario where an electron is transferred from adsorbates to electrocatalyst surface (step 1), and then transferred to adjacent ions in bulk and finally to the anode (step 2), accompanied by the oxygen molecular desorption (step 3). In the octahedral environment, the e_g orbitals (d_{z^2}, $d_{x^2-y^2}$) have strong spatial overlap with those of adjacent O 2*p* orbitals, forming σ-bonding and σ*-antibonding

states with partial metal and oxygen character while t_{2g} have weaker spatial overlap with nearby O 2p orbitals and form π bonds and π* anti-bonds. It is assumed that the σ-interaction dominates over the weaker π-interaction. The high energy orbital parentage is considered to more easily react with oxygen-related adsorbates due to their matched energies compared to other orbitals. Therefore, higher unoccupied e_g orbitals parentage facilitates the rate of the step 1. For step 3, it's just opposite to the step 1, so the optimized eg electron occupation is around unit, just as in Yang Shao-Horn's volcano-shaped dependence on the e_g electron number [60]. For step 2, the coherent relocation from one orbital to the neighbor is possible only if there is not already an electron of the same spin occupying that orbital. So, it is easier for the electrons near Fermi level to transfer from one ion to the adjacent ion with the energy-matched empty orbital. In this situation, the additional pairing energy is avoided. However, once the incoming electron has enough energy to be paired with the opposite spin electron, it will be difficult to keep transferring afterwards.

At first, the chemisorption bonding of surface ions with Co (3+, IS, $(t_{2g})^5(e_g)^1$) has an appropriate strength for a compromise between the absorption of reactants (step 1) and the desorption of products (step 3) (**Figure 4.8a**). Secondly, it only requires low energy to provide an instantaneous change of state from $(t_{2g})^5(e_g)^1$ to $(t_{2g})^5(e_g)^2$ (step 2), as electron will located in the empty $d_{x^2-y^2}$ orbital which needs no consumption of pairing energy (*P*). There is a possibility that the electron is paired and stabilized in d_{xy}, when the crystal field splitting energy (Δ) is larger than the pairing energy (*P*) [104]. However, the existence of the ground state of IS Co^{3+} justifies that this situation may not be happen, or HS Co^{3+} will appear instead. Fe (3+, HS) with $(t_{2g})^3(e_g)^2$, however, without any empty orbital but consuming additional pairing energy (*P*) , may be not as generous as IS Co in terms of sharing the orbital with adsorbates (step 1) as well as harboring electrons during the electron transfer in bulk (step 2) (**Figure 4.8b**). As Co^{3+} ion is usually in low spin (LS) or high spin (HS) state in some oxides such as $LaCoO_3$, and IS state occurs when there is favorable crystal structure and composition [105]. So, HS and LS $Co^{3+}$are also offered for to understand the superiority of IS Co^{3+} (**Figure 4.8c** and **4.8d**). In Co (3+, LS, $(t_{2g})^6(e_g)^0$) case, it's easier to adsorb species due to strong chemisorption bonding but it's harder to desorb afterwards (step 3 is rate-limiting), although it may give rise to high electronic conduction. For the situation of Co (3+, HS, $(t_{2g})^4(e_g)^2$), it is with the same situation as in the Fe (3+, HS, $(t_{2g})^3(e_g)^2$). Unfortunately, we found it very intractable to conduct computation such as through *ab initio* density functional theory (DFT) or other material computation methods to provide more solid evidence, mainly due to the too large unit cell of

layered perovskite.

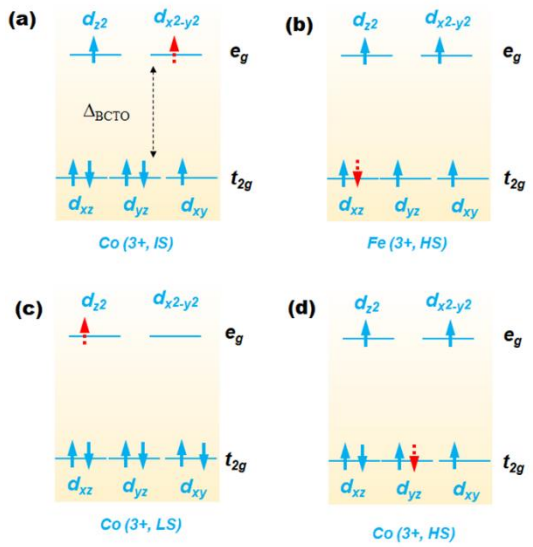

Figure 4.8 Possible mechanism for the better OER performance of IS state cobalt.

4.7 Conclusions

Three layered perovskite oxides with different compositions and structures, all Fe based, half-half Fe-Co based, and all Co based, were successfully prepared as an excellent platform to investigate the role of electronic structure in the OER efficiency. Refinements of measured XRD patterns suggested that doping Co ions cause the decrease of the perovskite layer number, but it has negligible effects on the OER activity. The elongation along the *c*-axis stabilized with Co ions in the intermediate spin (IS) state, which is further confirmed by the XAS spectra and magnetic measurements. All the elements are in the consistent oxidation state according to the XAS and XPS spectra, but there are more surface absorbed oxygen species with increasing Co. The electronic configurations of iron and cobalt ions are calculated to be $(t_{2g})^3(e_g)^2$ and $(t_{2g})^5(e_g)^1$, respectively, based on the FC curves and Curie-Weiss law. The OER performance of the all Co based oxide is 100 times higher than for the all Fe based one, with the following respective comparisons: (1) current density of 43 mA/cm^2 compared to 0.13 mA/cm^2 (1.8 V vs. RHE); (2) Tafel slope of 87 mV/dec compared to 656 mV/dec; (3) polarization resistance of 43 Ω compared to 2014 Ω; (4) double layer capacitance of 4193 μC/cm^2 compared to 174 μC/cm^2. For these incredible improvements, we also provide a possible mechanism. This work offers a new idea for developing novel high-efficiency OER electrocatalysts for future energy conversion devices.

Chapter 5

5 Enhancing oxygen evolution efficiency of multiferroic oxides by spintronic and ferroelectric polarization regulation

5.1 Introduction

The oxygen evolution reaction (OER) process not only involves four sequential proton coupled electron transfers, but also includes a transition of the spin states of the reactants from the singlet OH^-/H_2O to the triplet O_2 [25,71]. Such a spin transition needs to be promoted by an additional stimulus, such as enough voltage and spin orbital coupling, in order to proceed. So, it has been the rate-determining step that hinders applications in various energy conversion and storage devices [56]. Due to the scarcity and high cost of commercial OER catalysts such as Pt and magnetic RuO_2/IrO_2, a great deal of effort has been expended on possible alternatives [2]. Transition metal based perovskite is one of the most excellent candidates, owing to its low cost, relatively good stability, and high electrocatalytic activity [83]. In 2011, Yang Shao-Horn et al pointed out that the intrinsic OER activity of perovskite oxides exhibited a volcano-shaped dependence on the number of e_g electrons of surface transition metal cations [60]. Following this rule, the fastest OER is observed on $Ba_{0.5}Sr_{0.5}Co_{0.8}Fe_{0.2}O_{3-\delta}$ (BSCF), in which the magnetic ions are in the intermediate spin state, that is, the number of e_g electrons is around 1.2. Since then, this principle has become an effective guideline to improve the efficiency of perovskite oxide OER catalysts [83]. For example, by reducing the nanoparticle size of $LaCoO_3$ to 80 nm, Zeng's group successfully increased e_g filling of cobalt ions from unity to 1.2 and reduced the overpotential (330 mV) and Tafel slope (69 mV dec^{-1}) [62]. Wu's groups adjusted the e_g electron number of $LaCoO_3$ films to 1.2 by different degrees of octahedral distortion, resulting in an overpotential of 470 mV [61]. Yang Shao-Horn's group also acquired insight into several 6-fold coordination motifs of transition metal oxides, such as face-sharing, corner sharing, and distorted prism. Whether this rule is applicable in the composites remains unclear, however, considering composites with the combination of two or more different coordination may provide flexible tuning of average e_g electron numbers in contrast to the rigid single phase only.

Therefore, new strategies should also be explored to further improve the efficiency to meet the requirements of practical applications. Ultrathin two-dimensional (2D) morphology engineering for maximum surface area is one of the most effective approaches that have been recently developed [106].

For example, an atomically thin cobalt oxyhydroxide nanosheet had performance 20 times higher than that of its bulk counterpart and 2.4 times higher than that of the benchmark IrO_2 electrocatalyst for water oxidation [107]. Even so, it must be pointed out that atomic two-dimensional morphology usually requires subtle and intricate multi-step soft chemistry routes with low production. Excitingly, it has been discovered that the internal polarization of ferroelectrics can help to promote the separation and transport of carriers [108-113]. Meanwhile, ferroelectrics also produce an external screening effect, adsorbing charged ions and molecules from outside to neutralize their polarization inside [114-118], which may provide a valuable way to enhance the adsorption capacity that is not yet fully utilized in OER process. Inspired by the above-mentioned spin state effects and ferroelectric polarization function, we considered the multiferroic layered perovskite oxides as an excellent material matrix to demonstrate possible new strategies to further improve the OER efficiency [119,120]. As perovskite derivatives, layered perovskites preserve multiple perovskite physical parameters such as couplings between charge, spin, orbitals, and the lattice, and have attracted tremendous attentions for multiferroic and energy conversion devices [99,102]. More importantly, layered perovskite oxides have higher degrees of freedom in their structure and are amenable to properties modulation by component substitution or layer number regulation.

Herein, we propose a method to improve the OER activity: in-situ grown a secondary phase on a ferroelectric matrix to tune e_g electron number and corona poling ferroelectric polarization afterwards. It is started with the deliberately insertion of several layers of $BiCoO_3$ (BCO) into the 3-layered perovskite $Bi_4Ti_3O_{12}$ (BTO). According to our previous works, the structure of 3-layered perovskite $Bi_4Ti_3O_{12}$ (BTO) can be maintained when inserting 3 layers of $BiFeO_3$, but only one layer of $BiCoO_3$ is achievable due to the structural tolerance for smaller Co cations. Thus, from considerations of structural tolerance and thermodynamic stability, only one layer of BCO can be inserted to form a 4-layered perovskite oxide $Bi_5CoTi_3O_{15}$ (BCTO), while the residual BCO would be deposited in situ on its surface as the secondary phase. This configuration provides an excellent research platform to reveal the roles of the electronic regulation, as well as ferroelectric polarization on the OER performance. In order to manifest the reinforcement on the OER activity of the ferroelectric polarization, corona poling was applied afterwards which turned out to be very effective, resulting in a superior OER performance with 320 mV overpotential at the current density of 10 mA cm^{-2} and 34 mV dec^{-1} Tafel slope. The electronic structure and the contribution of the ferroelectric polarization were studied in detail by various tests and measurements, and a possible enhanced mechanism is proposed.

5.2 Experimental Methods

5.2.1 Synthesis

In a typical synthesis, 1.2 g $Ti(OC_4H_9)_4$ (> 99.7%) was first dissolved into 4 M HNO_3 solution (7.5 mL), and then $Bi(NO_3)_3{\cdot}5H_2O$ (> 99%), and $Co(NO_3)_2{\cdot}6H_2O$ (> 99%) were added with the stoichiometric ratio according to $Bi_4Ti_3O_{12}{\cdot}n(BiCoO_3)$ (n = 1, 2, 3, 4), with the products denoted as Co1, Co2, Co3, and Co4, respectively). After 20 min of magnetic stirring, the homogeneous metal-ion solution was added into a 1.66 M NaOH solution (70 mL). Afterwards, the resulting slurry was transferred into a Teflon-lined stainless autoclave (total capacity of 100 mL). The autoclave was sealed and heated at 200 °C for 2 days, then cooled down to room temperature (RT) naturally. The sediments were washed with water and ethanol several times and then dried at 60 °C for 8 hours.

5.2.2 Materials characterization

The purity and crystallinity of the as-prepared samples were characterized by X-Ray powder diffraction (XRD) with the patterns recorded on a Rigaku-TTR III X-ray diffractometer with Cu-Kα radiation. The morphologies of the powders were observed by scanning electron microscopy (SEM, JSM-6700F) and transmission electron microscopy (TEM, JEM-2010). Element distributions was identified by an aberration corrected scanning transmission electron microscope (STEM) (JEM-ARM200F, JEOL) equipped with X-ray energy dispersive spectroscopy (EDS) (X-max80, Oxford Instruments). The Brunauer-Emmett-Teller (BET) surface area was estimated by using the adsorption data (Tristar II 3020M, Mircomeritics, USA). Magnetic properties were characterized with the vibrating sample magnetometer (VSM) option of a Quantum Design physical property measurement system (PPMS) (Quantum Design, USA). X-ray photoelectron spectroscopy (XPS) analysis was performed using an ESCALAB 250 system (Thermo Scientific). The soft X-ray absorption spectra (XAS) were collected at the BL12B-a facility of the National Synchrotron Radiation Laboratory (NSRL, Hefei, P. R. China) using the synchrotron radiation from a storage ring running at 800 MeV with an average current of 300 mA. The polarization–electric field (P–E) loops were investigated with a Precision LC ferroelectric analyzer (Radiant Technology Product, USA) on the ceramic counterparts of the samples at room temperature. The corona poling method was applied on the Co2 sample. The voltage of the steel point electrode was 22 kV, and the 0.01 g Co2 powder was uniformly coated on a negative disk-like copper electrode with area of about 12 cm^2. The distance between too electrodes is 2 cm. Since the poled area at any one time was about 2 cm^2, the poling experiment is conducted 6 times on different parts of the disk-like copper

electrode coated with the Co2 sample, and the duration was 2 min.

5.2.3 Electrochemical testing

Investigation of the electrocatalytic oxygen evolution reaction (OER) was performed on an electrochemical workstation (CHI instruments 660E, China) in a standard three-electrode electrochemical cell, with saturated Ag/AgCl, platinum wire, and a glassy carbon electrode coated with the electrocatalyst as the reference electrode, the counter electrode, and the working electrode. To prepare the working electrode, 10 mg of electrocatalyst and 0.1 mL of 5 wt% Nafion® solution were dispersed in 0.75 mL deionized water and 0.25 mL methanol under ultrasound for 1 hour to form a mixed ink. 3 μL of this solution was drop-casted onto a glassy carbon electrode 3 mm in diameter (effective area 7.065 mm^2) and dried naturally, yielding a catalyst loading of 0.38 mg cm^{-2}. Linear sweeping voltammograms (LSV), CV curves and Tafel curves were obtained at a scan rate of 5 mV s^{-1}. Long term chronoamperometric measurements were conducted at 1.5 V vs reversible hydrogen electrode (RHE) with scan rate 10mV s^{-1}. In order to measure the Tafel plot, open potential (V_o) was measured at first. Then Tafel plots were obtained under Tafel mode and the range was set as V_o~V_o+100 mV with the scan rate 5 mV s^{-1}. Electrochemical impedance spectroscopy (EIS) was conducted with AC voltage with 5 mV amplitude at the potential of 1.686 V vs RHE within the frequency range from 10^6 Hz to 0.1 Hz. The potentials vs. Ag/AgCl were converted to RHE according to the Nernst Equation 5.1:

$$E_{\mathrm{RHE}} = E_{\mathrm{Ag/AgCl}} + E^{0}_{\mathrm{Ag/AgCl}} + 0.059 * \mathrm{pH} \qquad (5.1)$$

Where E_{RHE} is the converted potential vs. RHE, $E^{0}_{\mathrm{Ag/AgCl}}$ = 0.1976 V, and $E_{\mathrm{Ag/AgCl}}$ is the measured potential. Afterwards, the potentials are corrected to compensate for the effect of solution resistance, by subtracting *iR* (where *i* is the current, and *R* is the uncompensated ohmic electrolyte resistance).

5.3 Structure and morphology

Four samples were prepared by in-situ hydrothermal method according to the designed composition $Bi_4Ti_3O_{12}$·*n*($BiCoO_3$) (*n* = 1, 2, 3, 4), and denoted as Co1, Co2, Co3, and Co4, respectively. The morphologies are shown in **Figure 5.1**. It can be clearly observed from the SEM images that as-prepared samples are mainly composed of 10 nm thick nanoplates (with the average width varying from 1-2 μm), yet with tiny nanoparticles on the surface. And the quantity of nanoparticles on the surface increases from Co1 to Co4.

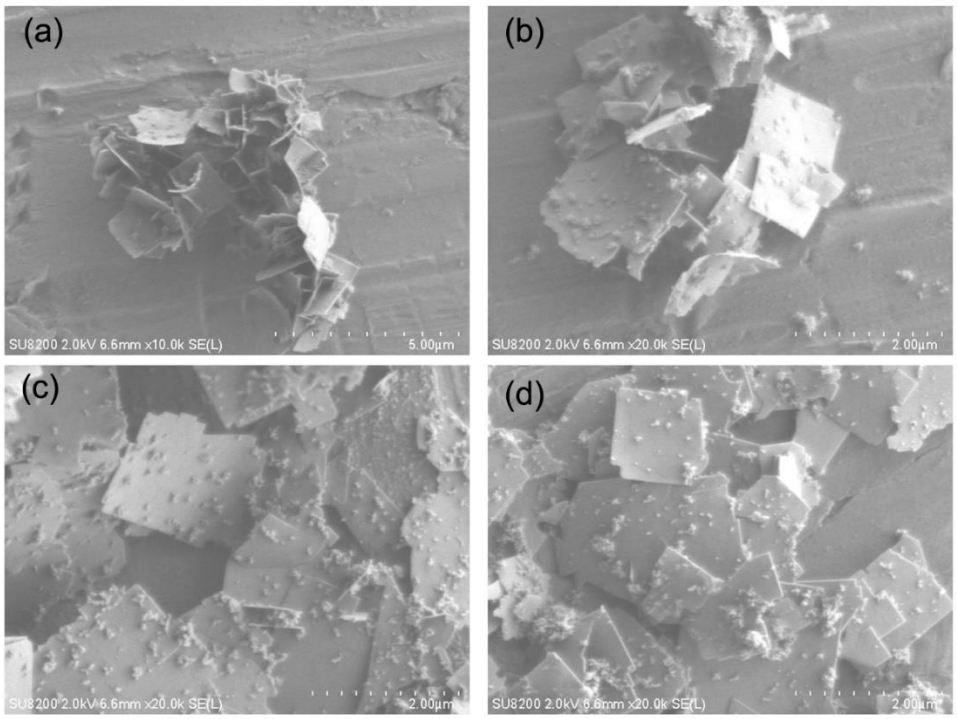

Figure 5.1 SEM images of as-prepared samples (a) Co1; (b) Co2; (c) Co3 and (d) Co4.

XRD patterns were collected to identify their compositions and are displayed in **Figure 5.2**. The refinements of the Co1 and Co2 samples were analyzed by the Pawley method based on the 4-layer perovskite BCTO crystal structure (Tetragonal, space group *F*2mm (42), JCPDS 38-1257). The resultant profile R-factor (R_p) values are far smaller than 10%, indicating that Co1 and Co2 samples are primarily $Bi_5CoTi_3O_{15}$ (BCTO). As shown in **Figure 5.3c**, this crystal structure is an alternation of four layers of perovskite-like oxide with one layer of fluorite-like bismuth oxide. In octahedral coordination with O, Co and Ti cations can occupy the A sites randomly in the perovskite-like sublattice.

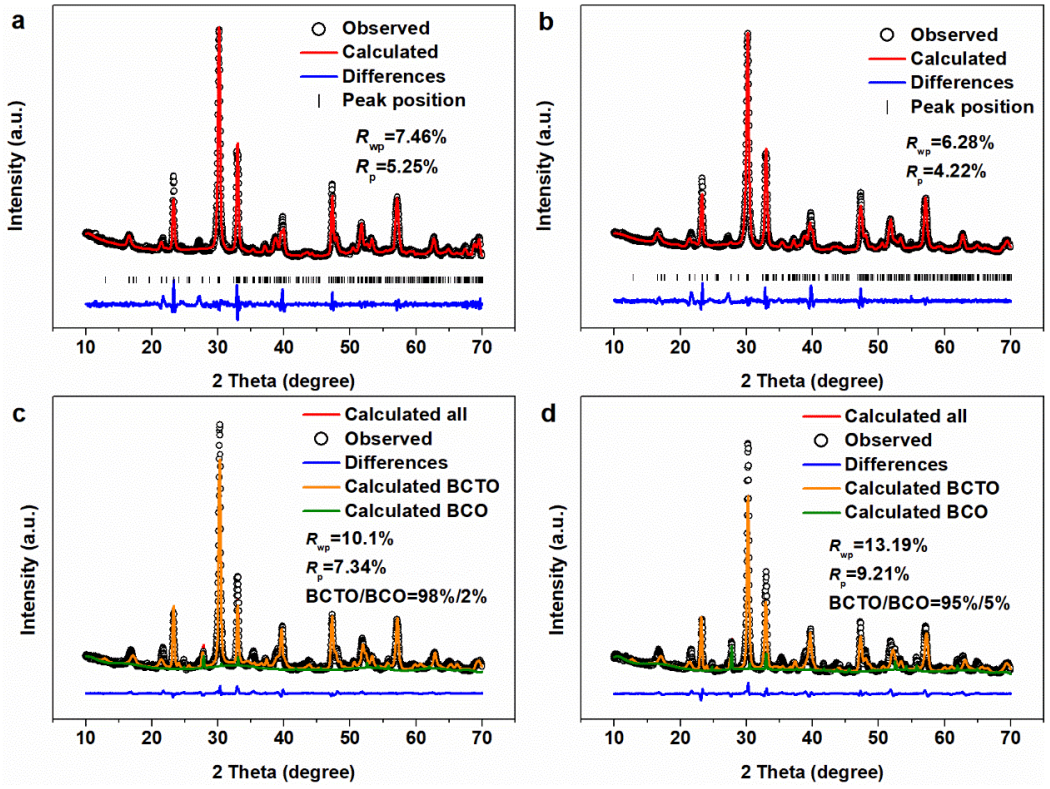

Figure 5.2 XRD patterns and refinements for as-prepared samples (a) Co1; (b) Co2; (c) Co3; and (d) Co4.

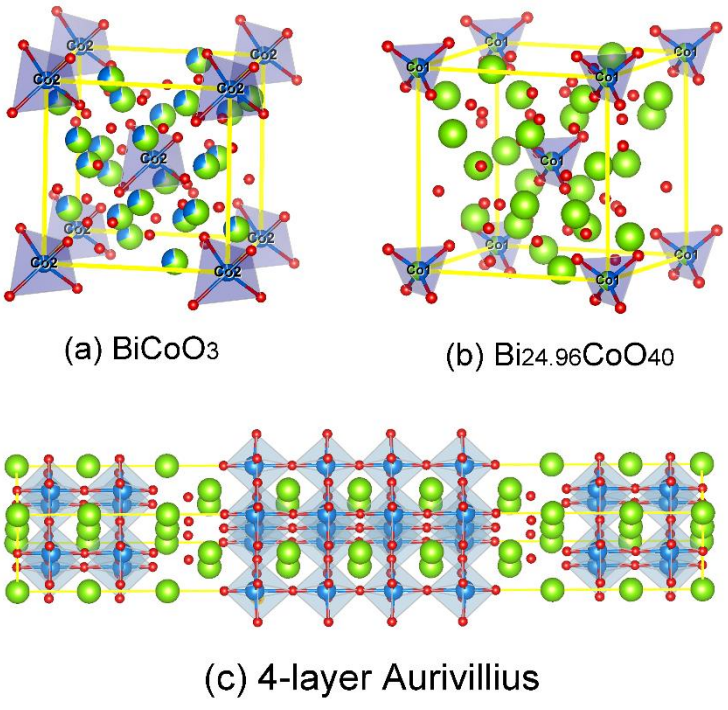

Figure 5.3 Crystal structures of $BiCoO_3$, $Bi_{24.96}CoO_{40}$, and $Bi_5CoTi_3O_{15}$. Red spheres present O, green spheres present Bi, and blue spheres present 3d transition metal Co (or Co/Ti in Aurivillius structure).

According to our previous work, collapse of perovskite-like sublattice will inevitably occur when too many perovskite-like cobalt oxide layers are inserted, resulting in a decreased number of layers and the

appearance of a secondary phase. Although the amount of the secondary phase in the Co1 and Co2 samples is too negligible to quantify by XRD refinement, we can discriminate the secondary phase by the appearance of a peak at 27.8°. This peak can be indexed to $BiCoO_3$ or some other isostructures such as Co-deficient $Bi_{24.96}CoO_{40}$ (in all $BiCoO_3$ isostructures, Co and Bi ions are tetrahedrally coordinated, and if there are more Bi ions, they will occupy the Co sites, or vice versa, as shown in the **Figure 5.3a, 5.3b**). So, the refinements of the Co3 and Co4 samples are analyzed by the Pawley method based on two phases: BCTO and the $BiCoO_3$ isostructure (BCO). From the refinement results, there are 2% BCO in the Co3 and 5% BCO in the Co4 sample. All lattice constants are listed in **Table 5.1**. Thus, we can draw the conclusion that when one or two $BiCoO_3$ layers are inserted into 3-layered perovskite $Bi_4Ti_3O_{12}$, the structure will turn out to be 4-layered perovskite $Bi_5Ti_3CoO_{15}$ (denoted as BCTO); but when three or four layers are inserted, 2% or 5% secondary phase BCO will appear.

Table 5.1 Cell constants of the main phase BCTO refined by Pawley method.

Sample	*a* (Å)	*b* (Å)	*c*(Å)
Co1	5.3830	5.3510	41.1100
Co2	5.4300	5.4120	41.5500
Co3	5.4310	5.4360	41.5600
Co4	5.4110	5.4260	41.2500

The typical TEM image in **Figure 5.4a** collected from the Co2 sample shows the morphology. **Figure 5.4b** is a high resolution TEM (HRTEM) image of a BCTO nanoplate recorded with the electron beam along the [001] zone axis. The spacings of the observed lattice are about 0.378 nm and 0.380 nm, which are consistent with the (110) crystalline planes of the orthorhombic 4-layer perovskite phase. The corresponding selected area electron diffraction (SAED) pattern in the inset of **Figure 5.4b** shows sharp diffraction spots, indicating that the BCTO nanoplates are single crystals with good crystallinity. **Figure 5.4c** contains a high-angle annular dark-field scanning transmission electron microscope (HAADF−STEM) image with EDS mapping applied to investigate the distribution of elements for the main phase and the secondary phase. Apparently, Bi, Ti, Co, and O are distributed homogenously throughout the BCTO nanoplates, but there are more Bi, Co, and O signal dots in the nanoparticles than in the nanoplates. The stronger signals from nanoparticles may associate with the fact that the secondary phase nanoparticles are Bi-Co enriched BCO, and the larger roughness of the tiny nanoparticles than

those in the nanoplates triggers an interfere of signals.

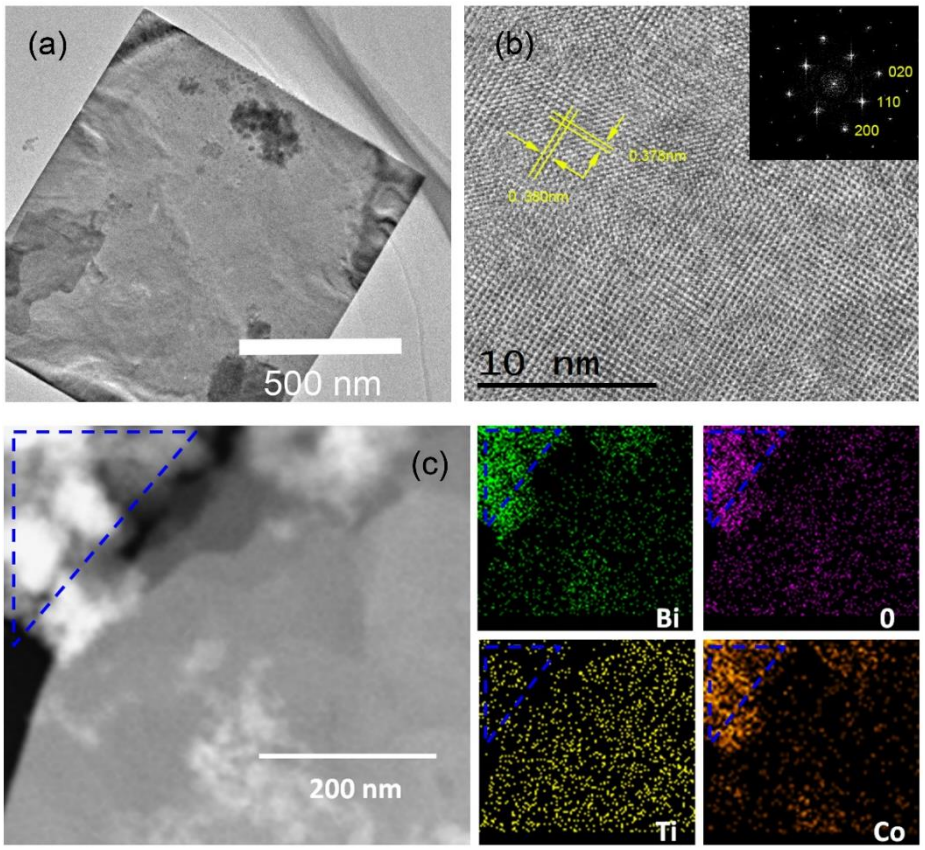

Figure 5.4 Morphology of Co2 sample (a) TEM image to show the typical morphology; (b) HRTEM image of the nanoplate in **Figure 5.4a** with the inset the corresponding SAED pattern; (c) STEM image and corresponding EDS element mapping images.

Above results mean that we have successfully prepared four samples composited by the in-situ grown secondary phase BCO nanoparticles and the 4-layer structured BCTO nanoplates. The BCO ratio increases gradually for composites Co1, Co2, Co3, to Co4, ranging in 0−5 wt% of the total mass of each sample. In order to better show the advantages of in-situ grown secondary phase for the following OER tests, we also synthesized the pure $Bi_4Ti_3O_{12}$ (BTO), $BiCoO_3$ isostructures (BCO) and $Bi_5CoTi_3O_{15}$ (BCTO) samples respectively. In addition, pure BCO and BCTO were physically mixed with the ratio of 2.5 wt%, and denoted as Phy Mix, for comparison purpose.

In a typical synthesis of the BCO, BCTO, Phy Mix, and BTO., $Ti(OC_4H_9)_4$ (> 99.7%), $Bi(NO_3)_3{\cdot}5H_2O$ (> 99%), $Co(NO_3)_2{\cdot}6H_2O$ (> 99%) were dissolved into 4 M HNO_3 solution according to the stoichiometric ratio of $Bi_4Ti_3O_{12}$, $BiCoO_3$, and $Bi_5CoTi_3O_{15}$, respectively. After 20 minutes of magnetic stirring, the homogeneous metal-ion solution was added into a 1.66 M NaOH solution (70 mL). The resulting slurry

was aged overnight and then washed with water and ethanol several times. Afterwards, it was dried at 60 °C for 8 hours and sintered at 650°C for 2 hours. According to the stoichiometric ratio, samples are denoted as BTO, BCO and BCTO. Phy Mix was prepared by physically mixing BCO and BCTO powders with the ratio of 2.5 wt% using an agate mortar. XRD and SEM see **Figure 5.5**, and **Figure 5.6** respectively.

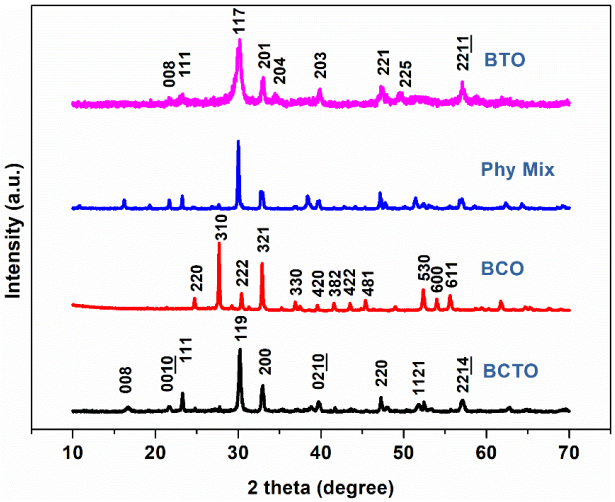

Figure 5.5 XRD patterns of pure BCTO, BCO, Phy Mix (physically mixed 2.5 wt% BCO and BCTO), and BTO samples.

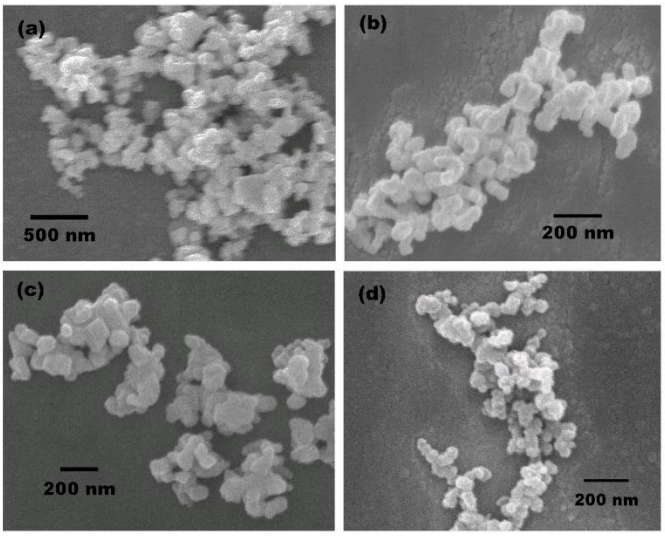

Figure 5.6 SEM images (a) pure BCTO; (b) pure BCO; (c) Phy Mix (physical mixed 2.5 wt% BCO and BCTO), and (d) pure BTO samples.

5.4 Electrocatalytic water splitting

The OER activities of the four in-situ grown samples (Co1, Co2, Co3, Co4) as well as Phy Mix sample, and reference BTO sample were characterized by linear-scan voltammetry (LSV) experiments in 1 M

NaOH electrolyte (**Figure 5.7a**). The current density at 1.7 V vs RHE is 20.34 mAcm^{-2}, 0.25 mA cm^{-2}, 0.025 mA cm^{-2} for Co2, Phy Mix, and BTO sample, respectively. Obviously, the performances of the in-situ grown samples are several orders higher than the physically mixed sample as well as the reference BTO sample. This can be explained by the following reasons. At first, in-situ grown secondary phase nanoparticles on the surface of nanoplates ensure a favorable heterojunction interface, which renders a fast electron transfer as well as a possible synergistic effect of the two phases. Moreover, the unique morphology, that is, decoration of the nanoparticles of BCO on the nanoplate of BCTO, guarantees abundant active sites (BET specific surface areas is 22.2 m^2 g^{-1}, 25.53 m^2 g^{-1}, 22.79 m^2 g^{-1}, and 17.56 m^2 g^{-1} for Co1, Co2, Co3, and Co4 respectively), which is another reason for the incredible enhancements of in-situ samples compared to ex-situ samples.

It is worth noting that the Co2 and Co3 sample exhibit s largest current density (j) when normalized by BET surface areas to exclude the surface area contribution (inset of **Figure 5.7a**), which will be discussed in detail with more characterizations as follows. The potential at current density j=10 mA cm^{-2} ($\eta_{j=10}$) is an important parameter characterizing the efficiency of a cell. The corresponding overpotentials (against 1.23 V vs. RHE) of the in-situ grown samples are plotted in **Figure 5.7b**, which decreased from 420 mV to 387 mV, and then raised up to 452 mV. Since a lower overpotential means less energy consumed to split the water, the Co2 sample with the lowest overpotential (387 mV at j=10 mA cm^{-2}) is the highest-performing OER electrocatalyst of all. The Tafel plots in Fig.3c and the Tafel slope values in **Figure 5.7d** further confirm that the Co2 sample possesses the smallest Tafel slope of 44 mV dec^{-1}. Such small Tafel slopes ($\leq$ 52 mV dec^{-1}) indicates that the rate determining step tends to change from -OH adsorption to -OOH formation [60], according to the possible OER process (**Equation 5.2-5.5**).

$$\mathrm{Catalyst} + 2\mathrm{OH}^- = \mathrm{Catalyst} - \mathrm{O} + \mathrm{H_2O} + 2e^- \quad (5.2)$$

$$\mathrm{Catalyst} - \mathrm{O} + \mathrm{OH}^- = \mathrm{Catalyst} - \mathrm{OOH} + e^- \quad (5.3)$$

$$\mathrm{Catalyst} - \mathrm{OOH} + \mathrm{OH}^- = \mathrm{Catalyst} - \mathrm{OO} + \mathrm{H_2O} + e^- \quad (5.4)$$

$$\mathrm{Catalyst} - \mathrm{OO} + \mathrm{OH}^- = \mathrm{Catalyst} - \mathrm{OH} + \mathrm{O_2} + e^- \quad (5.5)$$

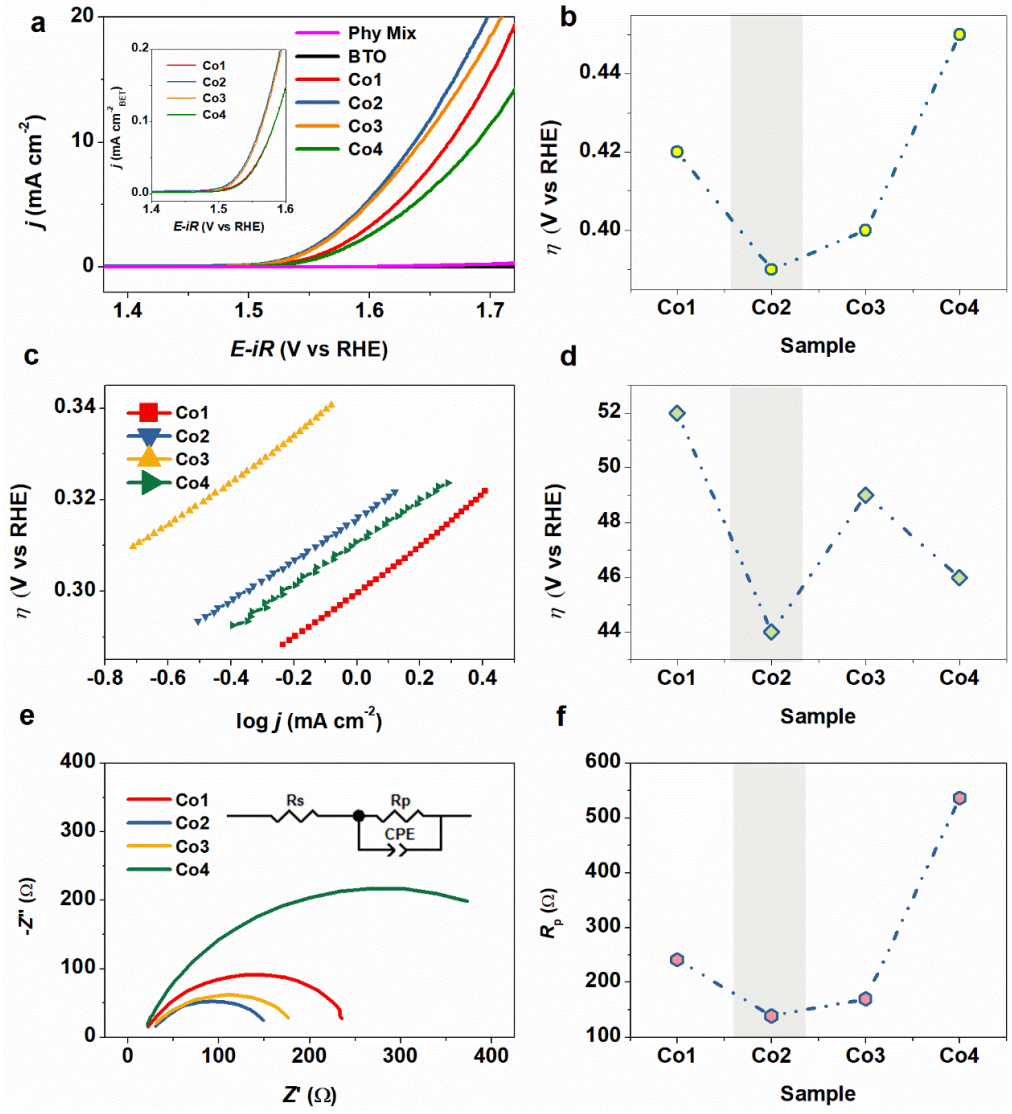

Figure 5.7 Electrocatalytic characterization for the OER (a) LSV curves at the scan rate of 5 mV/s, inset is the LSV curves normalized by BET surface area; (b) overpotentials of the four samples at the current density of 10 mA cm-2 ($\eta_{j=10}$); (c) Tafel plots; (d) Tafel slopes of the four samples; (e) Nyquist plots, with the inset showing the equivalent circuit; and (f) polarization resistance (R_p) of the four samples.

The measured electrochemical impedance spectra (EIS) provide more information about the electrochemical process. An equivalent circuit composed of R_s, R_p, and CPE is proposed to interpret the Nyquist plots in **Figure 5.7e**, where R_s represents the solution resistance, R_p represents the polarization resistance, and CPE is the constant phase element (for the equivalent circuit see the inset of **Figure 5.7e**). The Co2 sample has the smallest polarization resistance and the R_p values of the four samples are shown in **Figure 5.7f**, which is in line with the results from LSV. In addition, the electrochemical active surface area (ECSA) is generally proportional to double layer capacitance C_{dl}, which can be calculated based on

the Nyquist plots parameters and the equation:

$$C_{\mathrm{dl}} = (\frac{T}{Rs^{P-1}})^{\frac{1}{P}}/S \qquad (5.6)$$

T, P, R_s are the parameters resolved from Nyquist plots, and details provided in **Table 5.2**. The calculated C_{dl} is about 82 μF cm^{-2}, 158 μF cm^{-2}, 107 μF cm^{-2}, and 124 μF cm^{-2} for the Co1, Co2, Co3, and Co4 samples, respectively. Although these four sample have similar morphology and BET specific surface areas (22.2 m^2 g^{-1}, 25.53 m^2 g^{-1}, 22.79 m^2 g^{-1}, and 17.56 m^2 g^{-1} for Co1, Co2, Co3, and Co4 respectively), the Co2 sample possesses a larger ECSA (C_{dl}) than the other three samples.

Table 5.2 Parameters by analyze Nyquist plots to calculate the capacity Cdl.

Sample	Rs (Ω)	(CPE) T	(CPE) P	C_{dl} (μF cm^{-2})
Co1	17.43	3.0E-5	0.82	82
Co2	24.36	4.7E-5	0.82	158
Co3	22.6	4.0E-5	0.81	107
Co4	17.07	3.0E-5	0.86	124
Poled Co1	23.55	3.7E-5	0.79	79
Poled Co2	28.56	3.0E-5	0.87	143
Poled Co3	38.32	3.7E-5	0.81	106

5.5 Electronic structure analysis

The O 1*s* spectra (**Figure 5.8**) were measured first, and they exhibit two peaks with the binding energy (BE) at about 529.6 eV and 531.4 eV. The main peak located at 529.6 eV can be assigned to the lattice oxygen, and the latter shoulder one can be assigned to the less electron-rich oxygen species, such as surface chemisorbed oxygen species on the surface of BCO and BCTO [121]. Due to the complexity of the oxygen containing species, we do not ascribe the shoulder peak to distinct species (e.g., O^-, surface OH groups, contamination CO_2 etc). The peak area ratio of surface/lattice oxygen was defined as R_{so}, and it is about 50%, 59%, 56% and 55% for the Co1 to Co4 samples. The relatively high percentage of surface adsorbed oxygen species indicates that all the samples should have strong chemisorbing capacity.

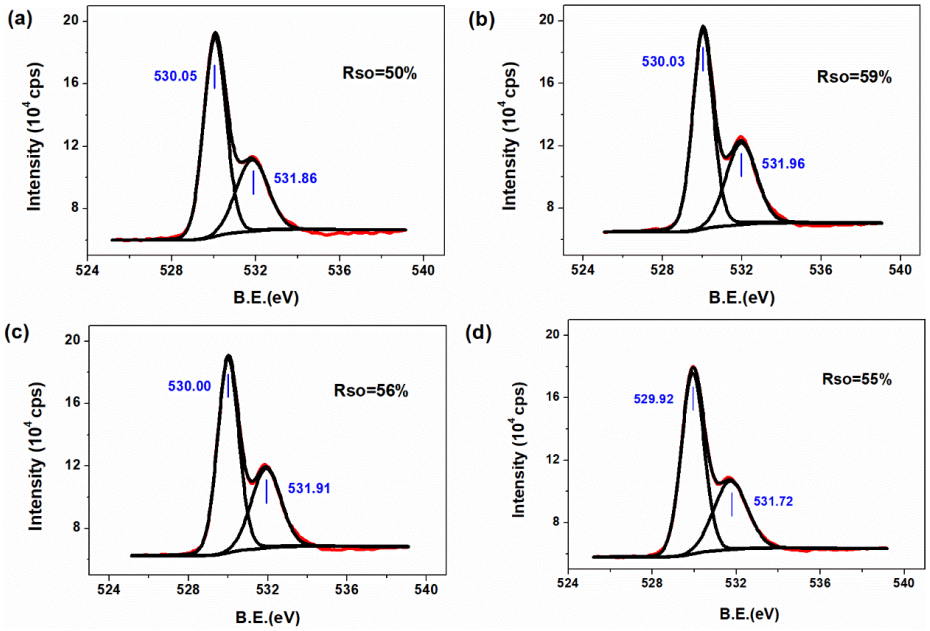

Figure 5.8 XPS spectra of O 2p peak (a) Co1; (b) Co2; (c) Co3 and (d) Co4.

In addition, the Co2 sample exhibited the best adsorption capacity, which is likely to have originated from its superior surface electronic structure, which will be discussed later. To provide further information, the temperature dependence of the magnetization (*M*−*T*) under magnetic field of 500 Oe was measured. There are two broadened peaks located at 10 K and 42 K in **Figure 5.9a**, which are caused by weak antimagnetic interactions of Co−O−Co. The Curie−Weiss law (**Equation 5.7**) was applied to fit the curves, as shown in **Figure 5.9b**. All the as-prepared samples have a positive linear correlation, suggesting Curie−Weiss paramagnetism. According to **Equations 7 and 8**, the effective magnetic moment, μ_{eff} and average e_g electron number can be estimated based on the quenching of orbital angular momentum (L = 0) and a measured g factor.

$$\frac{1}{\chi} = \frac{1}{C}T + \frac{T_C}{C} \qquad (5.7)$$

Where χ, C, T, and T_C represent the magnetic susceptibility, Curie−Weiss constant (C > 0), temperature, and Curie point, respectively.

$$\mu_{\text{eff}} = \sqrt{\frac{3kC}{N}} \qquad (5.8)$$

Where μ_{eff} is the effective magnetic moment, k is Boltzmann constant, C is the Curie−Weiss constant, and N is the number of magnetic ions in the unit cell (N = 1, since there is only one Co atom in the BCTO or BCO).

$$\mu_{\text{eff}} = g\sqrt{J(J+1)}\mu_B \qquad (5.9)$$

Where g is the Lande factor, J is total quantum number, and μ_B is the Bohr magneton. (g can be approximated by 4.2 in $Bi_6Fe_2Ti_3O_{18}$ and $Bi_6FeCrTi_3O_{18}$[122].)

Table 5.3 Estimated Curie-Weiss constant C, effective magnetic moment μ_{eff} and e_g electron number.

Sample	C (10^{-4} K μ_B Oe^{-1} f.u.$^{-1}$)	μ_{eff} (μ_B)	e_g electron
Co1	5.32	4.65	1
Co2	8.40	5.85	1.2
Co3	10.02	6.32	1.3
Co4	19.38	8.73	1.5

Figure 5.9c demonstrates the increasing trends in Curie-Weiss constant, effective magnetic moment, and average e_g electron number from the Co1 to the Co4 samples (For the numerical values, **Table 5.3**). In theory, to reveal the evolution of the electronic structure, the secondary phase BCO and the main phase BCTO should be separated when measuring, which was very difficult to realize in our case, however. Nevertheless, the ratio of BCO to BCTO is relatively very small (0−5 wt %), and the only difference between the four samples is none other than the ratio of BCO to BCTO. Thus, it is reasonable to identify the contribution of the secondary phase BCO by carefully comparing the subtle change in the entire BCO/BCTO sample. Here, the increase in the calculated average e_g electron number from Co1 to Co4 sample is due to the increased of amount of BCO. In BCO, the Co ions are octahedrally coordinated with threefold degenerate high energy t_{2g} orbitals and low energy doubly degenerate e_g orbitals. In BCTO, the Co ions are tetrahedrally coordinated with doubly degenerate high energy e_g orbitals and threefold degenerate low energy t_{2g} orbitals. Therefore, the calculated e_g number actually means the average electron number in high energy orbitals (HE), that is, e_g from main phase BCTO and t_{2g} from 0−5 wt % BCO.

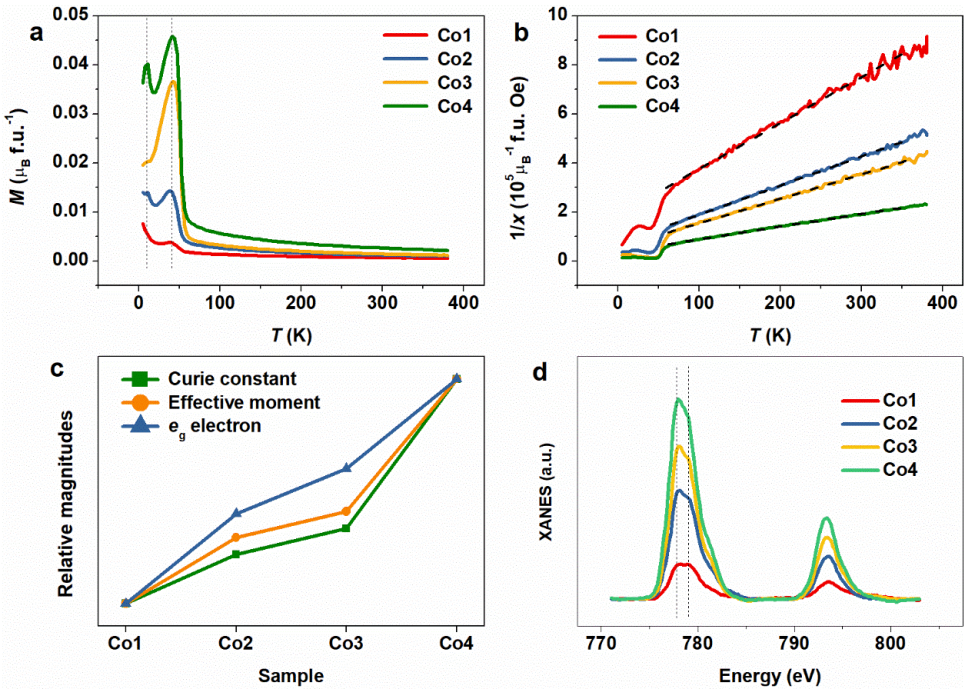

Figure 5.9 Electronic structure analysis. a Temperature dependence of the magnetization (M−T) under a magnetic field of 500 Oe; b Temperature dependence of the inverse susceptibility $1/\chi$; c evolution of the estimated Curie−Weiss constant C, effective magnetic moment, μ_{eff} and the e_g electron number; d normalized Co L−edge XAS spectra for the four samples.

XAS is an effective technique to investigate the specific electronic occupation. As shown in **Figure 5.9d**, the Co $L_{2,3}$ edge spectra are almost with the same for each of the four samples, which means that all the Co is in the same valence state. The two absorption peaks located at 778 eV and 779 eV are due to the spin-orbit splitting of the Co 2p state. Even though most octahedrally-coordinated transition metal ions are suggested to be in the low spin state (LS) due to the strong crystal field, the octahedrally-coordinated Co^{3+} ions (O_{Co}) in the BCTO nanoplates have a strong probability of being found in the intermediate spin (IS) state $(t_{2g})^5(e_g)^1$, since they would make no contribution to the absorption peak at 778 eV if they were in the LS state $(t_{2g})^6(e_g)^0$. In the tetrahedral coordination of the secondary phase BCO, Co^{3+} ions (T_{Co}) may be in the high spin (HS) state $(e_g)^3(t_{2g})^3$ on account of the low crystal field of the tetrahedron. Then, the absorption peak at 778 eV is contributed by the $2p$−e_g transition of HS T_{Co}. Meanwhile, the absorption peak of 779 eV is contributed by the $2p$−e_g transition of IS O_{Co} together with the $2p$−t_{2g} transition of HS T_{Co}. In this situation, the relative intensity of the peak at 778 eV will be increased if the ratio of BCO to BCTO is increased, just as the results of XAS measurements suggest. Importantly, this analysis is also in agreement with the continuing increase of the effective magnetic moment μ_{eff} and the e_g electron number

based on the *M*−*T* curves.

5.6 Influence of ferroelectric polarization

Figure 5.10a presents the polarization−field (*P*−*E*) loops at room temperature. However, the measured *P*−*E* loops are unable to reach saturation and they are not closed, all due to a certain degree of current leakage. In fact, leakage problem is very common for smaller band gap ferroelectric materials (especially the Bi-Co-contained oxides). Despite of the leakage, the intrinsic ferroelectric polarization of layered perovskite material family have been well recognized [123]. The saturation polarization ($2P_s$) is 24.5 μC cm^{-2} for the Co2 sample at the applied field of 80 kV cm^{-1}. The remnant polarization ($2P_r$) extracted from the *P*−*E* loops in **Figure 5.10a** increases from 7.12 μC cm^{-2} to 11.59 μC cm^{-2} and then decreases to 9.11 μC cm^{-2}.

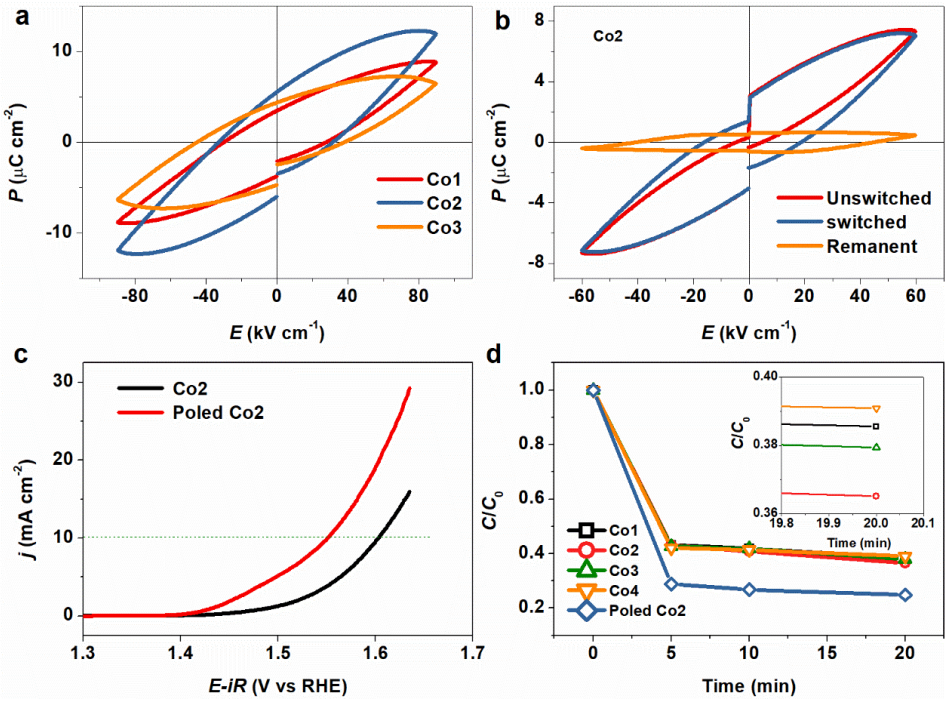

Figure 5.10 Effects of ferroelectric polarization (a) P-E loops at the maximum electric field of 90 kV cm-1 at room temperature; (b) remnant P-E loop of Co2 at the maximum electric field of 60 kV cm-1 at room temperature; (c) LSV curves of Co2 after corona-poling; (d) adsorption curves of RhB dye for the four samples as well as the poled Co2 sample, with the inset the enlarged residual concentration at the adsorption equilibrium after 20 min.

Figure 5.10b is the remnant *P*−*E* loop of the Co2 sample. Compared with the standard *P*−*E* measurement, remnant *P*−*E* loops will be more reliable and provide more information about the reverse voltage, reverse

speed, and useful non-residual polarization. The red curve represents the unswitched polarization part, the blue curve the switched part, and the yellow one the remnant part (the difference between the switched and unswitched polarizations). The closed feature of the remnant loop suggests the benign ferroelectric properties of the Co2 sample.

As the layered perovskite nanoplates are single crystalline and ferroelectric, they will easily exhibit a single domain structure aligned along the poling electric field direction. The corona polar method was applied to form the one-directional dipolar alignment inside. **Figure 5.10c** presents the LSV curves measured on the Co2 sample before poling and after poling, respectively. Remarkably, the overpotential at 10 mA cm^{-2} is reduced from 387 mV to 320 mV after poling. The superimposed improvements by poling can be explained as follows. At first, the poled crystals should attract more electrically charged species from the ambient environment on their surfaces to screen the enhanced internal built-in electric field for the sake of charge neutrality. Therefore, larger remnant polarization may result in better adsorption capability. To test this inference, the adsorption capacity of the four samples was measured with the organic dye rhodamine B (RhB) as the adsorbate target. As displayed in **Figure 5.10d**, all the as-prepared ferroelectric samples can adsorb about 60% of the RhB molecules in 10 mg L^{-1} RhB solution, although the Co2 sample shows superior adsorption over the other three (inset of **Figure 5.10d**) and the adsorption is 20% further enhanced after poling. In addition, the energy band of the poled single crystals will inevitably be bent by the magnitude of 0.3−0.5 V, as estimated in $BaTiO_3$ at room temperature [112]. The OER process might be accelerated at the same applied voltage with favorable energy band bending.

To verify the above assumption, samples were also corona poled and their LSV curves and Tafel plots were shown in **Figure 5.11a** and **Figure 5.11b** respectively. Based on the LSV curves in **Figure 5.11a**, the overpotential at the current density j=10 mA cm^{-2} ($\eta_{j=10}$) is about 390 mV, 320 mV, and 360 mV for Co1, Co2 and Co3 respectively. Apparently, poled Co2 and poled Co3 have exceeded the state-of-art commercial IrO_2 which is with 380 mV $\eta_{j=10}$. And corona poling treatment reduced the $\eta_{j=10}$ values to 30 mV, 70 mV, and 40 mV for the Co1, Co2 and Co3 respectively. Moreover, Tafel slope is decreased to be 59 mV dec^{-1}, 34 mV dec^{-1}, and 40 mV dec^{-1} for the three poled samples respectively (**Figure 5.11b**). ECSA are calculated in the same method as mention above and the details are provided in **Table 5.2**, from which we can see that ECSA do not change after corona poling treatment. LSV curves normalized by BET surface area and ECSA is consistent with the ferroelectric polarization results, indicating that the differences in the OER performance between the three poled samples are mainly originated from the

intrinsic polarization intensity.

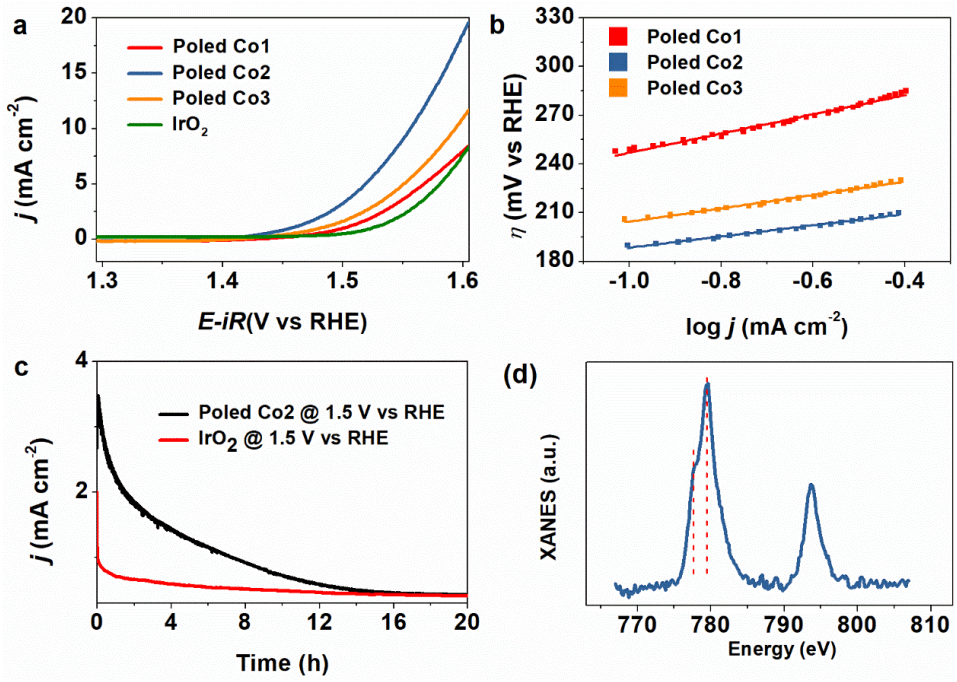

Figure 5.11 Electrocatalytic characterization for the corona poled samples (a) LSV curves at the scan rate of 5 mV s-1; (b) Tafel plots of; (c) Long term chronoamperometric measurement of poled Co2 and IrO2; (d) XAS spectra of poled Co2 sample before chronoamperometric measurement.

As shown in **Figure 5.12**, 20 cycles of cyclic voltammetry (CV) were conducted on the poled Co2 sample, and there is no obvious redox peak during the forwards and backwards sweep, suggesting a very stable phase and structure. However, the performance of 20th cycle is relatively worse than the 1st cycle. A long term chronoamperometric measurement was also conducted on the poled Co2 sample at the potential of 1.5 V vs RHE with the duration of 20 hours (**Figure 5.11c**). The measured corresponding current density decreased gradually in the first 14 hours and stabilized afterwards. After carefully analysis, we found that the initial current density (3.5 mA cm^{-2}) is almost the same as that from the LSV curve for poled Co2 sample in the **Figure 5.11a** (3.4 mA cm^{-2} at 1.5 V vs RHE). But 14 hours later, the current density is decreased to 0.45 mA cm^{-2} (8-fold decreased).

To find the underlying mechanism, TEM and HRTEM images of poled Co2 sample before and after the 20 hours chronoamperometric measurement were conducted (**Figure 5.13**). TEM images demonstrate that poled Co2 sample still keeps its original morphology during the 20 hours test. HRTEM images confirm its regular lattice fringe and crystalline surface morphology and SAED patterns verify there is no amorphization or phase transformation to other compositions, such as CoOOH et al. All these results

suggest that there is no morphology or phase structure change during either the corona poling or the long term OER test.

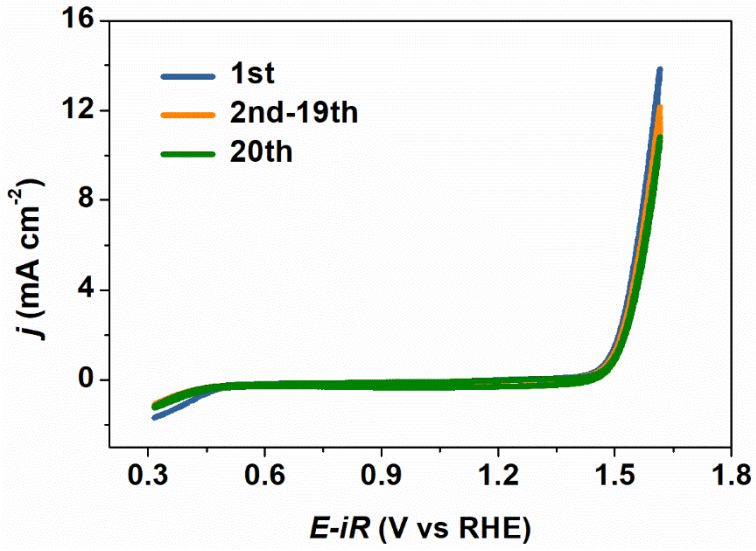

Figure 5.12 20 cycles of cyclic voltammetry (CV) on the poled Co2 sample.

Then XAS spectrum of corona poling treated poled Co2 sample after the chronoamperometric measurement was measured and presented in the **Figure 5.11d** to gain in-depth surface electronic information. It is obviously that peak intensity at 789 eV is much higher than that of 778 eV in poled Co2 sample before the long term chronoamperometric measurement, a sharp contrast to the curves in **Figure 5.9d**. According to above analysis, it means that the concentration of IS Co increased when poling Co2 sample. This change could be owed to a possible surface electronic structure modification during the corona poling process before long term test. The discharged air plasma in corona poling process may ensue tangling bond, defects generation, charge injection and other modification of surface, accompanied with the ferroelectric poling. After the 14 hours long time chronoamperometric measurement, this kind of transient surface electronic structure modification might be decreased. However, the poled Co2 sample still performed better than unpoled Co2 sample and IrO_2 with the assistance of the permanent ferroelectric polarization inside in this situation (0.45 mA cm^{-2} of poled Co2, 0.17 mA cm^{-2} of poled Co2 and 0.32 mA cm^{-2} of IrO_2). It means that the performance improvement contributed by the surface electronic modification may be dwindled gradually within 14 hours but the effects contributed by the ferroelectric polarization works all the time.

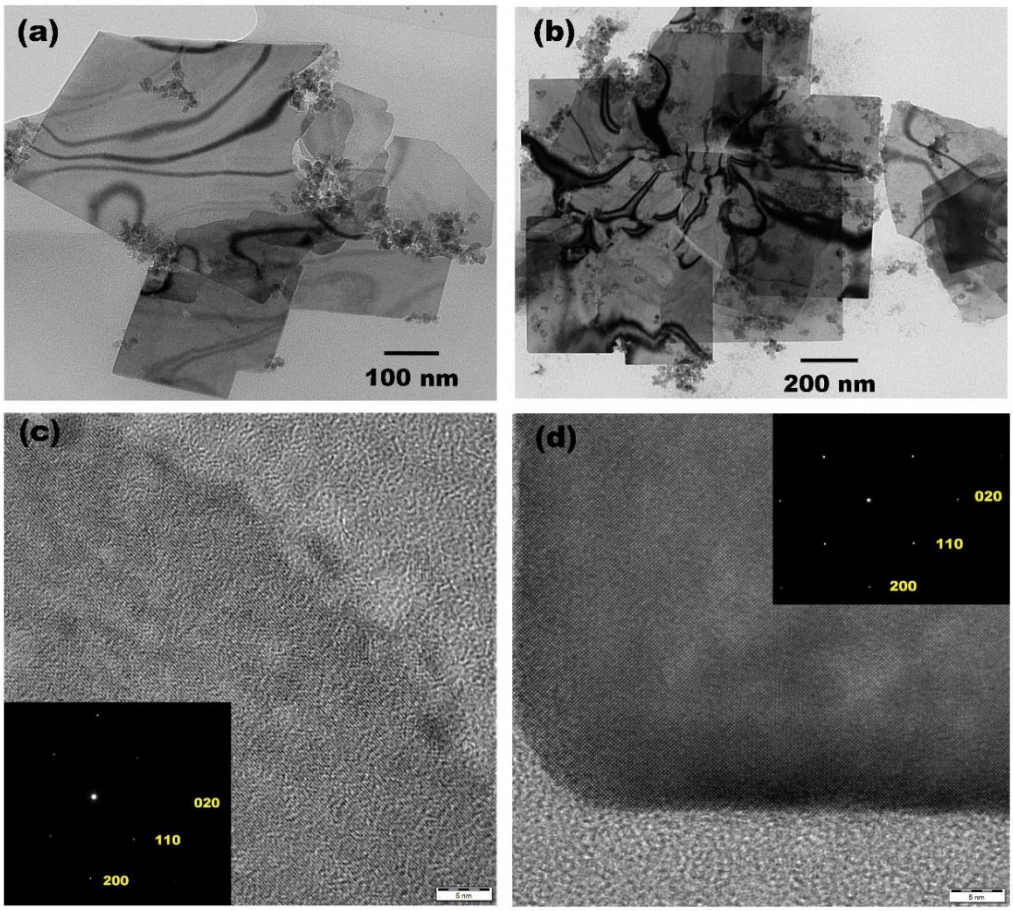

Figure 5.13 Morphology before and after 20 hours chronoamperometric measurement (a) TEM image of poled Co2 sample before chronoamperometric measurement; (b) TEM image of poled Co2 sample after chronoamperometric measurement; (c) HRTEM image and corresponding SAED of the main phase BCTO of the poled Co2 sample before chronoamperometric measurement; (d) HRTEM image and corresponding SAED of the main phase BCTO of the poled Co2 sample after chronoamperometric measurement.

5.7 Discussion

The high intrinsic OER efficiency and similarity of the LSV curves normalized by BET surface area for Co2 and Co3 can be contributed to the compromises of ferroelectric polarization and spin states. Co2 sample is with better ferroelectricity but the effective magnetic moment μ_{eff} (average e_g electron number) of Co3 sample is higher. But after poling these two samples, Co2 performed better than Co3 as the contribution of the ferroelectric polarization is predominant in this situation. **Figure 5.14** gives a clear point of this work: by inserting several magnetic layers of BCO into ferroelectric layered perovskite, 0−5

wt % BCO decorated 4-layered perovskite BCTO nanoplates were formed. The Co^{3+} in the BCO is in the tetrahedrally coordinated $(e_g)^3(t_{2g})^3$ HS state, which increases the e_g electron number (or high energy orbital electrons). Meanwhile, BCTO ultrathin nanoplates provide a large surface area and Co^{3+} in the IS spin state with the $(t_{2g})^5(e_g)^1$ configuration, as well as desirable remnant polarization. During the OER process, it is electrons located in unfulfilled high energy orbitals of 3*d* transition metal ion on the surface that participate in σ-bonding with the adsorbates. Neither too weak nor too strong bonding is favorable for absorption and desorption at the same time. Due to its intrinsic ferroelectric property, BCTO nanoplates may present an approximate single domain structure with strong polarity when applying the corona poling. This provides additional driving forces towards charge transport on the electrode due to band bending and attracts more charged interactants such as OH^- near the surface in the electrocatalytic OER process. At the same time, corona poling might also bring about favorable surface modification, which further improve the OER efficiency of the electrocatalysts. In this way, the rate determining step tends to change from -OH adsorption to -OOH formation, resulting in a dramatically low Tafel slope and greatly enhanced OER efficiency.

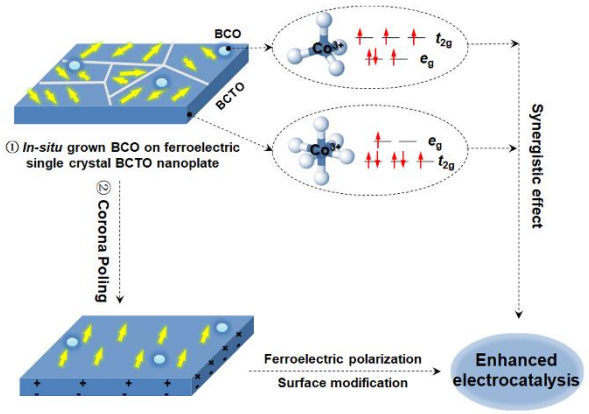

Figure 5.14 Illustration to demonstrate the advantages of the in-situ as-prepared BCO/BCTO nanostructures for electrocatalysis.

5.8 Conclusions

Here, we reported a strategy to improve the OER activity: in-situ grown a secondary phase on a ferroelectric matrix and corona poling it afterwards. At first, layered perovskite BCTO nanoplates with in-situ grown BCO nanoparticles were successfully prepared by a one-step hydrothermal method. According to the XRD and SEM results, the BCTO nanoplates are 10 nm in thickness, and the BCO

nanoparticles are in the ratio of 0−5 wt%. HRTEM and EDS mapping confirm the single crystallinity of the BCTO nanoplates and the composition of the BCO nanoparticles. All four samples exhibit excellent electrocatalytic OER activity, low overpotential, low Tafel slopes, and low polarization resistance. Nevertheless, the efficiency is increased from the Co1 to the Co2 sample, then decreased on the Co3 and Co4 samples, although they have a similar BET surface area (about 20 m^2 g^{-1}). Based on the *M*−*T* and XAS results, the estimated Curie−Weiss constant *C*, effective magnetic moment μ_{eff}, and average e_g electron number are increased from the Co1 to the Co4 sample. The maximum OER activity was realized on the Co2 sample with its appropriate electronic configuration. What is more interesting, the OER property can be further improved by the corona poling method, resulting in the low overpotential of 320 mV at the current density of 10 mA cm^{-2} and a Tafel slope of 34 mV dec^{-1}. The phase and morphology are very stable after treated by corona poling and the long term OER tests. The improvement contributed by the surface modification may decreased gradually within 14 hours but the effects of ferroelectric polarization works all the time. This work may provide an additional instructive strategy to enhance the OER performance for future energy conversion and storage devices.

Chapter 6

6 High oxygen evolution activity of tungsten bronze oxides boosted by anchoring of Co^{2+} at Nb^{5+} sites accompanied by substantial oxygen vacancy

6.1 Introduction

The efficiencies of many green energy technologies are generally restricted by the sluggish kinetics of the oxygen evolution reaction (OER) [83,124,125]. The underlying mechanisms are gradually being revealed, but they are not fully explicated as yet. For the traditional adsorbate evolution mechanism (AEM) [23,27], the rate-determining step is the O–O bond formation through nucleophilic attack of *O by water or OH^- occurring on single metal active sites (Eley–Rideal, ER-type mechanism) [28,3].This step can be avoided by the direct formation of the O–O bond between the neighboring oxygen species on two adjacent active sites (Langmuir–Hinshelwood, LH-type mechanism) [29]. In principle, the LH-type mechanism with two conjunct active sites is more desirable, but it requires the distance between two active sites to be short enough [30]. Activating the LH-type mechanism remains a challenge if only metal cations are OER-active, as two metal cations are spatially separated by the oxygen anion in oxide catalysts, while the pure transition metals with short metal atom distances are usually unstable as anode.

Recently, O-O formation via direct coupling between a metal cation and a lattice oxygen anion, known as lattice oxygen mechanism (LOM), has been proposed both theoretically and experimentally [31-33]. In this mechanism, both metal cations and lattice oxygen anions are active sites, cooperating with each other due to the short distance between them. The underlying physics of the LOM is that the electrons involved are contributed by the metal 3*d* orbitals as well as the O 2*p* orbitals when Fermi level enters into the O 2*p* band [13]. Exploring new-type LOM-active electrocatalysts or turning traditional AEM electrocatalysts into LOM ones by regulation, are two common strategies [126-128]. For instance, $CaCoO_3$ is a new LOM high-efficiency OER electrocatalyst with a significantly small lattice parameter due to the high valence state of Co [4]. Unfortunately, this kind of rigid structure is rather rare under ambient conditions, since they require rigorous synthesis conditions such as high temperature and ultrahigh pressure. To turn AEM to LOM in ABO_3 perovskites, one of the indirect methods applied is A-site doping to increase the valence state on the B-site metal active sites, for example, by doping Sr into La sites in the perovskite $LaCoO_{3-\delta}$

[11]. This strategy is usually limited, however, by the crystal lattice tolerance and poor stability issues when the O *p*-band center is too close to the Fermi level [79].

Compared to the rutile, perovskite, spinel, or pyrochlore structures that are usually adopted by transition metal oxides, the tetragonal tungsten bronze (TTB) structure, represented among a large family of solid solutions with enormous structural flexibility, has not been reported as an OER-active matrix, although it has been extensively studied in the realms of electro-optic, piezoelectric, pyroelectric, millimeter wave, and photorefractive applications [129,130]. With the typical formula of $(A_1)_4(A_2)_2C_4B_{10}O_{30}$, the A_1 cations are in the 15-fold-coordinated sites, the A_2 cations are in the 12-fold-coordinated sites, the B cations are in two different 6-fold-coordinated sites, and the C cations are in the 9-fold-coordinated sites [131]. Typically, A_1, A_2, and C sites can be empty or filled by alkali and alkaline-earth metal ions, which make the structure relatively flexible and stable. In addition, B sites are octahedrally coordinated, and they are reserved for high valence state cations such as Nb^{5+} or Ta^{5+}. What is more interesting, the connections of the NbO_6 octahedra are versatile in the TTB structure with the Nb-O-Nb distance ranging from 3.71 to 3.94 Å, in contrast to the rigid perovskite structure, for example, $LaCoO_3$ (Co-O-Co 3.82 Å) and $SrCoO_3$ (Co-O-Co 3.86 Å). Thus, we consider that the flexible TTB structure could be an excellent matrix, capable of fast OER mechanisms, if it can accommodate enough OER-active sites.

In this work, we attempted to anchor Co on Nb^{5+} sites in $Sr_{0.5}Ba_{0.5}Nb_2O_6$ (SBN), to explore the possible OER activity and mechanisms in the TTB structure. The similarity in the ion radii of Co and Nb ensures the success of substitution, while the difference in valence could introduce a huge amount of oxygen defects (Co^{2+} (LS, 0.79 Å) vs. Nb^{5+} (0.78 Å)), with the great potential of activating faster mechanisms with the involvement of oxygen defects. $Sr_{0.5}Ba_{0.5}Nb_{2-x}Co_xO_{6-\delta}$ (x = 0, 0.3, 0.45, 0.6, denoted as SBN, SBNC30, SBNC45, and SBNC60, respectively) with different amounts of Co was prepared to optimize the proportion of substitution. The crystal structure results suggest that the TTB structure can be well maintained in the SBN, SBNC30, and SBNC45, but the perovskite secondary phase would emerge in the SBNC60. Electronic study suggests that the occupation of Co in the Nb^{5+} sites of TTB structure brings about massive oxygen vacancy (O_{vac}) and stabilizes itself in the form of Co^{2+}. The presence of oxygen vacancies (O_{vac}) leads to a spin state transition of Co^{2+} from high spin (HS) to low spin (LS) due to the further crystal field splitting. The coexistence of O_{vac} and LS Co^{2+} triggers an oxygen intercalation mechanism, endowing SBNC45 with superior OER performance to commercial IrO_2 under alkaline working conditions.

6.2 Experimental

6.2.1 Synthesis

All the samples in the present work were prepared by conventional solid-state reaction (SSR). Nb_2O_5 (99.99%), $Ba(NO_3)_2$ (≥ 99%), $Sr(NO_3)_2$ (≥ 99%), $Co(NO_3)_2{\cdot}6H_2O$ (≥ 98%), KNO_3 (≥ 99%), $LiNO_3$ (99.99%), and Fe_2O_3 (99.995%) were purchased form Aldrich Ltd. and used as starting materials. For the preparation of the SBN, SBNC30. SBNC45, and SBNC60 samples, the corresponding chemicals were mixed homogenously in stoichiometric ratios according to the formula $Sr_{0.5}Ba_{0.5}Nb_{2-x}Co_xO_{6-\delta}$ (x = 0, 0.3, 0.45, 0.6). The mixed powders were first pressed into pellets under axial pressure (8 MPa) and calcinated at 700°C for 2 hours in air. After cooling down, these pellets were reground into fine powders and repressed into pellets under axial pressure (12 MPa). After sintering at 1150°C for 12 hours in air atmosphere, all the pellets were ground for 2 hours before characterizations and electrochemistry tests. $Sr_{0.5}Ba_{0.5}Fe_{0.45}Nb_{1.55}O_6$ denoted as SBNF45 and $Sr_{0.4}Ba_{0.4}Co_{0.2}Nb_2CoO_6$ denoted as (SBC)N were also prepared under the same conditions. $KNb_{0.775}Co_{0.225}O_3$ (KNC), $LiNb_{0.925}Co_{0.075}O_3$ (LNC075), and $LiNb_{0.775}Co_{0.225}O_3$ (LNC225) were prepared by following the same procedure except for their relatively lower final sintering temperature (1000°C). Commercial IrO_2 (99.9%) with a Brunauer-Emmett-Teller (BET) surface area of ~32.5 $m^2\ g^{-1}$ was also purchased from Aldrich Ltd and tested after grinding.

6.2.2 Materials characterization

X-Ray powder diffraction patterns (XRD) were recorded on a GBC eMMA X-ray diffractometer with Cu-Kα radiation and refined by the Pawley method. Scanning electron microscopy (SEM) and element mapping images were obtained on a JEOL JSM-7500FA and atomic arrangements from high-angle annular dark field (HAADF) and annular bright field (ABF) observations were conducted on a scanning transmission electron microscope (STEM, JEOL JEM-ARM200F). The Brunauer-Emmett-Teller (BET Nova 1000, Quantachrome Instrument) surface area was estimated based on the nitrogen adsorption/desorption isotherms. Raman spectra were collected at room temperature with a SPEX-1403 Laser Raman spectrometer excited by a 532 nm wavelength Ar^+ laser. Magnetization-temperature curves were measured under a 500 Oe magnetic field within the temperature range of 5–340 K on a Quantum Design physical properties measurement system (PPMS-9T) (Quantum Design, USA) with the vibrating sample magnetometer (VSM) option. Electronic structure was analyzed based on X-ray photoelectron spectra (XPS) collected on a SPECS XPS/Auger spectrometer, Co *L*-edge soft X-ray absorption spectra (XAS) from the BL12B-a facility of the National Synchrotron Radiation Laboratory (NSRL, P. R. China),

O *K*-edge spectra from the Soft X-ray Spectroscopy beamline at the Australian Synchrotron (AS, Australia), and Co *K*-edge spectra from BL14W1 facility of the Shanghai Synchrotron Radiation Facility (SSRF, P. R. China).

6.2.3 Electrochemical testing

For the preparation of working electrodes, 0.75 mL deionized water and 0.25 mL isopropanol, 2 mg carbon powder, 10 mg of electrocatalyst, and 0.1 mL of Nafion® 117 solution were mixed under ultrasound for 1 hour to form an homogenously mixed ink, and then 3 μL of above ink was drop casted onto a glassy carbon (GC) electrode 3 mm in diameter (effective electrode area 0.07065 cm^2, mass loading 0.38 mg cm^{-2}). OER performances were obtained on an electrochemical workstation (Ivium-n-Stat, Ivium Technologies) and a standard three-electrode electrochemical cell with saturated Ag/AgCl as reference electrode and platinum wire as the counter electrode. All the measurements were carried out in 1 M NaOH aqueous solution except for the pH-dependent linear sweep voltammetry (LSV) test. All LSV curves and Tafel plots were measured at a scan rate of 5 mV s^{-1}. Electrochemical impedance spectroscopy (EIS) was conducted at 1.6 V vs. reversible hydrogen electrode (RHE), over frequencies from 1–10^5 Hz. All the potentials vs. Ag/AgCl were converted to vs. RHE according to the Nernst Equation.

6.3 Crystal and electronic structure

From the XRD patterns in **Figure 6.1a**, we can see that the original TTB structure can be maintained when $x \leq 0.45$. A secondary phase identical to perovskite $KNbO_3$ (Cubic, space group P*m-3m*) would emerge, however, when $x \geq 0.6$. Thus, a Co-doped $KNbO_3$ perovskite with same Co/Nb ratio (KNC) was also prepared for a better comparison, the XRD pattern of which is also provided in **Figure 6.1a**. The specific crystal structure information can be obtained by the Retiveld refinement method, based on TTB $Sr_{0.5}Ba_{0.5}Nb_2O_{6-\delta}$ (Tetragonal, space group P4bm) prototype. The refined pattern of SBNC45 is displayed in **Figure 6.1b** (for other samples see **Figure 6.2**). The profile and weighted profile R factors (R_p and R_{wp}) are far smaller than 7% for the SBN, SBNC30, and SBNC45 samples, indicating the pure tetragonal tungsten bronze structure (TTB) phase when $x \leq 0.45$. The refined lattice parameters are listed in **Table 6.1**.

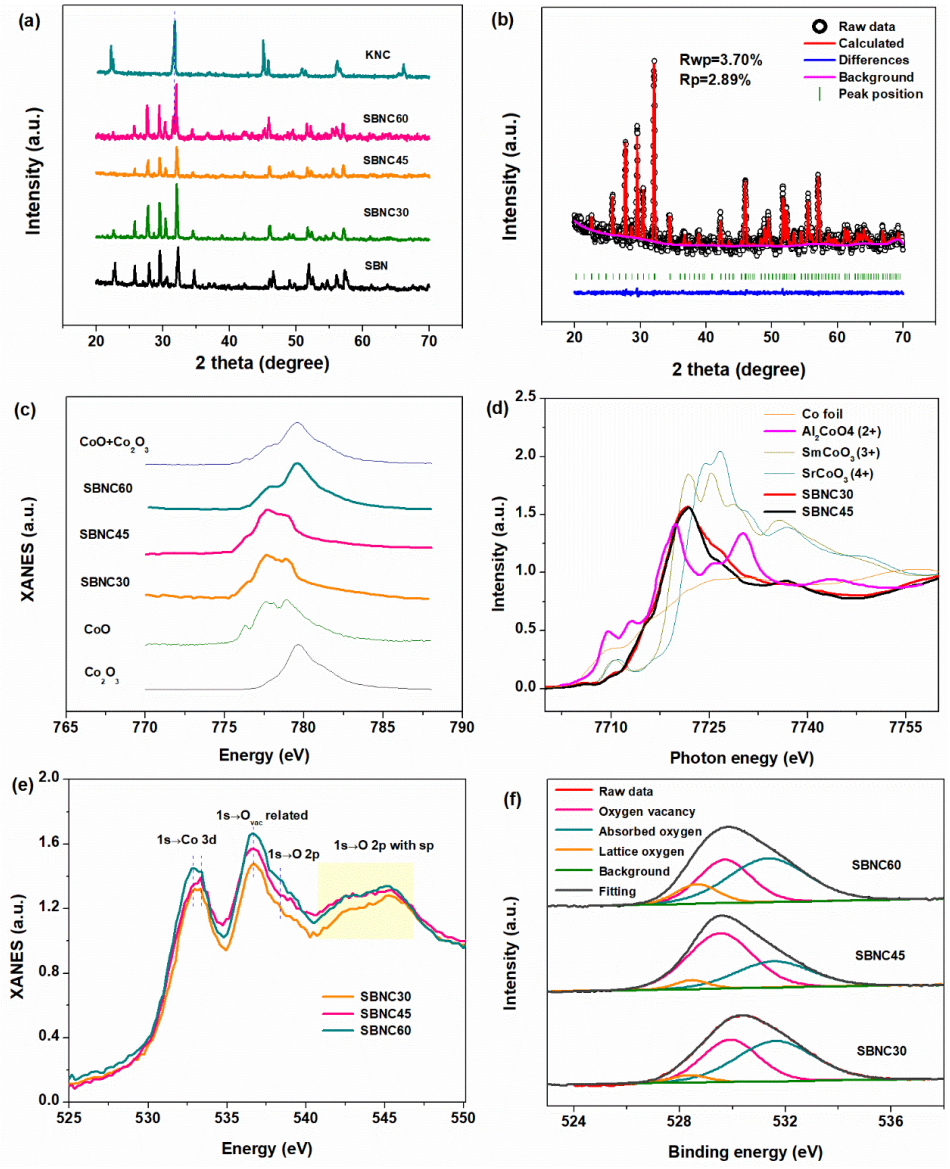

Figure 6.1 Structure characterization spectra. (a) XRD patterns of SBN, SBNC30, SBNC45, SBNC60 and KNC; (b) refined XRD pattern of SBNC45 as a demonstration; (c) Co L_3-edge XAS spectra recorded on the as-prepared samples as well as standard references; (d) Co K-edge XAS spectra of SBNC30 and SBNC45, and plots downloaded from https://materialsproject.org/ for comparison; (e) O K-edge XAS spectra of SBNC30, SBNC45, and SBNC60; (f) fitted XPS core level spectra of O 1s from SBNC30, SBNC45, and SBNC60.

The enlargement of the unit cell from SBN to SBNC45 can be clearly observed from **Table 6.1**, implying that Co has been successfully doped into the TTB crystal lattice. If Co cations are not incorporated into the TTB lattice, the unit cell is likely to shrink with reduced lattice parameters, given the insufficient supply of both Nb and Co.

Table 6.1 Lattice parameters from XRD refinement.

	SBN	SBNC30	SBNC45
a	12.4803 Å	12.4997 Å	12.5202 Å
b	12.4803 Å	12.4997 Å	12.5202 Å
c	3.9598 Å	3.9505 Å	3.9504 Å
Vol	616.7700 $Å^3$	617.2359$Å^3$	619.2466 $Å^3$

On the basis of the radii of the cations listed in **Table 6.2**, Co ions should have to occupy Nb sites in the TTB lattice. In addition, from original designs, only Nb sites with suitable size (0.78 Å) are left as vacancies reserved for Co, and Ba or Sr sites are well allocated with large cations (at least larger than 1.32 Å). On the contrary, if Co cations are located at Ba or Sr sites, then the Ba or Sr should have to find sites that are large enough for them, which is not available in the TTB structure. What is noteworthy is that there is a large probability that Co^{2+} rather than Co^{3+} enters Nb sites because the smaller radius of Co^{3+} (irrespective of the spin state) might also lead to lattice shrinkage, which is opposite to the XRD results. Herein, we draw a preliminary conclusion that Co has been successfully anchored in Nb sites with the valence state of Co^{2+}.

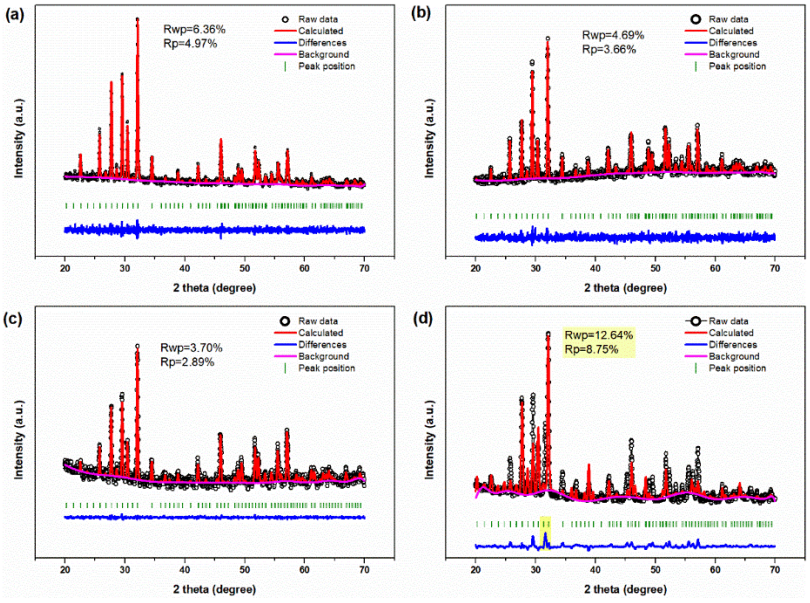

Figure 6.2 Refined XRD patterns based on the TTB Sr0.5Ba0.5Nb2O6-δ (Tetragonal, space group P4bm): (a) SBN; (b) SBNC30; (c) SBNC45, and (d) SBNC60, in which the marked peak in the Differences curve was most probably induced by the perovskite secondary phase.

To verify the above conclusion, XAS spectra of the Co L_3-edge were first conducted as shown in **Figure 6.1c**. Spectra of SBNC30 and SBNC45 coincide with the standard CoO (Co^{2+}), while SBNC60 sample contains both Co^{2+} and Co^{3+} compared to the spectra of reference samples CoO (Co^{2+}) and Co_2O_3 (Co^{3+}).

This implies that the TTB structure has the capacity to stabilize Co^{2+} cations in its lattice, while SBNC45 encompasses the maximum amount of Co^{2+}. Doping excessive Co into SBNC60 would generate a perovskite secondary phase containing Co^{3+}. This result can also be confirmed by the Co *K*-edge X-ray absorption near-edge structure (XANES) spectra in **Figure 6.1d**, which reflects the electronic dipole transition from the 1*s* level to the 4*p* levels. The absorption edge position of SBNC30 and SBNC45 agree with the Co^{2+} from the standard Al_2CoO_4. The pre-edge peak at 7100 eV is visibly in tetrahedral coordination, originating from the electron transition from the Co 1*s* to 3*d* orbitals. The octahedrally coordinated SBNC30 and SBNC45 reflect a certain degree of lattice distortion of the CoO_6 octahedra from the central symmetry [132].

Table 6.2 Parameters of cations in different coordination environments.

Cations	Electronic	Coordination	Spin state	Crystal Radii[a]	t_{2g}	e_g
Co^{4+}	$3d^5$	6	High spin	0.67 Å	3	2
Co^{3+}	$3d^6$	6	Low spin	0.69 Å	6	0
			High spin	0.75 Å	4	2
Co^{2+}	$3d^7$	6	Low spin	0.79 Å	6	1
			High spin	0.89 Å	5	2
Nb^{5+}	$4d^0$	6	-	0.78 Å	-	-
Sr^{2+}	$5s^0$	6	-	1.32 Å	-	-
		12	-	1.58 Å	-	-
Ba^{2+}	$6s^0$	6	-	1.49 Å	-	-
		12	-	1.75 Å	-	-

[a] These data are from: http://abulafia.mt.ic.ac.uk/shannon/p**Table**.php

The specific spin structure of Co^{2+} can be estimated based on the temperature dependence of the magnetization (*M*−*T*) curve and the Curie-Weiss law fitting [133,75]. From **Figure 6.3** we can see that the magnetization of all samples decreased with increasing temperature, and the inverse magnetic susceptibility curves fit very well with the Curie-Weiss law, suggesting an overall paramagnetic ground state. After calculation, the number of unpaired electrons of Co^{2+} in SBNC30 is found to be near 3, but it decreased to about 2 in SBNC45 (details in **Table 6.3**). This result implies that SBNC45 encompasses a larger proportion of LS Co^{2+} with fewer unpaired electrons, while SBNC30 contains more HS Co^{2+} with more unpaired electrons. It should be noted that the spin configuration estimated based on Curie-Weiss law is the average information for the bulk.

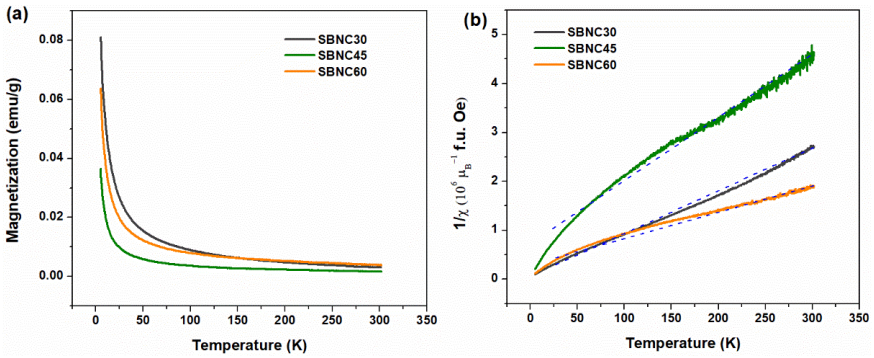

Figure 6.3 (a) Magnetization–temperature (M-T) curves for SBNC30, SBNC45, and SBNC60; (b) corresponding curves of inverse magnetic susceptibility versus temperature.

Table 6.3 Electronic parameters calculated based on the M-T curves and Curie-Weiss law.

	Curie constant (10^{-4} K μ_B Oe^{-1} f.u.$^{-1}$)	U_{eff} (μ_B)	Unpaired number [a] (n)	LS Co^{2+} [b] Percentage
SBNC30	1.19	4.21	3.3	Low
SBNC45	0.757	2.74	1.9	High

The original Nb sites are in the 5+ valance state in the TTB structure, but they accommodate Co^{2+}, which is reminiscent of a large amount of oxygen vacancy (O_{vac}) generation reducing the valence state of Co for the principle of electrical neutrality during the crystal growth. The generation of O_{vac} can be confirmed by the O K-edge XAS spectra in **Figure 6.1e**. Since only electron transition from O 1*s* to unoccupied states with O 2*p* character can be probed in O K-edge XAS, it gives information on the density of unoccupied O 2*p* states and hybridizing with transition metal 3*d* states [49]. The peak at 538.4 eV represents the transition from O 1*s* to O 2*p* and the broad peak range of 540-545 eV contains the transitions to O 2*p* hybrids with metal *sp* orbitals [134]. The absorption around 532.8-533.4 eV is caused by the electron transition from O 1*s* to Co 3*d*, while the absorption peak located at 536.7 eV reflects the electron transition from O 1*s* to oxygen vacancy (O_{vac}) related unoccupied 2*p* orbitals [135]. O K-edge XAS spectra with the features of the transition from O 1*s* to oxygen vacancy (O_{vac}) related unoccupied 2*p* orbitals confirm the existence of O_{vac} on the surface.

Further solid evidence can be observed in the O 1*s* core-level spectra in **Figure 6.1f**. The peaks with binding energy (BE) around 528.3-528.8 eV are signals from the electron transition of lattice oxygen (O_L). The peak ranging 531.6-531.7 eV is most likely contributed by surface adsorbed oxygen (O_{ad}), while the peak centered at 529.6-529.9 eV can be assigned to the less electron-rich oxygen species related to the oxygen vacancies (O_{vac}) [136]. As summarized in **Table 6.4**, the peak area from oxygen vacancy related

species is substantial for all the samples, from 41.1% for SBNC30 and 61.4% for SBNC45 to 39.7% for SBNC60, indicating that enormous amounts of oxygen vacancies (O_{vac}) are generated on their surfaces.

Table 6.4 Fitting parameters of O 1*s* core-level spectra.

	Peak1(eV)	Ratio	Peak2(eV)	Ratio	Peak3(eV)	Ratio
SBNC30	528.3	4.8%	529.9	41.1%	531.6	33.9%
SBNC45	528.5	4.7%	529.6	61.4%	531.7	54.1%
SBNC60	528.8	6.9%	529.7	39.7%	531.5	53.7%

Raman spectra investigated at room temperature in the frequency range of 100-1100 cm^{-1} can also provide some structural information (**Figure 6.4a**). The spectrum of SBN obtained here is well consistent with previous reports [137,138]. Spectra of SBNC30 and SBNC45 are similar to that of SBN but with obvious peak broadening, which is caused by additional disorder introduced by O_{vac} with cobalt substitution. Due to the complexity of the TTB structure, there are 45 atoms and 135 vibrational modes in the unit cell. Remarkably, there is the strongest peak located at around 834 cm^{-1} in SBNC30, SBNC45, and SBNC60, which cannot be observed in the SBN. This peak is identified as a vibrational mode of the CoO_6 octahedron, as detected in cobalt doped layered perovskite oxides [139]. Therefore, the emerging of this vibrational mode of the CoO_6 octahedron confirms that Co cations are octahedrally coordinated, excluding the possibility that Co may be located in the Ba/Sr sites, which are not octahedral environments.

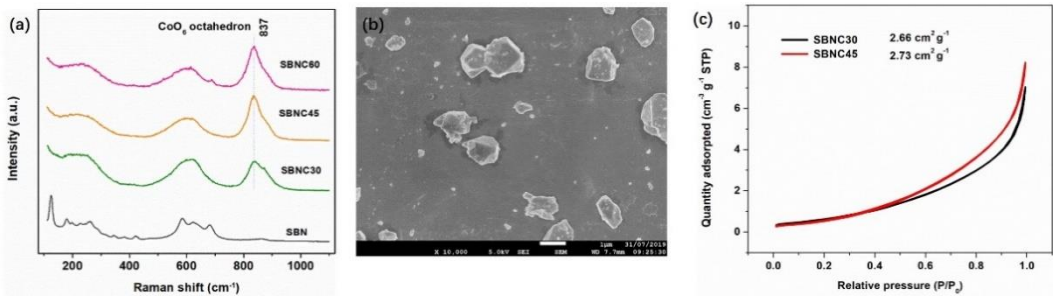

Figure 6.4 (a) Raman spectra of SBN, SBNC30, SBNC45, and SBNC60 at room temperature. The peak located at 837 cm-1 is attributed to the vibration modes of CoO_6 octahedra; (b) SEM image of SBNC45; (c) BET isotherms for SBNC30 and SBNC45.

Figure 6.5a presents the calculated crystal structure of SBNC45 based on the XRD refinement with two cells projected in the (001) plane. On average, the distances between Nb/CoO_6 octahedra are 3.73 Å

(50%), 3.79 Å (25%), and 3.97 Å (25%). The high percentage with the short distance of 3.73 Å makes the average distance between Nb/Co around 3.81 Å, which is smaller than for other Co based perovskite oxides such as $LaCoO_3$ (3.82 Å) and $SrCoO_3$ (3.86 Å). **Figure 6.5b** is a transmission electron microscope (TEM) image of a single crystal SBNC45 particle around 200 nm in size. It is noteworthy that some of the particles are polycrystals with a broad size distribution due to the high sintering temperature of the SSR method. The average particle size is about 1.5 μm, estimated from the SEM image (**Figure 6.5b**), so the sample has a relatively small BET surface area (~2.6 m^2 g^{-1}, **Figure 6.5c**).

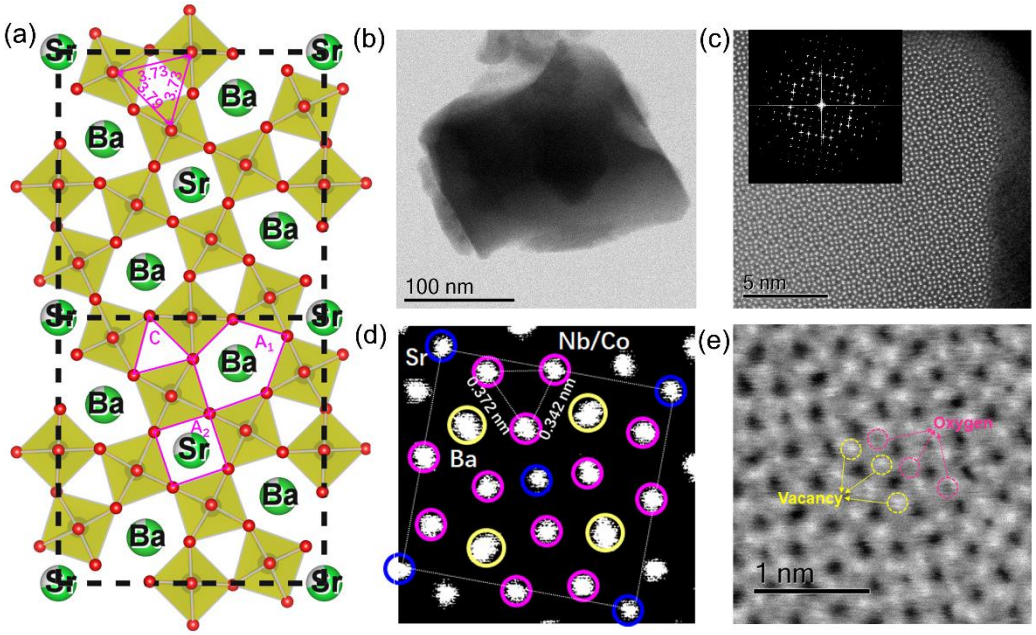

Figure 6.5 (a) Two unit cells projected on the (001) plane, based on the refined structure of SBNC45; all A sites are occupied by metal cations, but, in fact, they are partially occupied but randomly distributed; (b) TEM image of a SBNC45 particle around 200 nm in size; (c) HAADF image from the edge of the particle in **Figure 6.5b**, with the inset the corresponding SAED pattern by fast Fourier transform (FFT); (d) enlarged HAADF image from **Figure 6.5c** with the superposition of one unit cell marked with circles and lines; (e) ABF image with high magnification, in which the dark area marked in red circles is the oxygen atom column, while the bright area marked in yellow circles denotes the oxygen vacancies.

The TEM image in **Figure 6.5c** is a high-angle annular dark-field scanning transmission electron microscopy (HAADF-STEM) image recorded with the electron beam along the [001] zone axis, from which we can see that these atoms are highly organized in a crystalline pattern. The inset is the selected area electron diffraction (SAED) pattern corresponding to the lattice from the HAADF image, indicating

a good single crystallinity in that area. The enlarged HAADF image in **Figure 6.5d** with the superposition of a unit cell of the TTB structure confirms the pure phase of the as-prepared samples despite the Co doping. There are two adjacent Co/Nb sites as noted, with a spacing of 3.72 Å, which is consistent with the value of 3.73 Å from the XRD refinement. A distance of 3.42 Å for the other two adjacent Co/Nb cations is also observed, however, which is a characteristic of lattice distortion induced by oxygen vacancy (O_{vac}). **Figure 6.5e** is an annular bright-field scanning transmission electron microscope (ABF-STEM) image, enabling us to observe the atomic columns of both relatively heavy elements (metals) and light elements (oxygen) with the same contrast. The electrons that are incident on the oxygen vacancy (O_{vac}) columns will pass through directly, appearing as bright dots marked by yellow circles in the image. If oxygen atoms are present in the crystal lattice, then black dots will be observed instead, as marked with pink circles. It is obvious that the bright dots account for a dramatically larger proportion than the black dots in **Figure 6.5e**. This result from ABF is another piece of solid evidence that strongly affirms the existence of abundant oxygen vacancies (O_{vac}) on the surfaces of the as-prepared samples.

6.4 Electrochemical Tests

Linear-scan voltammetry (LSV) curves tested in 1 M NaOH electrolyte are displayed in **Figure 6.6a**, in which the current density (j) is calibrated by the disk electrode area (0.0765 cm^2). The current density at 1.7 V vs. RHE is 1.0 mA cm^{-2}, 12.9 mA cm^{-2}, 30.9 mA cm^{-2}, and 29.2 mA cm^{-2} for SBN, SBNC30, SBNC45, and SBNC60, respectively. The overpotential (η) at 10 mA cm^{-2} is about 460 mV, 400 mV, and 401 mV for the SBNC30, SBNC45, and SBNC60 samples, respectively. As expected, SBNC45 performed better than SBNC30 because more Co active sites were involved, although SBNC60 with more cobalt content exhibits similar OER activity to that of SBNC45. This phenomenon can be well explained by the crystal and electronic result that excessive Co in SBNC60 forms a perovskite secondary phase, although Co^{3+} in the perovskite secondary phase might not as active as Co^{2+} in the TTB structure. This is evidenced by the negligible OER performance of the perovskite KNC with the same Co ratio prepared by the same method (**Figure 6.7**). Thus, when part of the surface of TTB is covered by perovskite, it would result in a slightly reduced OER performance. The values of Tafel slopes can be calculated based on the Tafel curves in **Figure 6.6c**: 91 mV dec^{-1}, 60 mV dec^{-1}, 57 mV dec^{-1}, and 53 mV dec^{-1} for SBN, SBNC30, SBNC45, and SBNC60 respectively. Even though the Tafel slope of SBNC60 is slightly smaller than that of SBNC45, SBNC45 has a lower overpotential at $\log j = 0$. Thus, the result from the Tafel slope is in good agreement with that obtained from the LSV curves.

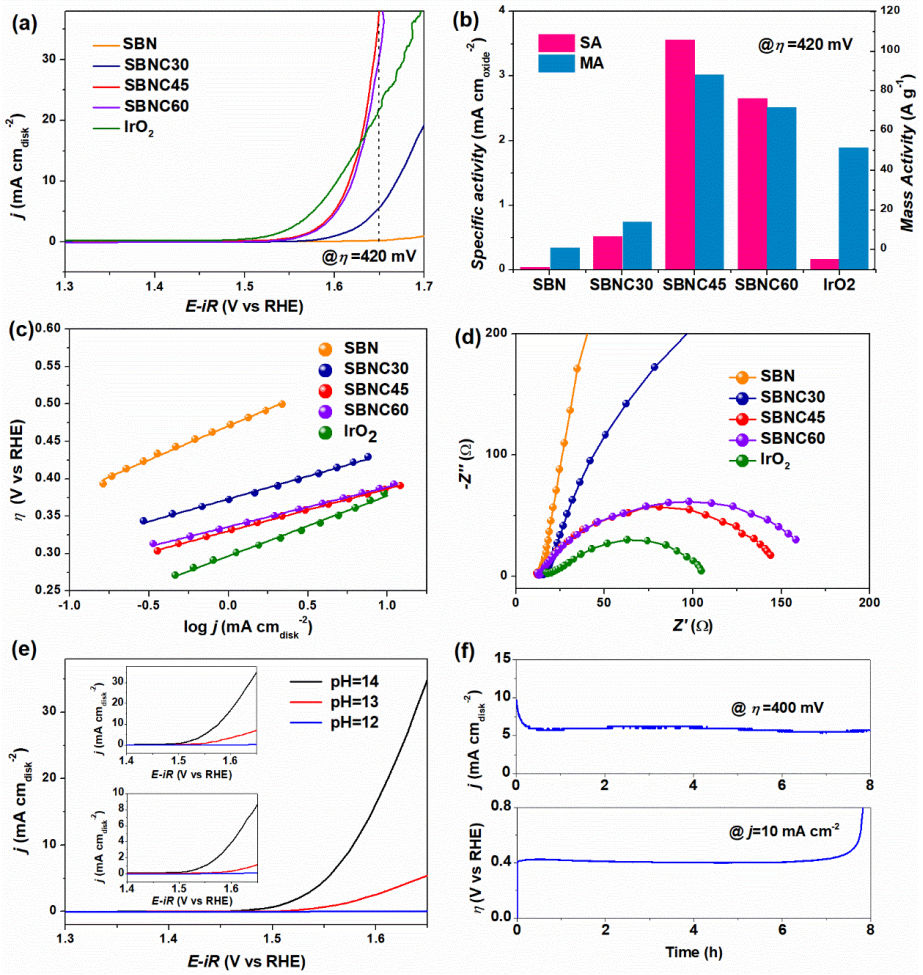

Figure 6.6 (a) LSV curves collected at the scan rate of 5 mV s-1 in 1 M NaOH; (b) Specific activity and mass activity at the overpotential of 420 mV; (c) Tafel plots with the scan rate of 5 mV s-1; (d) Nyquist plots measured at 1.6 V vs RHE, ranging from 1–105 Hz; (e) LSV curves of SBNC45 at the scan rate of 5 mV s^{-1} in 0.01 M NaOH, 0.1 M NaOH, and 1 M NaOH, insets are the corresponding curves measured on SBNC30 (top) and SBNC60 (bottom); (f) chronoamperometry (CA) curve (top) at the overpotential of 400 mV and chronopotentiometry (CP) curve (bottom) at the current density of 10 mA cm-2 with the duration of 8 hours tested on the SBNC45

To provide a clear comparison between these electrocatalysts, the mass activity (MA) and specific activity (SA) at overpotential η = 420 mV for all the samples are displayed in **Figure 6.6b**. The MA is the current density based on the current normalized by the corresponding mass of electrocatalyst, which is more useful in practical applications. The SA normalized by the total surface area can reflect the intrinsic activity of the catalyst, which is significant for fundamental research. In **Figure 6.6b**, an upward tendency can be observed from SBN to SBNC45, and then a downward tendency when it comes to SBNC60. This

general dependency is even more distinctive when evaluated from the SA rather than from the MA, which indicates that their intrinsic OER activity is even more different. We note that SBNC45, SBNC60, and even SBNC30 are better than state-of-the-art IrO_2 in terms of their intrinsic activity according to the SA results.

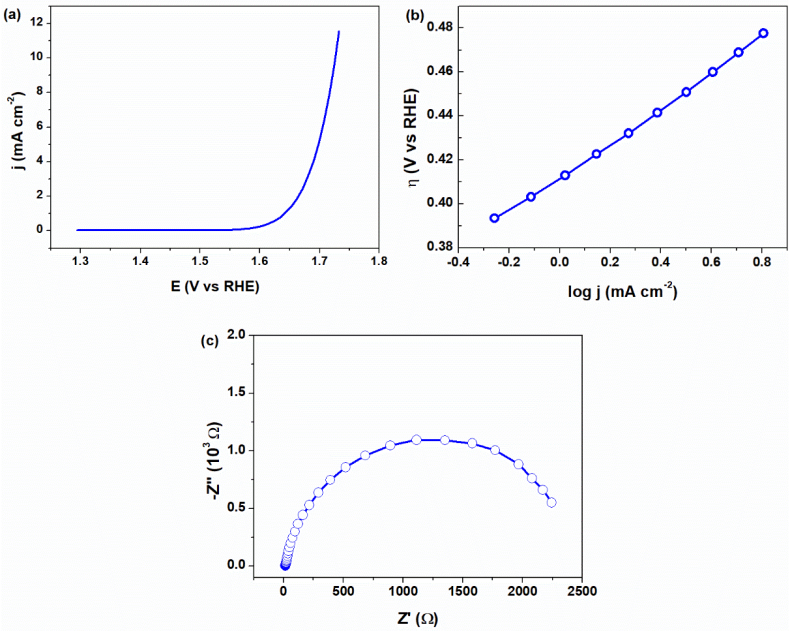

Figure 6.7 OER performance of KNC: (a) LSV curve with the scan rate of 5 mV s^{-1} ; (b) Tafel plot collected with the scan rate of 5 mV s^{-1}; (c) Nyquist plot measured at 1.6 V vs RHE, with the frequency ranging from 1–10^5 Hz.

The Nyquist plots in **Figure 6.6d** show that the polarization resistance (semicircle diameter) is decreased dramatically from SBN to SBNC60, which means that the electron transfer barrier is greatly reduced with increasing Co content. Being proportional to the electrochemical surface area (ECSA), the double-layer capacitance (C_{dl}) can provide another comparison. The calculated C_{dl} derived from the cyclic voltammograms (CVs, **Figure 6.8**) versus the scan rate is 1.10 mF cm^{-2} on SBNC30, 4.02 mF cm^{-2} on SBNC45, and 1.03 mF cm^{-2} on SBNC60. The higher C_{dl} value of SBNC45 implies that more enriched active sites are involved. Furthermore, LSV measurements on SBNC30 and SBNC45 were also conducted in NaOH electrolytes with different pH values. As shown in **Figure 6.6e** and the insets, the OER activities of SBNC30, SBNC45, and SBNC60 all exhibit a strong pH-dependent characteristic, implying a non-concerted proton–electron transfer related OER mechanism [16]. Long-term activity and stability were tested on SBNC45, as shown in **Figure 6.6f**. Both the chronoamperometry (CA) at the

overpotential of 400 mV and the chronopotentiometry (CP) at the current density of 10 mA cm^{-2} were stable over a duration of 8 hours, confirming the good performance stability of the SBNC45 sample. With respect to its structural stability, the high resolution TEM (HRTEM) in **Figure 6.9** suggests that SBNC45 can maintain its TTB structure with no obvious structural deterioration or surface amorphization.

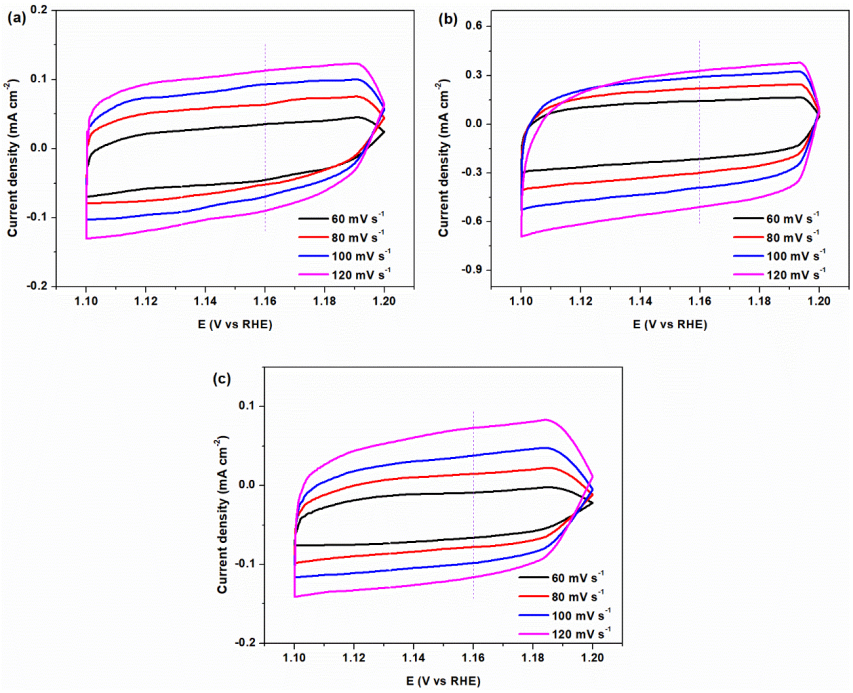

Figure 6.8 Cyclic voltammograms collected with different scan rates from 1.10–1.20 V vs RHE: (a) SBNC30; (b) SBNC45; (c) SBNC60.

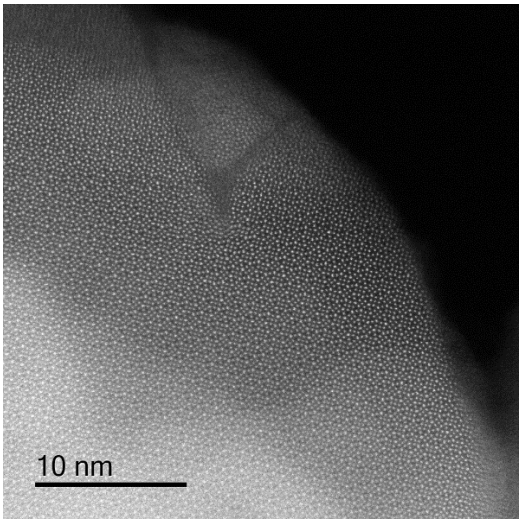

Figure 6.9 HRTEM-HAADF image of SBNC45 sample after the OER tests.

6.5 Discussion

The greatly improved OER performance of the cobalt doped TTB structured samples is likely to have originated from the allocation of low valence state Co^{2+} to the original high valence state Nb^{5+} sites, which leads to the generation of a tremendous amount oxygen vacancy (O_{vac}) (**Figure** 6.10a). One of the most amazing merits of the TTB structure is its unique octahedral connection network that is flexible enough to accommodate Co^{2+} cations together with O_{vac}. On the one hand, oxygen vacancy (O_{vac}) on the surface facilitates the adsorption of OH^- in the interface, as experimentally and theoretically proved by many researchers [11,13]. On the other hand, one O_{vac} in an oxygen containing octahedron could transform the coordination to pyramidal, with a degeneration of the 3*d* orbital energy, as illustrated in the diagram in **Figure 6.10b**. The evolution of this electronic structure will lead to a decrease in the number of unpaired electrons, which is confirmed by the results of the magnetization characterization.

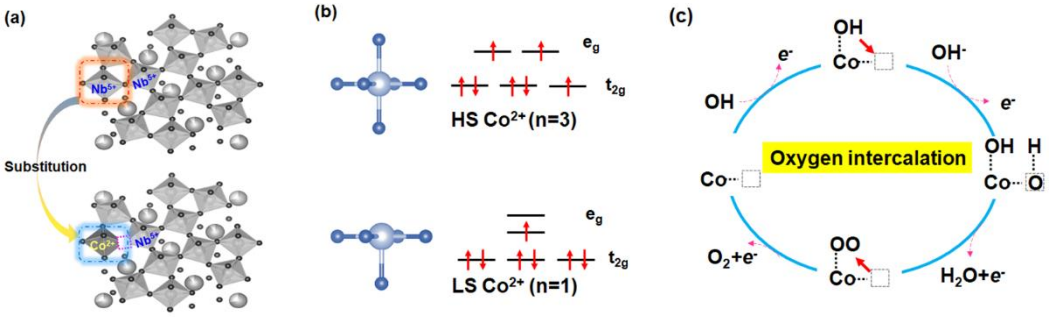

Figure 6.10 (a) Demonstration of the replacement of Nb^{5+} by Co in the TTB structure; (b) spin configuration evolution from HS Co^{2+} to LS Co^{2+} in the octahedron due to further crystal field splitting caused by the generation of oxygen vacancy; (c) a possible oxygen intercalation mechanism, with the dashed box representing the oxygen vacancy.

SBNC45, despite its poor electronic conductivity, exhibits 20 times higher current density than IrO_2 at 1.7 V vs. RHE when normalized by the BET surface area. It also has a rather small Tafel slope value (＜70 mV dec^{-1}) together with a pH-dependent characteristic, which indicates ultrafast non-concerted proton-electron transfer during the OER. This should be promoted by the combination of Co^{2+} and O_{vac} which are connected as Co-O_{vac}-Co when the Co sites are adequate. In this situation, an oxygen vacancy mediated oxygen intercalation mechanism may be possible, similar to the oxygen intercalation in the $LaMnO_3$ perovskite pseudocapacitor or the oxygen vacancy filling mechanism in CuO/CeO_2 catalysts [140,141]. As demonstrated in **Figure 6.10c**, starting from the adsorption of OH^- by a Co site on the surface in alkaline OER conditions, oxygen from OH· may be intercalated into the lattice when an adjacent lattice

oxygen is absent (O_{vac} site). Compared to high spin Co^{2+}, low spin Co^{2+} with less unpaired electrons and more empty orbitals is more efficient in the adsorption of OH^-. More O_{vac} makes oxygen intercalation easier. What is more important, the oxidation state of Co is increased after oxygen intercalation, which is more OER-active. **Figure 6.11** is the Co L_3-edge XAS spectra recorded on SBNC45 samples before and after the OER tests, from which it is observed that the Co cations on the surface have an electronic structure evolution from Co^{2+} to higher oxidation states.

According to the Zaanen–Sawatzky–Allen (ZSA) model, the electronic structure of transition metal oxides is typically described by three primary parameters: the Hubbard interaction (self-exchange), the metal–oxygen covalency (charge-transfer energy), and the metal–oxygen hybridization (orbital overlapping)[142]. The oxygen intercalation in the O_{vac} introduces high covalency between Co and oxygen, which will reduce the charge-transfer energy due to the increased ionization energy of Co cations with high valence. A small charge-transfer energy can alter the OER mechanism from concerted proton–electron transfer to non-concerted proton–electron transfer reactions. For example, in the concerted proton–electron transfer process, the addition of OH^- and the loss of e^- from O* to OOH* are coupled, which is pH-independent. They will be separated, however, in the non-concerted proton–electron transfer with a pH-dependent characteristic. A typical non-concerted proton–electron transfer mechanism is the lattice oxygen mechanism (LOM), in which O-O would directly be formed through bonding of O* on a metal active site with lattice oxygen. However, part of the oxygen in O_2 is from the crystal lattice for the traditional LOM electrocatalysts, which will lead to structural stability issues such as amorphization. In this oxygen intercalation mediated mechanism, all the oxygen element is from the electrolyte, even though some oxygen has even been inserted into the crystal lattice. Therefore, the electrocatalyst can maintain its original structure before and after OER tests.

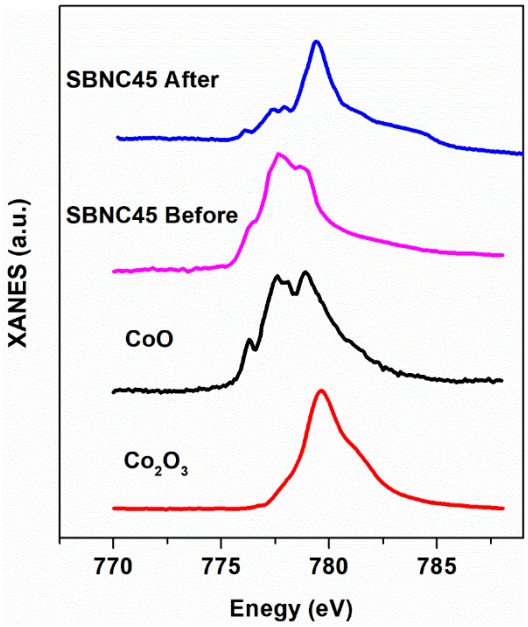

Figure 6.11 Co L_3-edge XAS spectra recorded on SBNC45 samples before and after the OER tests, as well as the standard reference samples.

We believe that the OER-active metal cations, enough oxygen vacancy, and a flexible structure are the essential conditions for this oxygen intercalation mechanism. It was evidenced by several reference samples prepared and tested under the same conditions (**Figure 6.12**). For example, the SBNF45 sample with the same amount of Fe doping into the Nb^{5+} sites, is not OER active, possibly due to the inefficient metal cations (Fe^{3+}), while the (SBC)N sample with Co doping into Sr^{2+} or Ba^{2+} sites is also not OER-active without adequate oxygen vacancy. Similarly, bad OER performances were also observed from the LNC075 and LNC225 samples with the same amount of Co occupying the Nb^{5+} sites in the trigonal crystal structure. The OER performance is limited by the rigid crystal structure, as in the situation of the perovskite KNC (**Figure 6.13**).

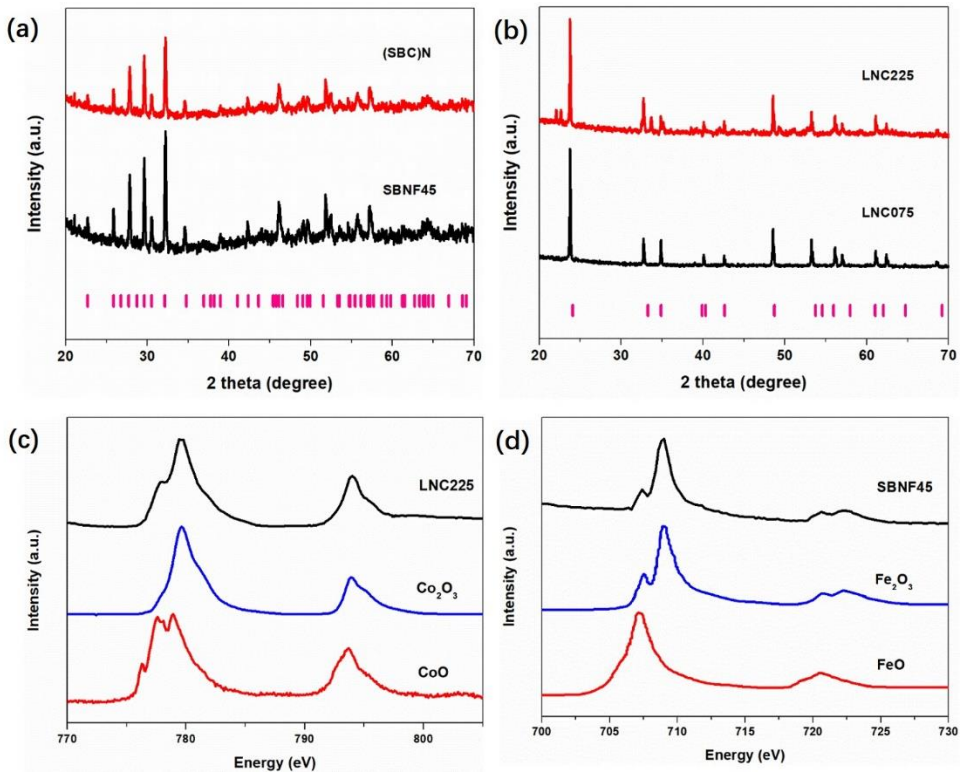

Figure 6.12 (a) XRD patterns of the SBNF45 and (SBC)N samples with comparison to the standard TTB structured SBN pattern. Both SBNF45 and (SBC)N can be regarded as pure phase; (b) XRD patterns of LNC075 and LNC225 samples with comparison to the standard LiNbO3 pattern. The LNC075 can be regarded as pure phase, but some impurity emerges in the LNC225 sample; (c) Co L-edge XAS spectra recorded from LNC225 and standard references CoO and Co2O3. Co in the LNC225 is identified as mainly 3+; (d) Fe L-edge XAS spectra recorded from SBNF45 and standard references FeO and Fe_2O_3. Fe in the SBNF45 is identified as mainly 3+.

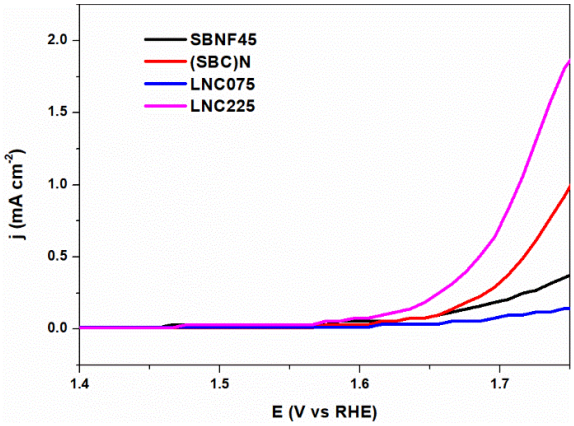

Figure 6.13 LSV curves of SBNF45, (SBC)N, LNC075, and LNC225 at the scan rate of 5 mV s^{-1}. These samples are not OER-active, as the current density is smaller than 1 mA cm^{-2} even at 1.7 V vs RHE.

6.6 Conclusion

High intrinsic OER activity is reported in the Co-doped tetragonal tungsten bronze (TTB) structure for the first time. TTB can maintain its structure with the harmonious coexistence of low-valence Co^{2+} and a huge amount of oxygen vacancy (O_{vac}). Due to this magic combination, the as-prepared SBNC45 sample exhibits superior performance to the state-of-the-art IrO_2 with a very small Tafel slope and a pH-dependent characteristic. The oxygen intercalation-mediated mechanism can expedite the OER process by non-concerted proton-electron transfer, but without compromising of the structure and the performance stability. This work indicates that the oxygen intercalation mechanism with a high reaction rate and good stability can be instructive for designing new electrocatalysts and that doping low valence state cations into high valence sites in the flexible structure is an effective strategy.

Chapter 7

7 General Conclusions and Outlook

7.1 General Conclusions

In this doctoral work, several strategies to enhance OER efficiency of transition metal oxides by regulating their electronic structures have been developed and demonstrated:

1. By composition substitution, the OER performance of Co substituted oxide is 100 times higher than for original Fe based compound, due to the fact that Co (3+, IS, $(t_{2g})^5(e_g)^1$) has an appropriate strength for a compromise between the absorption of reactants and the desorption of products. Furthermore, it requires low energy to provide an instantaneous change of state from $(t_{2g})^5(e_g)^1$ to $(t_{2g})^5(e_g)^2$.
2. By the corona poling method to align the internal polarization, OER property is further improved, resulting in the low overpotential of 320 mV at the current density of 10 mA cm^{-2} and a Tafel slope of 34 mV dec^{-1}. The phase, morphology and effects of ferroelectric polarization works all the time during the long term OER tests.
3. By anchoring low valence state Co on the high valence state Nb^{5+} sites in $Sr_{0.5}Ba_{0.5}Nb_2O_6$ (SBN), the occupation of Co in the Nb^{5+} sites of TTB structure brings about massive oxygen vacancy (O_{vac}) and stabilizes itself in the form of Co^{2+}. The coexistence of O_{vac} and LS Co^{2+} triggers an oxygen intercalation mechanism, endowing SBNC45 with superior OER performance to commercial IrO_2 under alkaline working conditions.

These strategies have been justified by the excellent OER performance and systematic electronic structure analysis. The results of this doctoral work is expected to be very suggestive for the rationally design for new type OER electrocatalysts with more ultrafast kinetics in the future.

7.2 Outlook

The rapid development of industrialization has raised growing concerns toward worldwide energy crisis and environmental problems, such as the shortage of fossil fuels and climate change. Advances in renewable energy largely rely on technologies for energy conversion and storage to mitigate intermittency issues associated with wind and sunlight. Potential key storage solution for highly renewable power systems is the conversion of electrical energy into chemical energy in the form of fuels. It could also

allow for a greater penetration of renewable energy in the chemical industry. The first and simplest step in this process could be to split water and generate hydrogen. There are two principal routes for this: in the near term, electricity could be used to drive electrolysers; in the longer term, the electrolysis process could be directly integrated with photovoltaics (PVs) in a photoelectrochemical (PEC) device [143]. Either way, to split water efficiently, both PV-electrolysis and PEC cells require highly performing catalysts for the two half reactions, the hydrogen evolution reaction (HER) and the oxygen evolution reaction (OER). However, the efficiency of hydrogen energy generation is limited by the oxygen evolution reaction (OER) due to its sluggish kinetics.

For the practical application of OER in acid, the best catalyst, considering both activity and stability, is IrO_2, although RuO_2 is often used together with IrO_2. However, even IrO_2 is not entirely stable under OER and iridium is an even more critical element than noble metal platinum [143]. Thus, it is desirable if Earth-abundant catalysts could be developed that could outcompete, and replace, platinum. A full and comprehensive understanding of the underlying physics of the OER is one the basics for designing high-efficient low-cost OER electrocatalysts. As revealed in Chapter 3, regardless of adopted mechanisms, the underlying rationale of OER is that three in four electrons being extracted from adsorbates should be in the same spin direction before O=O formation. This conclusion is with great significance in providing rational guidance for the more effective design of energy conversion electrocatalysts.

Although we have fully illustrated the role of spin in the OER process in the theory, it is still very challenging to experimentally observed and verified due to the limitation of current characterization techniques. The results of current works indicate that the underlying physics of the dependence of OER performance on the electronic structure can only be understood when considering the couplings between lattice, charge and orbital inside. Thus, a more deliberated platform with material foundation and computation are desired. Other strategies, such as modifying material preparation methods, can also be considered for tuning electronic structures. For example, a double perovskite oxide $La_{0.7}Sr_{1.3}Co_2O_{6-\delta}$ (LSCO) fabricated by three different solid-phase based methods were also prepared and investigated. By fully investigation on the structure and properties, it is found that the sample prepared with grain boundary exposed as the particle surface have shortened Co-O bond length, highly oxidized Co cations, plenty oxygen vacancies, as well as five times higher specific activity of OER tests.

References

1. Suntivich, J., Gasteiger, H.A., Yabuuchi, N., Nakanishi, H., Goodenough, J.B., Shao-Horn, Y.: Design principles for oxygen-reduction activity on perovskite oxide catalysts for fuel cells and metal-air batteries. Nat. Chem. **3**(7), 546-550 (2011).

2. Tang, T., Jiang, W.J., Niu, S., Liu, N., Luo, H., Chen, Y.Y., Jin, S.F., Gao, F., Wan, L.J., Hu, J.S.: Electronic and morphological dual modulation of cobalt carbonate hydroxides by Mn doping toward highly efficient and stable bifunctional electrocatalysts for overall water splitting. J. Am. Chem. Soc. **139**(24), 8320-8328 (2017).

3. Hwang, J., Rao, R.R., Giordano, L., Katayama, Y., Yu, Y., Shao-Horn, Y.: Perovskites in catalysis and electrocatalysis. Science **358**, 751–756 (2017).

4. Li, X., Wang, H., Cui, Z., Li, Y., Xin, S., Zhou, J., Long, Y., Jin, C., Goodenough, J.B.: Exceptional oxygen evolution reactivities on $CaCoO_3$ and $SrCoO_3$. Sci. Adv. **5**, eaav6262 (2019).

5. Hwang, J., Feng, Z., Charles, N., Wang, X.R., Lee, D., Stoerzinger, K.A., Muy, S., Rao, R.R., Lee, D., Jacobs, R., Morgan, D., Shao-Horn, Y.: Tuning perovskite oxides by strain: Electronic structure, properties, and functions in (electro)catalysis and ferroelectricity. Mater. Today **31**, 100-118 (2019).

6. Pinta, C., Fuchs, D., Merz, M., Wissinger, M., Arac, E., v. Löhneysen, H., Samartsev, A., Nagel, P., Schuppler, S.: Suppression of spin-state transition in epitaxially strained $LaCoO_3$. Phys. Review B **78**(17) (2008).

7. Björketun, M.E., Castelli, I.E., Rossmeisl, J., Olsen, T., Ukai, K., Kato, M., Dennler, G., Jacobsen, K.W.: Defect chemistry and electrical conductivity of Sm-doped $La_{1-x}Sr_xCoO_{3-\delta}$ for solid oxide fuel cells. J. Phys. Chem. C **121**(28), 15017-15027 (2017).

8. Garcés-Pineda, F.A., Blasco-Ahicart, M., Nieto-Castro, D., López, N., Galán-Mascarós, J.R.: Direct magnetic enhancement of electrocatalytic water oxidation in alkaline media. Nat. Energy **4**(6), 519-525 (2019).

9. Tahini, H.A., Tan, X., Schwingenschlögl, U., Smith, S.C.: In operando self-healing of perovskite electrocatalysts: A case study of $SrCoO_3$ for the oxygen evolution reaction. Part. Part. Syst. Char. **34**(4), 1600280 (2017).

10. Stoerzinger, K.A., Choi, W.S., Jeen, H., Lee, H.N., Shao-Horn, Y.: Role of strain and conductivity in oxygen electrocatalysis on $LaCoO_3$ thin films. J. Phys. Chem. Lett. **6**(3), 487-492 (2015).

11. Grimaud, A., Diaz-Morales, O., Han, B., Hong, W.T., Lee, Y.L., Giordano, L., Stoerzinger, K.A., Koper, M.T.M., Shao-Horn, Y.: Activating lattice oxygen redox reactions in metal oxides to catalyse

oxygen evolution. Nat. Chem. **9**(5), 457-465 (2017).

12. Tahini, H.A., Tan, X., Schwingenschlögl, U., Smith, S.C.: Formation and migration of oxygen vacancies in $SrCoO_3$ and their effect on oxygen evolution reactions. ACS Catal. **6**(8), 5565-5570 (2016).

13. Mefford, J.T., Rong, X., Abakumov, A.M., Hardin, W.G., Dai, S., Kolpak, A.M., Johnston, K.P., Stevenson, K.J.: Water electrolysis on $La_{1-x}Sr_xCoO_{3-\delta}$ perovskite electrocatalysts. Nat. Commun. **7**, 11053 (2016).

14. Cheng, X., Fabbri, E., Nachtegaal, M., Castelli, I.E., Kazzi, M.E., Haumont, R., Marzari, N., Schmidt, T.J.: Oxygen evolution reaction on $La_{1-x}Sr_xCoO_3$ perovskites: A combined experimental and theoretical study of their structural, electronic, and electrochemical properties. Chem. Mater. **27**, 7662-7672 (2015).

15. Suen, N.T., Hung, S.F., Quan, Q., Zhang, N., Xu, Y.J., Chen, H.M.: Electrocatalysis for the oxygen evolution reaction: Recent development and future perspectives. Chem. Soc. Rev. **46**(2), 337-365 (2017).

16. Wang, X., Sun, P., Lu, H., Tang, K., Li, Q., Wang, C., Mao, Z., Ali, T., Yan, C.: Aluminum-Tailored Energy Level and Morphology of Co3- x Alx O4 Porous Nanosheets toward Highly Efficient Electrocatalysts for Water Oxidation. Small **15**(11), e1804886 (2019).

17. Zhou, Y., Sun, S., Wei, C., Sun, Y., Xi, P., Feng, Z., Xu, Z.J.: Significance of Engineering the Octahedral Units to Promote the Oxygen Evolution Reaction of Spinel Oxides. Advanced materials **31**(41), e1902509 (2019).

18. Fan, K., Chen, H., Ji, Y., Huang, H., Claesson, P.M., Daniel, Q., Philippe, B., Rensmo, H., Li, F., Luo, Y., Sun, L.: Nickel-vanadium monolayer double hydroxide for efficient electrochemical water oxidation. Nature communications **7**, 11981 (2016).

19. Hao, C., Wu, Y., An, Y., Cui, B., Lin, J., Li, X., Wang, D., Jiang, M., Cheng, Z., Hu, S.: Interface-coupling of CoFe-LDH on MXene as high-performance oxygen evolution catalyst. Materials Today Energy **12**, 453-462 (2019).

20. Medford, A.J., Vojvodic, A., Hummelshøj, J.S., Voss, J., Abild-Pedersen, F., Studt, F., Bligaard, T., Nilsson, A., Nørskov, J.K.: From the Sabatier principle to a predictive theory of transition-metal heterogeneous catalysis. J. Catal. **328**, 36-42 (2015).

21. Bockris, J.O.M., Otagaw, T.: The electrocatalysis of oxygen evolution on perovskites. J. Electrochem. Soc. **131**, 290-302 (1984).

22. Chung, D.Y., Lopes, P.P., Farinazzo Bergamo Dias Martins, P., He, H., Kawaguchi, T., Zapol, P., You, H., Tripkovic, D., Strmcnik, D., Zhu, Y., Seifert, S., Lee, S., Stamenkovic, V.R., Markovic, N.M.:

Dynamic stability of active sites in hydr(oxy)oxides for the oxygen evolution reaction. Nat. Energy **5**(3), 222-230 (2020).

23. Man, I.C., Su, H.-Y., Calle-Vallejo, F., Hansen, H.A., Martínez, J.I., Inoglu, N.G., Kitchin, J., Jaramillo, T.F., Nørskov, J.K., Rossmeisl, J.: Universality in oxygen evolution electrocatalysis on oxide surfaces. ChemCatChem **3**(7), 1159-1165 (2011).

24. Calle-Vallejo, F., Díaz-Morales, O.A., Kolb, M.J., Koper, M.T.M.: Why is bulk thermochemistry a good descriptor for the electrocatalytic activity of transition metal oxides? ACS Catal. **5**(2), 869-873 (2015).

25. Lim, T., Niemantsverdriet, J.W.H., Gracia, J.: Layered antiferromagnetic ordering in the most active perovskite catalysts for the oxygen evolution reaction. ChemCatChem **8**(18), 2968-2974 (2016).

26. Cheng, X., Fabbri, E., Yamashita, Y., Castelli, I.E., Kim, B., Uchida, M., Haumont, R., Puente-Orench, I., Schmidt, T.J.: Oxygen evolution reaction on perovskites: a multieffect descriptor study combining experimental and theoretical methods. ACS Catal. **8**(10), 9567-9578 (2018).

27. Koper, M.T.M.: Theory of multiple proton–electron transfer reactions and its implications for electrocatalysis. Chem. Sci. **4**(7), 2710–2723 (2013).

28. Hong, W.T., Risch, M., Stoerzinger, K.A., Grimaud, A., Suntivich, J., Shao-Horn, Y.: Toward the rational design of non-precious transition metal oxides for oxygen electrocatalysis. Energ. Environ. Sci. **8**(5), 1404-1427 (2015).

29. Yagi, S., Yamada, I., Tsukasaki, H., Seno, A., Murakami, M., Fujii, H., Chen, H., Umezawa, N., Abe, H., Nishiyama, N., Mori, S.: Covalency-reinforced oxygen evolution reaction catalyst. Nat. Commun. **6**, 8249 (2015).

30. Sun, W., Wang, Z., Zaman, W.Q., Zhou, Z., Cao, L., Gong, X.Q., Yang, J.: Effect of lattice strain on the electro-catalytic activity of IrO_2 for water splitting. Chem. Commun. **54**(8), 996-999 (2018).

31. Chen, X., Aschaffenburg, D.J., Cuk, T.: Selecting between two transition states by which water oxidation intermediates decay on an oxide surface. Nat. Catal. **2**(9), 820-827 (2019).

32. Mueller, D.N., Machala, M.L., Bluhm, H., Chueh, W.C.: Redox activity of surface oxygen anions in oxygen-deficient perovskite oxides during electrochemical reactions. Nat. Commun. **6**(1), 6097 (2015).

33. Yoo, J.S., Rong, X., Liu, Y., Kolpak, A.M.: Role of lattice oxygen participation in understanding trends in the oxygen evolution reaction on perovskites. ACS Cata. **8**(5), 4628-4636 (2018).

34. Zou, X., Zhang, Y.: Noble metal-free hydrogen evolution catalysts for water splitting. Chem. Soc.

Rev. **44**(15), 5148-5180 (2015).

35. Liu, Y., Xiao, C., Huang, P., Cheng, M., Xie, Y.: Regulating the charge and spin ordering of two-dimensional ultrathin solids for electrocatalytic water splitting. Chem **4**(6), 1263-1283 (2018).

36. Mabayoje, O., Shoola, A., Wygant, B.R., Mullins, C.B.: The role of anions in metal chalcogenide oxygen evolution catalysis: electrodeposited thin films of nickel sulfide as "pre-catalysts". ACS Energy Lett. **1**(1), 195-201 (2016).

37. McFarland, E.W., Metiu, H.: Catalysis by doped oxides. Chem. Rev. **113**(6), 4391-4427 (2013).

38. Jiao, Y., Sharpe, R., Lim, T., Niemantsverdriet, J.W.H., Gracia, J.: Photosystem II acts as a spin-controlled electron gate during oxygen formation and evolution. J. Am. Chem. Soc. **139**(46), 16604-16608 (2017).

39. Chretien, S., Metiu, H.: O_2 evolution on a clean partially reduced rutile TiO_2(110) surface and on the same surface precovered with Au_1 and Au_2: the importance of spin conservation. J. Chem. Phys. **129**(7), 074705 (2008).

40. Torun, E., Fang, C.M., de Wijs, G.A., de Groot, R.A.: Role of magnetism in catalysis: RuO_2 (110) surface. J. Phys. Chem. C **117**(12), 6353-6357 (2013).

41. Gracia, J., Sharpe, R., Munarriz, J.: Principles determining the activity of magnetic oxides for electron transfer reactions. J. Catal. **361**, 331-338 (2018).

42. Reier, T., Nong, H.N., Teschner, D., Schlögl, R., Strasser, P.: Electrocatalytic oxygen evolution reaction in acidic environments - reaction mechanisms and catalysts. Adv. Energy Mater. **7**(1), 1601275 (2017).

43. Tao, H.B., Xu, Y., Huang, X., Chen, J., Pei, L., Zhang, J., Chen, J.G., Liu, B.: A general method to probe oxygen evolution intermediates at operating conditions. Joule **3**(6), 1498-1509 (2019).

44. Sun, Y., Lu, Y., Li, X., Yu, Z., Zhang, S., Sun, H., Cheng, Z.: Flexible hybrid piezo/triboelectric energy harvester with high power density workable at elevated temperatures. Journal of Materials Chemistry A **8**(24), 12003-12012 (2020).

45. Zhao, X., Zhang, H., Yan, Y., Cao, J., Li, X., Zhou, S., Peng, Z., Zeng, J.: Engineering the electrical conductivity of lamellar silver-doped cobalt(II) selenide nanobelts for enhanced oxygen evolution. Angew. Chem. **56**(1), 328-332 (2017).

46. Oliver-Tolentino, M.A., Vázquez-Samperio, J., Manzo-Robledo, A., González-Huerta, R.d.G., Flores-Moreno, J.L., Ramírez-Rosales, D., Guzmán-Vargas, A.: An approach to understanding the

electrocatalytic activity enhancement by superexchange interaction toward OER in alkaline media of Ni–Fe LDH. J. Phys. Chem. C **118**(39), 22432-22438 (2014).

47. Calle-Vallejo, F., Inoglu, N.G., Su, H.-Y., Martínez, J.I., Man, I.C., Koper, M.T.M., Kitchin, J.R., Rossmeisl, J.: Number of outer electrons as descriptor for adsorption processes on transition metals and their oxides. Chem. Sci. **4**(3), 1245-1249 (2013).

48. Biesinger, M.C., Payne, B.P., Grosvenor, A.P., Lau, L.W.M., Gerson, A.R., Smart, R.S.C.: Resolving surface chemical states in XPS analysis of first row transition metals, oxides and hydroxides: Cr, Mn, Fe, Co and Ni. Appl. Surf. Sci. **257**(7), 2717-2730 (2011).

49. Suntivich, J., Hong, W.T., Lee, Y.-L., Rondinelli, J.M., Yang, W., Goodenough, J.B., Dabrowski, B., Freeland, J.W., Shao-Horn, Y.: Estimating hybridization of transition metal and oxygen states in perovskites from O K-edge X-ray absorption spectroscopy. J. Phys. Chem. C **118**(4), 1856-1863 (2014).

50. Aken, P.A.v., Liebscher, B., Styrsa, V.J.: Quantitative determination of iron oxidation states in minerals using Fe $L_{2,3}$-edge electron energy-loss near-edge structure spectroscopy. Phys. Chem. Minerals **25**, 323-327 (1998).

51. Chen, J.Y., Dang, L., Liang, H., Bi, W., Gerken, J.B., Jin, S., Alp, E.E., Stahl, S.S.: Operando analysis of NiFe and Fe oxyhydroxide electrocatalysts for water oxidation: Detection of Fe^{4+} by mossbauer spectroscopy. J. Am. Chem. Soc. **137**(48), 15090-15093 (2015).

52. Karppinen, M., Fukuoka, A., ¨o, L.N., Yamauchi, H.: Determination of oxygen content and metal valences in oxide superconductors by chemical methods. Supercond. Sci. Technol. **9**, 121-135 (1996).

53. Zhou, J.-S., Goodenough, J.B.: Paramagnetic phase in single-crystal $LaMnO_3$. Phys. Rev. B **60**, R15002-R15004 (1999).

54. Malkhandi, S., Yang, B., Manohar, A.K., Manivannan, A., Prakash, G.K., Narayanan, S.R.: Electrocatalytic properties of nanocrystalline calcium-doped lanthanum cobalt oxide for bifunctional oxygen electrodes. J. Phys. Chem. Lett. **3**(8), 967-972 (2012).

55. Liu, S., Luo, H., Li, Y., Liu, Q., Luo, J.-L.: Structure-engineered electrocatalyst enables highly active and stable oxygen evolution reaction over layered perovskite $LaSr_3Co_{1.5}Fe_{1.5}O_{10-\delta}$. Nano Energy **40**, 115-121 (2017).

56. Grimaud, A., Hong, W.T., Shao-Horn, Y., Tarascon, J.M.: Anionic redox processes for electrochemical devices. Nat. Mater. **15**(2), 121-126 (2016).

57. Gracia, J.: Spin dependent interactions catalyse the oxygen electrochemistry. Phys. Chem. Chem.

Phys. **19**(31), 20451-20456 (2017).

58. Grimaud, A., Carlton, C.E., Risch, M., Hong, W.T., May, K.J., Shao-Horn, Y.: Oxygen evolution activity and stability of $Ba_6Mn_5O_{16}$, $Sr_4Mn_2CoO_9$, and $Sr_6Co_5O_{15}$: the influence of transition metal coordination. J. Phys. Chem. C **117**(49), 25926-25932 (2013).

59. Anantharaj, S., Ede, S.R., Sakthikumar, K., Karthick, K., Mishra, S., Kundu, S.: Recent trends and perspectives in electrochemical water splitting with an emphasis on sulfide, selenide, and phosphide catalysts of Fe, Co, and Ni: A review. ACS Catal. **6**(12), 8069-8097 (2016).

60. Suntivich, J., May, K.J., A.Gasteiger, H., Goodenough, J.B., Shao-Horn, Y.: A perovskite oxide optimized for oxygen evolution catalysis from molecular orbital principles. Science **334**, 1383-1385 (2011).

61. Tong, Y., Guo, Y., Chen, P., Liu, H., Zhang, M., Zhang, L., Yan, W., Chu, W., Wu, C., Xie, Y.: Spin-state regulation of perovskite cobaltite to realize enhanced oxygen evolution activity. Chem **3**(5), 812-821 (2017).

62. Zhou, S., Miao, X., Zhao, X., Ma, C., Qiu, Y., Hu, Z., Zhao, J., Shi, L., Zeng, J.: Engineering electrocatalytic activity in nanosized perovskite cobaltite through surface spin-state transition. Nat. Commun. **7**, 11510 (2016).

63. Zhu, Y., Zhou, W., Chen, Z.G., Chen, Y., Su, C., Tade, M.O., Shao, Z.: $SrNb_{0.1}Co_{0.7}Fe_{0.2}O_{3-\delta}$ perovskite as a next-generation electrocatalyst for oxygen evolution in alkaline solution. Angew. Chem. **54**(13), 3897-3901 (2015).

64. Chen, S., Kang, Z., Hu, X., Zhang, X., Wang, H., Xie, J., Zheng, X., Yan, W., Pan, B., Xie, Y.: Delocalized spin states in 2D atomic layers realizing enhanced electrocatalytic oxygen evolution. Adv. Mater. **29**(30), 1701687 (2017).

65. Maitra, U., Naidu, B.S., Govindaraj, A., Rao, C.N.: Importance of trivalency and the e_g^1 configuration in the photocatalytic oxidation of water by Mn and Co oxides. PNAS **110**(29), 11704-11707 (2013).

66. Guo, Y., Tong, Y., Chen, P., Xu, K., Zhao, J., Lin, Y., Chu, W., Peng, Z., Wu, C., Xie, Y.: Engineering the electronic state of a perovskite electrocatalyst for synergistically enhanced oxygen evolution reaction. Adv. Mater. **27**(39), 5989-5994 (2015).

67. Ramírez, A., Hillebrand, P., Stellmach, D., May, M.M., Bogdanoff, P., Fiechter, S.: Evaluation of MnO_x, Mn_2O_3, and Mn_3O_4 electrodeposited films for the oxygen evolution reaction of water. J. Phys. Chem. C **118**(26), 14073-14081 (2014).

68. Robinson, D.M., Go, Y.B., Mui, M., Gardner, G., Zhang, Z., Mastrogiovanni, D., Garfunkel, E., Li, J., Greenblatt, M., Dismukes, G.C.: Photochemical water oxidation by crystalline polymorphs of manganese oxides: structural requirements for catalysis. J. Am. Chem. Soc. **135**(9), 3494-3501 (2013).

69. Arima, T., Tokura, Y., Torrance, J.B.: Variation of optical gaps in perovskite-type 3*d* transition-metal oxides. Phys. Rev. B **48**(23), 17006-17009 (1993).

70. Yamada, I., Fujii, H., Takamatsu, A., Ikeno, H., Wada, K., Tsukasaki, H., Kawaguchi, S., Mori, S., Yagi, S.: Bifunctional oxygen reaction catalysis of quadruple manganese perovskites. Adv. Mater. **29**(4), 1603004 (2017).

71. Gracia, J., Sharpe, R., Munarriz, J.: Principles determining the activity of magnetic oxides for electron transfer reactions. J Cata. **361** 331-338 (2018).

72. Suntivich, J., May, K.J., Gasteiger, H.A., Goodenough, J.B., Shao-Horn, Y.: A perovskite oxide optimized for oxygen evolution catalysis from molecular orbital principles. Science **334**, 1383-1385 (2011).

73. Iwakura, C., Nishioka, M., Tamura, H.: Oxygen evolution on spinel type ferrite film electrodes. Nippon Kagaku Kaishi **130**, C242 (1982).

74. Sharpe, R., Munarriz, J., Lim, T., Jiao, Y., Niemantsverdriet, J.W., Polo, V., Gracia, J.: Orbital physics of perovskites for the oxygen evolution reaction. Top. Catal. **61**(3-4), 267-275 (2018).

75. Li, X., Sun, Y., Wu, Q., Liu, H., Gu, W., Wang, X., Cheng, Z., Fu, Z., Lu, Y.: Optimized electronic configuration to improve the surface absorption and bulk conductivity for enhanced oxygen evolution reaction. J. Am. Chem. Soc. **141**(7), 3121-3128 (2019).

76. Liu, H., Yin, X., Cheng, H., Li, X., Zhang, Y., Gu, W., Zou, W., Zhu, L., Wu, Q., Huang, H., Wang, J., Ye, B., Fu, Z., Lu, Y.: Quantitative correlations between photochemical performance and low-electron-density defect. Applied Surface Science **527**, 146688 (2020).

77. Maruthapandian, V., Pandiarajan, T., Saraswathy, V., Muralidharan, S.: Oxygen evolution catalytic behaviour of Ni doped Mn_3O_4 in alkaline medium. RSC Adv. **6**(54), 48995-49002 (2016).

78. Gao, X., Zhang, H., Li, Q., Yu, X., Hong, Z., Zhang, X., Liang, C., Lin, Z.: Hierarchical $NiCo_2O_4$ hollow microcuboids as bifunctional electrocatalysts for overall water-splitting. Angew. Chem. **55**(21), 6290-6294 (2016).

79. Grimaud, A., May, K.J., Carlton, C.E., Lee, Y.L., Risch, M., Hong, W.T., Zhou, J., Shao-Horn, Y.: Double perovskites as a family of highly active catalysts for oxygen evolution in alkaline solution. Nat.

Commun. **4**, 2439 (2013).

80. Mtangi, W., Tassinari, F., Vankayala, K., Vargas Jentzsch, A., Adelizzi, B., Palmans, A.R., Fontanesi, C., Meijer, E.W., Naaman, R.: Control of electrons' spin eliminates hydrogen peroxide formation during water splitting. J. Am. Chem. Soc. **139**(7), 2794-2798 (2017).

81. Song, F., Bai, L., Moysiadou, A., Lee, S., Hu, C., Liardet, L., Hu, X.: Transition metal oxides as electrocatalysts for the oxygen evolution reaction in alkaline solutions: An application-Inspired renaissance. J. Am. Chem. Soc. **140**(25) (2018).

82. Lee, J.G., Hwang, J., Hwang, H.J., Jeon, O.S., Jang, J., Kwon, O., Lee, Y., Han, B., Shul, Y.G.: A new family of perovskite ctalysts for oxygen-evolution reaction in alkaline media: $BaNiO_3$ and $BaNi_{0.83}O_{2.5}$. J. Am. Chem. Soc. **138**(10), 3541-3547 (2016).

83. Chen, D., Chen, C., Baiyee, Z.M., Shao, Z., Ciucci, F.: Nonstoichiometric oxides as low-cost and highly-efficient oxygen reduction/evolution catalysts for low-temperature electrochemical devices. Chem. Rev. **115**(18), 9869-9921 (2015).

84. Kim, J., Yin, X., Tsao, K.C., Fang, S., Yang, H.: $Ca_2Mn_2O_5$ as oxygen-deficient perovskite electrocatalyst for oxygen evolution reaction. J. Am. Chem. Soc. **136**(42), 14646-14649 (2014).

85. Lam, K., Gao, Y., Wang, J., Ciucci, F.: H_2O_2 treated $La_{0.8}Sr_{0.2}CoO_{3-\delta}$ as an efficient catalyst for oxygen evolution reaction. Electrochim. Acta **244**, 139-145 (2017).

86. Sharpe, R., Gracia, J., Lim, T., Niemantsverdriet, J.W.H., Jiao, Y.: Oxygen evolution reaction on perovskite electrocatalysts with localized spins and orbital rotation symmetry. ChemCatChem **8**, 3762–3768 (2016).

87. Zhao, H., Chen, C., Chen, D., Saccoccio, M., Wang, J., Gao, Y., Wan, T.H., Ciucci, F.: $Ba_{0.95}La_{0.05}FeO_{3-\delta}$–multi-layer graphene as a low-cost and synergistic catalyst for oxygen evolution reaction. Carbon **90**, 122-129 (2015).

88. Grimaud, A., Hong, W.T., Shao-Horn, Y., Tarascon, J.M.: Anionic redox processes for electrochemical devices. Nature materials **15**(2), 121-126 (2016).

89. Chen, D., Wang, J., Zhang, Z., Shao, Z., Ciucci, F.: Boosting oxygen reduction/evolution reaction activities with layered perovskite catalysts. Chem. Commun. **52**(71), 10739-10742 (2016).

90. Wang, J., Gao, Y., Chen, D., Liu, J., Zhang, Z., Shao, Z., Ciucci, F.: Water splitting with an enhanced bifunctional double perovskite. ACS Cata. **8**(1), 364-371 (2017).

91. Mao, X., Wang, W., Chen, X., Lu, Y.: Multiferroic properties of layer-structured $Bi_5Fe_{0.5}Co_{0.5}Ti_3O_{15}$

ceramics. Appl. Phys. Lett. **95**(8), 082901 (2009).

92. Zou, W., Wang, J., Chen, Z., Shi, N., Li, Z., Cui, Z., Li, X., Yin, X., Yan, W., Huang, H., Peng, R., Fu, Z., Lu, Y.: Anisotropic electrical and magnetic properties in grain-oriented $Bi_4Ti_3O_{12}$–$La_{0.5}Sr_{0.5}MnO_3$. J. Mater. Chem. C **6**(42), 11272-11279 (2018).

93. Wang, G., Huang, Y., Sun, S., Wang, J., Peng, R., Lu, Y., Tan, X.: Layer effects on the magnetic behaviors of Aurivillius compounds $Bi_{n+1}Fe_{n-3}Ti_3O_{3n+1}$ (n= 6, 7, 8, 9). J. Am. Ceram. Soc. **99**(4), 1318-1323 (2016).

94. Ghorbani-Moghadam, T., Kompany, A., Bagheri-Mohagheghi, M.M., Abrishami, M.E.: Cobalt spin states investigation of Ruddlesden-Popper $La_{2-x}Sr_xCoO_4$, using X-ray diffraction and infrared spectroscopy. J. Magn. Magn. Mater. **465**, 768-774 (2018).

95. Swatsitang, E., Phokha, S., Hunpratub, S., Usher, B., Bootchanont, A., Maensiri, S., Chindaprasirt, P.: Characterization and magnetic properties of cobalt ferrite nanoparticles. J. Alloys Compd. **664**, 792-797 (2016).

96. Huang, Y., Sun, S., Wang, G., Wang, J., Peng, R., Lu, Y.: Yttrium-modified $Bi_7Fe_{1.5}Co_{1.5}Ti_3O_{21}$ ceramics with improved room temperature multiferroic properties. Rsc Adv. **4**(55), 29264 (2014).

97. Chen, L., Li, F., Ni, B., Xu, J., Fu, Z., Lu, Y.: Enhanced visible photocatalytic activity of hybrid Pt/a-Fe_2O_3 nanorods. RSC Adv. **2**(26), 10057-10063 (2012).

98. Li, X., Ju, Z., Li, F., Huang, Y., Xie, Y., Fu, Z., Knize, R.J., Lu, Y.: Visible light responsive $Bi_7Fe_3Ti_3O_{21}$ nanoshelf photocatalysts with ferroelectricity and ferromagnetism. J. Mater. Chem. A **2**(33), 13366-13372 (2014).

99. Chen, Z., Wang, J., Huan, D., Sun, S., Wang, G., Fu, Z., Zhang, W., Zheng, X., Pan, H., Peng, R., Lu, Y.: Tailoring the activity via cobalt doping of a two-layer Ruddlesden-Popper phase cathode for intermediate temperature solid oxide fuel cells. J. Power Sources **371**, 41-47 (2017).

100. Yang, J., Tong, W., Liu, Z., Zhu, X.B., Dai, J.M., Song, W.H., Yang, Z.R., Sun, Y.P.: Structural, magnetic, and EPR studies of the Aurivillius phase $Bi_6Fe_2Ti_3O_{18}$ and $Bi_6FeCrTi_3O_{18}$. Phys. Rev. B **86**(10), 2757-2764 (2012).

101. Mao, X., Wang, W., Chen, X., Lu, Y.: Multiferroic properties of layer-structured $Bi_5Fe_{0.5}Co_{0.5}Ti_3O_{15}$ ceramics. Appl. Phys. Lett. **95**(8), 1719 (2009).

102. Li, M., Pietrowski, M.J., Souza, R.A.D., Zhang, H., Reaney, I.M., Cook, S.N., Kilner, J.A., Sinclair, D.C.: A family of oxide ion conductors based on the ferroelectric perovskite $Na_{0.5}Bi_{0.5}TiO_3$. Nat. Mater.

13, 31-35 (2014).

103. Mao, X., Wang, W., Sun, H., Lu, Y., Chen, X.: Structural, magnetic and ferroelectric properties of $Bi_5FeTi_3O_{15}$ and $Bi_5Fe_{0.5}Co_{0.5}Ti_3O_{15}$ ceramics. Integr. Ferroelectr. **132**(1), 16-21 (2012).

104. Kang, J., Hwang, J., Han, B.: First-principles computational screening of highly active pyrites catalysts for hydrogen evolution reaction through a universal relation with a thermodynamic variable. J. Phys. Chem. C **122**(4), 2107-2112 (2018).

105. Y. Moritomo, Higashi, K., Matsuda, K., Nakamura, A.: Spin-state transition in layered perovskite cobalt oxides: La2-xSrxCoO4 (0.4<x<1.0). Phys. Review B **55**, R14725 (1997).

106. Zhang, W., Zhou, K.: Ultrathin Two-Dimensional Nanostructured Materials for Highly Efficient Water Oxidation. Small **13**(32) (2017).

107. Huang, J., Chen, J., Yao, T., He, J., Jiang, S., Sun, Z., Liu, Q., Cheng, W., Hu, F., Jiang, Y., Pan, Z., Wei, S.: CoOOH Nanosheets with High Mass Activity for Water Oxidation. Angewandte Chemie **54**(30), 8722-8727 (2015).

108. Park, S., Lee, C.W., Kang, M.G., Kim, S., Kim, H.J., Kwon, J.E., Park, S.Y., Kang, C.Y., Hong, K.S., Nam, K.T.: A ferroelectric photocatalyst for enhancing hydrogen evolution: polarized particulate suspension. Physical chemistry chemical physics : PCCP **16**(22), 10408-10413 (2014).

109. Zhen, C., Yu, J.C., Liu, G., Cheng, H.M.: Selective deposition of redox co-catalyst(s) to improve the photocatalytic activity of single-domain ferroelectric $PbTiO_3$ nanoplates. Chemical communications **50**(72), 10416-10419 (2014).

110. Wu, H., Ling, H., Zhang, Z., Li, Y., Liang, L., Chai, G.: Research progress on photocatalytic activity of ferroelectric materials. Acta Phys. Sin. **66**(16), 167702 (2017).

111. Li, H., Sang, Y., Chang, S., Huang, X., Zhang, Y., Yang, R., Jiang, H., Liu, H., Wang, Z.L.: Enhanced ferroelectric-nanocrystal-based hybrid photocatalysis by ultrasonic-wave-generated piezophototronic effect. Nano letters **15**(4), 2372-2379 (2015).

112. Morris, M.R., Pendlebury, S.R., Hong, J., Dunn, S., Durrant, J.R.: Effect of Internal Electric Fields on Charge Carrier Dynamics in a Ferroelectric Material for Solar Energy Conversion. Advanced materials **28**(33), 7123-7128 (2016).

113. Lou, Z., Wang, P., Huang, B., Dai, Y., Qin, X., Zhang, X., Wang, Z., Liu, Y.: Enhancing Charge Separation in Photocatalysts with Internal Polar Electric Fields. ChemPhotoChem **1**(5), 136-147 (2017).

114. Yang, W.C., Rodriguez, B.J., Gruverman, A., Nemanich, R.J.: Photo electron emission microscopy

of polarity-patterned materials. Journal of Physics: Condensed Matter **17**(16), S1415-S1426 (2005).

115. Dunn, S., Tiwari, D., Jones, P.M., Gallardo, D.E.: Insights into the relationship between inherent materials properties of PZT and photochemistry for the development of nanostructured silver. Journal of Materials Chemistry **17**(42), 4460 (2007).

116. Kalinin, S.V., Bonnell, D.A., Alvarez, T., Lei, X., Hu, Z., Ferris, J.H.: Atomic Polarization and Local Reactivity on Ferroelectric Surfaces: A New Route toward Complex Nanostructures. Nano Lett. **2**(6), 589-593 (2002).

117. Dunn, S., Jones, P.M., Gallardo, D.E.: Photochemical Growth of Silver Nanoparticles on c- and c+ Domains on Lead Zirconate Titanate Thin Films. J. Am. Chem. Soc. **129**(28), 8724-8728 (2007).

118. Li, D., Zhao, M.H., Garra, J., Kolpak, A.M., Rappe, A.M., Bonnell, D.A., Vohs, J.M.: Direct in situ determination of the polarization dependence of physisorption on ferroelectric surfaces. Nature materials **7**(6), 473-477 (2008).

119. Li, X., Ju, Z., Li, F., Huang, Y., Xie, Y., Fu, Z., Knized, R.J., Lu, Y.: Visible light responsive $Bi_7Fe_3Ti_3O_{21}$ nanoshelf photocatalysts with ferroelectricity and ferromagnetism. J. Mater. Chem. A **2**, 13366-13372 (2014).

120. Wang, J., Fu, Z., Peng, R., Liu, M., Sun, S., Huang, H., Li, L., Knize, R.J., Lu, Y.: Low magnetic field response single-phase multiferroics under high temperature. Mater. Horiz. **2**(2), 232-236 (2015).

121. Chen, L., Li, F., Ni, B., Xu, J., Fu, Z., Lu, Y.: Enhanced visible photocatalytic activity of hybrid Pt/α-Fe2O3 nanorods. RSC Advances **2**(26), 10057-10063 (2012).

122. Yang, J., Tong, W., Liu, Z., Zhu, X.B., Dai, J.M., Song, W.H., Yang, Z.R., Sun, Y.P.: Structural, magnetic, and EPR studies of the Aurivillius phase $Bi_6Fe_2Ti_3O_{18}$ and $Bi_6FeCrTi_3O_{18}$. Phys. Review B **86**(10) (2012).

123. Jia, T., Kimura, H., Cheng, Z., Zhao, H., Kim, Y.H., Osada, M., Matsumoto, T., Shibata, N., Ikuhara, Y.: Mechanical force involved multiple fields switching of both local ferroelectric and magnetic domain in a $Bi_5Ti_3FeO_{15}$ thin film. Npg Asia Materials **9**(2) (2017).

124. Guan, D., Zhou, J., Huang, Y.C., Dong, C.L., Wang, J.Q., Zhou, W., Shao, Z.: Screening highly active perovskites for hydrogen-evolving reaction via unifying ionic electronegativity descriptor. Nat. Commun. **10**(1), 3755 (2019).

125. Zhao, B., Zhang, L., Zhen, D., Yoo, S., Ding, Y., Chen, D., Chen, Y., Zhang, Q., Doyle, B., Xiong, X., Liu, M.: A tailored double perovskite nanofiber catalyst enables ultrafast oxygen evolution. Nat.

Commun. **8**(1), 14586 (2017).

126. Zhou, Y., Sun, S., Song, J., Xi, S., Chen, B., Du, Y., Fisher, A.C., Cheng, F., Wang, X., Zhang, H., Xu, Z.J.: Enlarged CoO covalency in octahedral sites leading to highly efficient spinel oxides for oxygen evolution reaction. Adv. Mater. **30**(32), e1802912 (2018).

127. Zhu, Y., Tahini, H.A., Hu, Z., Chen, Z.G., Zhou, W., Komarek, A.C., Lin, Q., Lin, H.J., Chen, C.T., Zhong, Y., Fernandez-Diaz, M.T., Smith, S.C., Wang, H., Liu, M., Shao, Z.: Boosting oxygen evolution reaction by creating both metal ion and lattice-oxygen active sites in a complex oxide. Adv. Mater. **32**(1), e1905025 (2020).

128. Duan, Y., Sun, S., Sun, Y., Xi, S., Chi, X., Zhang, Q., Ren, X., Wang, J., Ong, S.J.H., Du, Y., Gu, L., Grimaud, A., Xu, Z.J.: Mastering surface reconstruction of metastable spinel oxides for better water oxidation. Adv. Mater. **31**(12), e1807898 (2019).

129. Dandeneau, C.S., Yang, Y., Krueger, B.W., Olmstead, M.A., Bordia, R.K., Ohuchi, F.S.: Site occupancy and cation binding states in reduced polycrystalline $Sr_xBa_{1-x}Nb_2O_6$. Appl. Phys. Lett. **104**(10), 101607 (2014).

130. Wesner, M., Herden, C., Kip, D., E.Kr• atzig, Moretti, P.: Photorefractive steady state solitons up to telecommunication wavelengths in planar SBN waveguides. Optics Commun. **188**, 69-76 (2001).

131. Cihangir Duran, Trolier-McKinstry, S., Messing, G.L.: Fabrication and electrical properties of textured $Sr_{0.53}Ba_{0.47}Nb_2O_6$ ceramics by templated grain growth. J. Am. Ceram. Soc. **83**, 2203–2213 (2000).

132. Chen, Z., Wang, W., Yang, Y., Tang, H., Sun, Z., Wang, J., Huang, H., Peng, R., Fu, Z., Lu, Y.: F^--induced tunable perovskite structure and impressive spin polarization in $SrCoO_3$. Chem. Mater. **31**(22), 9453-9461 (2019).

133. Li, X., Liu, H., Chen, Z., Wu, Q., Yu, Z., Yang, M., Wang, X., Cheng, Z., Fu, Z., Lu, Y.: Enhancing oxygen evolution efficiency of multiferroic oxides by spintronic and ferroelectric polarization regulation. Nat. Commun. **10**(1), 1409 (2019).

134. Wang, W., Ye, Y., Feng, J., Chi, M., Guo, J., Yin, Y.: Enhanced photoreversible color switching of redox dyes catalyzed by barium-doped TiO_2 nanocrystals. Angew. Chem. **54**(4), 1321-1326 (2015).

135. Ling, T., Yan, D.Y., Jiao, Y., Wang, H., Zheng, Y., Zheng, X., Mao, J., Du, X.W., Hu, Z., Jaroniec, M., Qiao, S.Z.: Engineering surface atomic structure of single-crystal cobalt (II) oxide nanorods for superior electrocatalysis. Nat. Commun. **7**, 12876 (2016).

136. Tu, Y., Chen, S., Li, X., Gorbaciova, J., Gillin, W.P., Krause, S., Briscoe, J.: Control of oxygen

vacancies in ZnO nanorods by annealing and their influence on ZnO/PEDOT:PSS diode behaviour. J. Mater. Chem. C **6**(7), 1815-1821 (2018).

137. KURODA, S., KUBOTA, K.: Impurity effect on the Raman spectra of $Sr_{0.6}Ba_{0.4}Nb_2O_6$. J. Phys. Chem. Solids **44**, 527-530 (1983).

138. Amzallag, E., Chang, T.S., Pantell, R.H., Feigelson, R.S.: Raman Scattering by $Sr_xBa_{1-x}Nb_2O_6$. J. Appl. Phys. **42**(8), 3254-3256 (1971).

139. Mao, X., Sun, H., Wang, W., Lu, Y., Chen, X.: Effects of Co-substitutes on multiferroic properties of $Bi_5FeTi_3O_{15}$ ceramics. Solid State Commun. **152**(6), 483-487 (2012).

140. Davó-Quiñonero, A., Bailón-García, E., López-Rodríguez, S., Juan-Juan, J., Lozano-Castelló, D., García-Melchor, M., Herrera, F.C., Pellegrin, E., Escudero, C., Bueno-López, A.: Insights into the oxygen vacancy filling mechanism in CuO/CeO_2 catalysts: A key step toward high selectivity in preferential CO oxidation. ACS Cata., 6532-6545 (2020).

141. Mefford, J.T., Hardin, W.G., Dai, S., Johnston, K.P., Stevenson, K.J.: Anion charge storage through oxygen intercalation in $LaMnO_3$ perovskite pseudocapacitor electrodes. Nat. Mater. **13**(7), 726-732 (2014).

142. Zaanen, J., Sawatzky, G.A., Allen, J.W.: Band gaps and electronic structure of transition-metal compounds. Phys. Rev. Lett. **55**(4), 418-421 (1985).

143. Kibsgaard, J., Chorkendorff, I.: Considerations for the scaling-up of water splitting catalysts. Nat. Energy. **4** (6), 430-433 (2019).

Appendix 1

List of Publications

1. **Li, X.**; Liu, H.; Sun, Y.; Zhu, L.; Yin, X.; Sun, S.; Fu, Z.; Lu, Y.; Wang X.; Cheng, Z. High Oxygen Evolution Activity of Tungsten Bronze Oxides Boosted by Anchoring of Co at Nb Sites Accompanied by Substantial Oxygen Vacancies, *Adv. Sci.*, 7, 2002242, **20202020** (**IF=15.8**)
2. **Li, X.**; Sun, Y.; Wu, Q.; Liu, H.; Gu, W.; Wang, X.; Cheng, Z.; Fu, Z.; Lu, Y. Optimized electronic configuration to improve the surface absorption and bulk conductivity for enhanced oxygen evolution reaction. *J. Am. Chem. Soc.* **2019,** *141* (7), 3121-3128. (**IF= 14.6**)
3. **Li, X.**; Liu, H.; Chen, Z.; Wu, Q.; Yu, Z.; Yang, M.; Wang, X.; Cheng, Z.; Fu, Z.; Lu, Y. Enhancing oxygen evolution efficiency of multiferroic oxides by spintronic and ferroelectric polarization regulation. *Nat. Commun.* **2019,** *10* (1), 1409. (**IF= 12.1**)
4. **Li, X.**; Wang X.; Cheng, Z. Understanding the mechanism of oxygen evolution reaction (OER) with the consideration of spin. *Electrochem. Energy Review* 4, 136–145, **2021 (IF=27.31)**
5. Gu, W.; **Li, X.**; Zhang, W.; Wang, J.; Yin, X.; Zhu, L.; Chen, Z.; Zou, W.; Fu, Z.; Lu, Y. Self-limited ion-exchange grown Bi6Fe2Ti3O18-BiOBr ferroelectric heterostructure and the enhanced photocatalytic oxygen evolution. *Applied Surface Science* **2019,** *479*, 137-147.
6. Liu, H.; **Li, X.**; Peng, C.; Zhu, L.; Zhang, Y.; Cheng, H.; Cui, J.; Wu, Q.; Zhang, Y.; Chen, Z.; Zou, W.; Gu, W.; Huang, H.; Wang, J.; Ye, B.; Fu, Z.; Lu, Y. Activating the lattice oxygen in (Bi0.5Co0.5)2O3 by vacancy modulation for efficient electrochemical water oxidation. *Journal of Materials Chemistry A* **2020,** *8* (26), 13150-13159.
7. Sun, Y.; Chen, J.; **Li, X.**; Lu, Y.; Zhang, S.; Cheng, Z. Flexible piezoelectric energy harvester/sensor with high voltage output over wide temperature range. *Nano Energy* **2019,** *61*, 337-345.
8. Hu, L.; Yin, X.; Cheng, H.; **Li, X.**; Zhang, Y.; Gu, W.; Zou, W.; Zhu, L.; Wu, Q.; Huang, H.; Wang, J.; Ye, B.; Fu, Z.; Lu, Y. Quantitative correlations between photochemical performance and low-electron-density defect. *Applied Surface Science* **2020,** *527*, 146688.
9. Sun, Y.; Lu, Y.; **Li, X.**; Yu, Z.; Zhang, S.; Sun, H.; Cheng, Z. Flexible hybrid piezo/triboelectric energy harvester with high power density workable at elevated temperatures. *Journal of Materials Chemistry A*

2020, *8* (24), 12003-12012.

10. Yin, X.; Sun, Y.; Wu, X.; **Li, X.**; Liu, H.; Gu, W.; Zou, W.; Zhu, L.; Fu, Z.; Lu, Y. Superior adsorption capability and excellent photocatalytic activity derived from the ferroelectric external screening effect in Bi3TiNbO9 single-crystal nanosheets. *Catalysis Science & Technology* **2020,** *10* (9), 2864-2873.
11. Hao, C.; Wu, Y.; An, Y.; Cui, B.; Lin, J.; **Li, X.**; Wang, D.; Jiang, M.; Cheng, Z.; Hu, S. Interface-coupling of CoFe-LDH on MXene as high-performance oxygen evolution catalyst. *Materials Today Energy* **2019,** *12*, 453-462.
12. Hu, L.; Geng, X.; Singh, S.; Shi, J.; Hu, Y.; Li, S.; Guan, X.; He, T.; **Li, X.**; Cheng, Z.; Patterson, R.; Huang, S.; Wu, T. Synergistic effect of electron transport layer and colloidal quantum dot solid enable PbSe quantum dot solar cell achieving over 10 % efficiency. *Nano Energy* **2019,** *64*, 103922.
13. Yu, Z.; Chen, Y.; Cheng, Z.; Tsekouras, G.; **Li, X.**; Wang, X.; Kong, X.; Dou, S. X. Enzyme-catalysed room temperature and atmospheric pressure synthesis of metal carbonate hydroxides for energy storage. *Nano Energy* **2018,** *54*, 200-208.
14. Zou, W.; Wang, J.; Chen, Z.; Shi, N.; Li, Z.; Cui, Z.; **Li, X.**; Yin, X.; Yan, W.; Huang, H.; Peng, R.; Fu, Z.; Lu, Y. Anisotropic electrical and magnetic properties in grain-oriented Bi4Ti3O12–La0.5Sr0.5MnO3. *Journal of Materials Chemistry C* **2018,** *6* (42), 11272-11279.

Appendix 2

Conferences

1. *2018 International Conference on Emerging Advanced Nanomaterials (ICEAN)*.

   Time: 30th October - 2nd November 2018

   Place: Newcastle NSW, Australia.

   Form: **Poster presentation**

   Title: Electronic regulation in layered perovskite for oxygen evolution

2. *20th International Union of Materials Research Societies – International Conference in Asia (IUMRS - ICA).*

   Time: 22 – 26 September 2019.

   Place: Perth, Western Australia.

   Form: **Oral presentation**

   Title: Enhancing oxygen evolution efficiency of multiferroic oxides by spintronic and ferroelectric polarization regulation

3. *2019 Internal Symposium on Future Materials.*

   Time: January 30 – February 1 2019.

   Place: Wollongong, Australia.

   Form: **Poster presentation**

   Title: New strategy to enhance oxygen evolution efficiency by spintronic and ferroelectric polarization regulation